# PLACE IN RETURN BOX to remove this checkout from your record. TO AVOID FINES return on or before date due. MAY BE RECALLED with earlier due date if requested.

DATE DUE	DATE DUE	DATE DUE
	<u>.</u>	

2/05 p:/CIRC/DateDue.indd-p.1

# ELECTRONIC CHARACTERIZATION AND FABRICATION OF CVD DIAMOND PIEZORESISTIVE PRESSURE SENSORS

By

Sondes Sahli

11

#### **A DISSERTATION**

Submitted to

Michigan State University
in partial fulfillment of the requirements
for the degree of

**DOCTOR OF PHILOSOPHY** 

Department of Electrical Engineering

1997

THS

#### **ABSTRACT**

# ELECRONIC CHARACTERIZATION AND FABRICATION OF CVD DIAMOND PIEZORESISTIVE PRESSURE SENSORS

By

#### Sondes Sahli

Diamond piezoresistive sensors outperform their Si or SiC counterparts in sensitivity, especially in harsh environments and at high temperatures. In this work, the resistivity and gauge factor (GF) of in-situ B-doped polycrystalline chemical vapor deposited (CVD) diamond grown on insulating substrates, were studied. A hot filament CVD reactor was built, optimized for 4" wafers and used for film deposition.

The effect of substrate, post deposition annealing and electric field on the resistivity of CVD diamond were studied using three types of films: small grain (1 - 2  $\mu$ m), large grain (up to 170  $\mu$ m) and homoepitaxial. In-situ B-doped and undoped films deposited on oxidized, n-type and p-type silicon were used. Resistivity, temperature and electric field ranges of 0.27 - 535  $\Omega$ cm, 300 - 633 K and 10 - 650 V/cm, respectively, were explored.

The role of grain boundaries (GBs) in current flow was studied by performing four-point probe I-V across many grains, potential profile across five grains and two-point-probe I-V within a single grain and across an individual GB. The potential profiles

revealed non-uniform current flow and the I-V data across individual GBs suggested the existence of potential barriers at GBs

The pressure response of small grain films was measured in the pressure, resistivity and field ranges of 10 - 740 Torr, 0.29 - 116  $\Omega$ cm and 10 - 255 V/cm, respectively. The results showed that higher doping minimized GF fluctuations with electric field. Cantilever beam measurements in the temperature range of 22 - 80 °C revealed that GF is constant with temperature at low resistivity, but increases at intermediate resistivity and decreases at high resistivity. Intra- and inter-grain GF measurements achieved an intragrain GF of 4062 and provided direct evidence that the presence of GBs lowers GF.

Copyright by SONDES SAHLI 1997 To

my parents, my sister and my brothers

and

to all those whose path crossed mine

#### **ACKNOWLEDGMENTS**

I would like to thank Allah (soobhanahowa taalah) for providing me with the ability to complete this work. I owe my greatest thanks to my parents who worked hard and sacrificed much so I can reach my goals. A very special thank you goes to my sister, my brothers and my friends for their encouragements.

I would like to thank my advisor, Dr. Dean Aslam, for his guidance and the members of my oral committee, Dr. Jes Asmussen, Dr. David Grummon and Dr. Karen Klomparens for their comments. Many thanks also go to all faculty, staff and students at Michigan State University who made my school years enjoyable with their help and smile.

# **TABLE OF CONTENTS**

L	ST O	F TAB	LES	ix
LI	ST O	F FIG	URES	X
1	Res	earch N	Motivation and Goals	1
	1.1	Introd	luction	1
	1.2	Objec	tive of this Work	2
	1.3	Disser	rtation Organization	5
2	Bac	kgroun	ıd	6
	2.1	Introd	luction	6
	2.2	Diamo	ond Sensors	<del>6</del>
		2.2.1	Diamond Piezoresistive Sensors	8
		2.2.2	Other Diamond Sensors	11
	2.3	Theor	y of Piezoresistance Property	12
		2.3.1	Definition of Gauge Factor	12
		2.3.2	Piezoresistance in Single Crystal Semiconductors	15
		2.3.3	Piezoresistance Models in Polycrystalline Semiconductors	24
	2.4	Curre	nt Understanding of Diamond Piezoresistance	29
		2.4.1	Single Crystal Diamond	29
		2.4.2	Polycrystalline Diamond	30
	2.5	Diamo	ond Film Technology	33
		2.5.1	Chemical Vapor Deposition of Diamond	33
		2.5.2	Doping	38
		2.5.3	Patterning	39
		2.5.4	Metallization	41
	2.6	Summ	nary	43

3	Dia	mond I	Film Technology	44
	3.1	Introd	luction	44
	3.2	Hot F	ilament Chemical Vapor Deposition Reactor	44
		3.2.1	System Testing and Optimization	46
		3.2.2	System Operation	57
	3.3	Samp	le fabrication	59
		3.3.1	Small Grain Film	59
		3.3.2	Large Grain Film	62
		3.3.3	Homoepitaxial Film	69
	3.4	Summ	nary	71
4	Res	istivity	Characterization	72
	4.1	Introd	luction	72
	4.2	Effect	of Substrate Conduction	73
	4.3	Effect	of Anneal on Resistivity	73
		4.3.1	Experimental Details	74
		4.3.2	Results	74
		4.3.3	Discussion	76
	4.4	Effect	of Electric Field on Resistivity	78
		4.4.1	Experimental Details	79
		4.4.2	Electric Field Effect as a function of Doping	79
		4.4.3	Electric Field Effect as a function of Temperature	81
		4.4.4	Electric Field Effect as a function of Morphology	81
		4.4.5	Discussion	84
	4.5	Curre	nt Flow Study	85
		4.5.1	Experimental	87
		4.5.2	Four Point Probe Measurements	87
		4.5.3	Potential Profile Measurements	89
		4.5.4	Intra- and Inter-grain I-V	89
		4.5.5	Non-uniform Current Flow	93
	4.6	Summ	nary	95

5	Sen	sor characterization	96
	5.1	Introduction	96
	5.2	Gauge Factor Measurement Setup	97
		5.2.1 Pressure Sensor Setup	97
		5.2.2 Cantilever Beam Setup	101
	5.3	Effect of Electric Field on Piezoresistance	101
	5.4	Effect of Temperature on Piezoresistance	109
	5.5	Summary	111
6	Intr	ra-grain Gauge Factor	115
	6.1	Introduction	115
	6.2	Measurement Setup	115
	6.3	Gauge Factor for Different Path Morphologies	117
	6.4	Summary	123
7	Sun	nmary and Future Research	124
	7.1	Introduction	124
	7.2	Summary of Contributions	124
		7.2.1 Results Reported for the First Time	124
		7.2.2 Other Significant Results	126
	7.3	Future Research	126
BI	BLIC	OGRAPHY	128

# LIST OF TABLES

2.1	Comparison of diamond properties and some commonly used semiconductors	7
2.2	Summary of reported GF data for polycrystalline diamond	9
2.3	Reported temperature dependence of GF of polycrystalline diamond for	
	different resistivities	10
2.4	Longitudinal GF for films dominated by [100], [110], [111] and random	
	grain orientation [51]	29
3.1	Typical deposition parameters	59
4.1	Sample specifications	<b>7</b> 9
4.2	Summary of linear I-V data	94

## **LIST OF FIGURES**

1.1	Steps needed to put CVD diamond piezoresistors on the market	. 4
2.1	Simple geometry to define GF	13
2.2	Energy band structure of Si	16
2.3	Constant energy ellipsoids in k-space near the conduction band minima	
	of Si	17
2.4	(a) Conduction band under zero strain and an electric field in the [100]	
	direction, electrons moving parallel to the field, $k_x$ , have larger effective	
	mass than those moving perpendicular to the field, $k_y$ , $k_z$ . (b) As a result	
	of tension in the [100] direction, the $k_x$ band minima are lowered	19
2.5	The factor P(N,T) with which the piezoresistive coefficient at RT must be	
	multiplied to obtain GF at temperature T and donor concentration N in Si	21
2.6	Simplified and roughly drawn valence band diagram of Si under (a) zero	
	stress and (b) uniaxial tension	23
2.7	(a) Schematic of a grain and surrounding GBs in polysilicon.	
	(b) Corresponding energy band diagram assuming p-type doping and	
	neglecting the physical width of GB. Traps with density $Q_t$ having energy	
	in the bandgap capture holes creating a barrier potential $qV_B$ and a space	
	charge region, L <sub>w</sub> . (c) Scattering in GB is modeled by a potential barrier	
	with height $q\chi$ and width $L_{gb}$ . The different components of carrier	
	transport across the barrier are indicated	25
2.8	Longitudinal gauge factor as a function of doping concentration for	
	Boron () and Phosphorus () doped polysilicon. The calculation are	
	based on a grain size of 60 nm and a texture dominated by [110]	
	orientation. Curves b show the same calculation with GB assumed to be	
	insensitive to strain [51]	28
2.9	a) Resistivity, (b) Hall mobility and (c) hole concentration measurements	
	of simultaneously deposited polycrystalline (PD), homoepitaxial (HMD)	
	and highly oriented (HOD) films. Films deposited in the same run have the	

	same number	. 32
2.10	Atomic C-H-O diamond deposition phase diagram indicating the diamond	
	growth domain [66]	35
2.11	Growth rate for different CVD methods correlate with the temperature of	
	the as mixture needed for growth [66]	37
2.12	Irvin curve for single crystal (●) and polycrystalline (▲) B-doped	
	diamond. The open symbols refer to effective doping concentration,	
	N <sub>A</sub> -N <sub>D</sub> , and the closed symbols to the free hole concentration, p	40
2.13	Interface band diagram of Ti on diamond: (a) as deposited Ti, (b) high	
	concentration of electrically active defects created via carbide formation	
	and/or ion bombardment, (c) the defects created in (b) decrease the	
	effective Ti/diamond barrier height	42
3.1	Schematic of the hot filament reactor	45
3.2	(a) Filament assembly and (b) substrate holder	47
3.3	Effect of filament to substrate separation	49
3.4	Effect of methane	. 50
3.5	Temperature gradient over the 4 inch substrate	51
3.6	Effect of (a) pressure and (b) gas flow rate at D(F,S) = 2.5 cm	52
3.7	Effect of initial high temperature cure on filament	54
3.8	Effect of repeated use on filament	55
3.9	Effect of multiple runs on the room temperature filament resistance	56
3.10	Types of CVD diamond films used in this work	60
3.11	Nucleation and patterning	. 61
3.12	Temperature and gas profiles during RTP anneal	61
3.13	(a) processed 4" wafer, (b) CVD diamond resistor (c) SEM and	
	(d) Raman	63
3.14	Raman Spectra of the B-doped film	64
3.15	(a) Light microscope photo of doped CVD film and (b) corresponding	
	grain size distribution	. 65
3.16	AFM of different types of GBs	66
3.17	AFM of typical well defined GB	67

3.18	Typical intra-grain AFM
3.19	Raman Spectrum of B-doped homoepitaxial diamond
4.1	Resistivity after anneal vs. resistivity before anneal. Inset: ratio of
	resistivity after anneal to that before anneal
4.2	Raman spectra and SEM of samples used in the anneal study
4.3	Effect of electric field on resistivity for different doping levels
4.4	Normalized resistivity vs. field of small grain sample as a function of
	temperature. (a) $\rho_{40}$ and (b) $(\rho_{40} - \rho_{600}) / \rho_{40}$ as a function of T
4.5	Ratio of room temperature resistivity to low-field resistivity for B-doped
	homoepitaxial, highly oriented, large grain and small grain films
4.6	Four-probe resistivity measurements as a function of temperature
4.7	Potential profile measurements and corresponding probe positions 88
4.8	I-V data and corresponding probe positions
4.9	Current flow in polycrystalline diamond with non-uniform grain size
	modeled in terms of paths made of small grains and paths made of large
	grains
5.1	(a) Differential pressure measurement setup and (b) plate model 98
5.2	Pressure response of wire strain gauge
5.3	Schematic diagram of a cantilever beam setup
5.4	Room temperature pressure response measured using different electric
	fields. Insets: (i) SEM, (ii) Raman and (iii) zero strain IV 102
5.5	Room temperature pressure response measured using different electric
	fields. Insets: (i) SEM, (ii) Raman and (iii) zero strain IV 103
5.6	Room temperature pressure response measured using different electric
	fields. Insets: (i) SEM, (ii) Raman and (iii) zero strain IV 104
5.7	Calculated GF as a function of strain for SS4S6. Inset: (■) GF at 20
	microstrains and (O) zero strain resistivity 106
5.8	Calculated GF as a function of strain for SS70S2. Inset: (■) GF at 20
	microstrains and (O) zero strain resistivity
5.9	Calculated GF as a function of strain for SS70S4. Inset: (■) GF at 20
	microstrains and (O) zero strain resistivity 108

5.10	Summary of room temperature GF vs. resistivity data reported in	
	literature	110
5.11	Effect of temperature on GF	112
5.12	Summary of data reported in literature on the effect of temperature on	
	GF	113
6.1	Small grain I-V at different strains and corresponding probe location.	
	Insets: Cantilever beam setup, relative resistance change vs. strain and	
	extracted GF	116
6.2	Large grain I-V at different strains and corresponding probe location.	
	Inset: Relative resistance change vs. strain and extracted GF	118
6.3	Intra-grain I-V at different strains and corresponding probe location.	
	Inset: Relative resistance change vs. strain and extracted GF	120

## **CHAPTER 1**

## **Research Motivation and Goals**

#### 1.1 Introduction

As automation and control find their way into more products, the need for sensors to measure and monitor the performance of these products increases. The sensor market revenues are projected to reach \$5.9 billions in 1999 split up into 40% pressure, 30% temperature, 13% acceleration, 13% vibration and 4% others [1]. Today, most pressure sensors are based on silicon device technology: 90% piezoresistive (lower cost and easier signal conditioning) and 10% capacitive [1]. Since pressure sensors cannot be hermetically sealed, the sensor material without passivation will be exposed to its environment during operation. The operation of silicon pressure sensors under chemically harsh, high radiation and high temperature environments is limited by leakage current (~150°C), plastic deformation (~600°C) [2] and corrosion. Thus, there is a need for new sensor materials suitable for such environments.

The high chemical resistance, radiation hardness, thermal conductivity, wide energy gap, high dielectric strength and moderately good carrier mobilities of diamond, make it an excellent material for use in high temperature and chemically harsh environments. However, single crystal natural and synthetic diamonds are too expensive and

scarce to be considered for the sensor market. Lately, a less expensive, low pressure diamond synthesis technique which uses chemical vapor deposition (CVD) has been developed. Although the properties of homoepitaxial CVD diamond rival those of natural diamond, the need for a diamond substrate makes them too costly. The properties of CVD polycrystalline diamond films (PDF), deposited on non-diamond substrates, are being constantly improved [5]. As the cost of CVD diamond is projected to reach \$1.06-1.68/cm<sup>2</sup> [6], PDF pressure sensors will be able to compete with the silicon ones, especially in applications where increased performance and reliability have a higher priority than cost and where the operating conditions cannot be withstood by Si sensors.

#### 1.2 Objective of this Work

The discovery [7][8] of a large piezoresistive gauge factor (GF) in p-type CVD diamond films has generated continued interest for diamond piezoresistive sensors [9][10][11]. GFs as high as 1000 and 700 at room temperature and 200°C [11], respectively, have been measured using cantilever beam, three-point bending fixture and differential pressure setup. The technology of a multisensor test chip for pressure and temperature sensors was developed using process techniques compatible with Si technology [8]. Earlier works characterizing the performance of CVD diamond piezoresistors were limited to proving the feasibility of these sensors by measuring the film response to applied strain and looking for samples that had larger sensitivity. Although a general trend of increasing GF with resistivity was established and some data on the effect of temperature on GF has been published, current understanding of GF in CVD diamond is not sufficient to understand the observed scattering in reported GF values.

The goal of this work is to provide a better understanding of the piezoresistive property in B-doped polycrystalline diamond and eventually contribute to their commercialization. Figure 1.1 gives an overview of what needs to be done in order to put CVD diamond piezoresistive sensors on the market. Sensor characterization aims at understanding the effect of film properties on GF and identify the best film for piezoresistive application. Since GF is defined as the fractional change of resistance to strain, understanding of piezoresistivity is not possible without understanding of the electrical and mechanical properties of CVD diamond. For this reason the study scheme shown in Figure 1.1 covers film characterization as well as sensor characterization. Besides characterizing sensor performance, a high yield, low cost diamond sensor fabrication technology needs to be developed and fully tested.

This work will be limited to those tasks with solid frames. The task to accomplish was dictated by one or more of the following: (i) feasibility of the task given our lab facilities, (ii) necessity of the task to understanding and improving GF and (iii) complete unavailability of similar measurements in the literature. Specifically, the following issues will be addressed:

- (1) study the effect of substrate conduction, anneal, electric field on the resistivity of CVD diamond to determine the appropriate processing and operating conditions for stable resistivity.
- (2) perform intra- and inter-grain I-V to understand current flow in CVD diamond.
- (3) characterize the effect of electric fields and temperature on GF and relate the results to the observed scattering in reported GF.

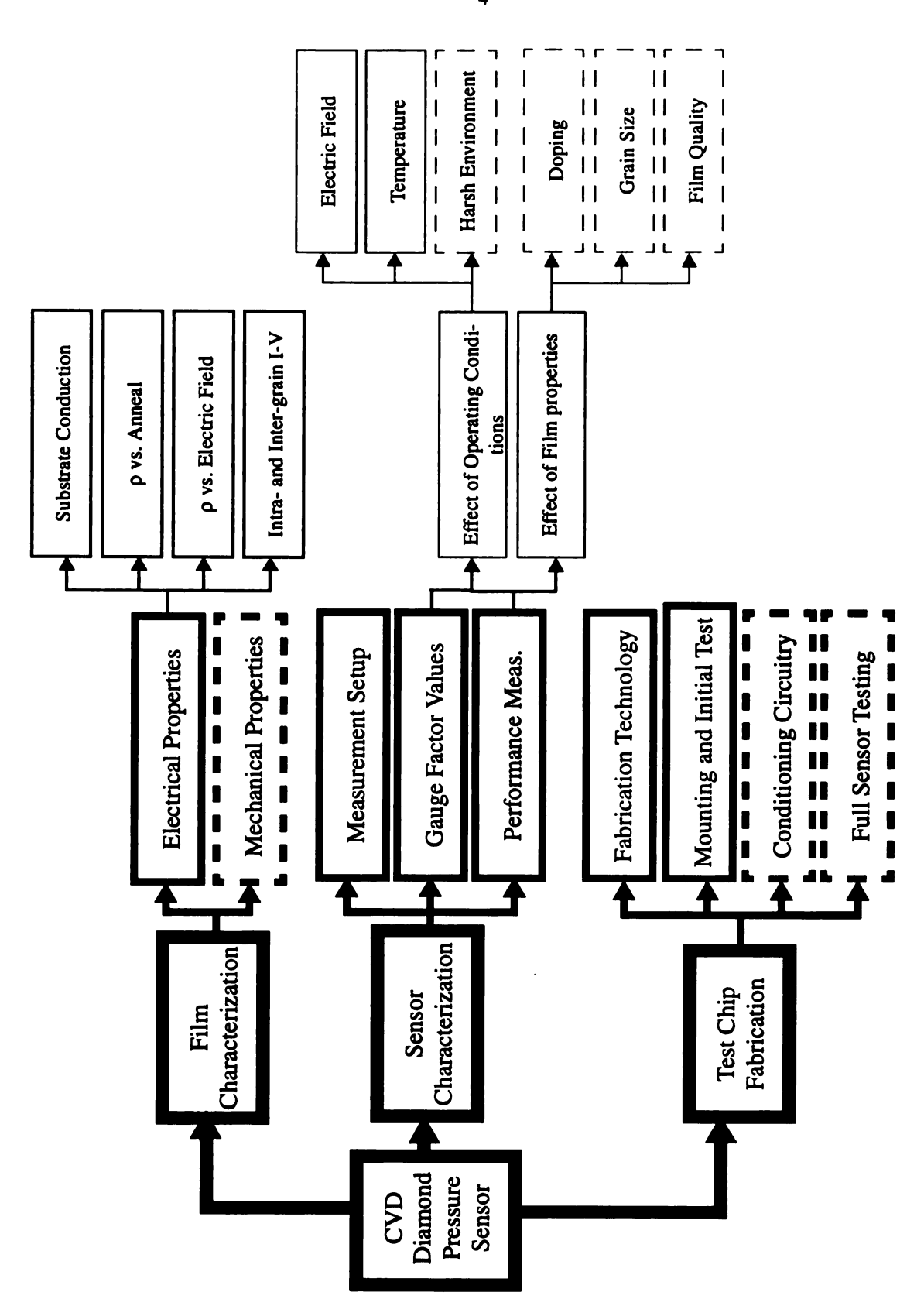


Figure 1.1 Steps needed to put CVD diamond piezoresistors on the market

(4) measure intra- and inter-grain GF.

#### 1.3 Dissertation Organization

This dissertation has six major chapters: background, diamond film technology, resistivity characterization, sensor characterization and intra-grain gauge factor. In chapter two a summary of previous work on diamond sensor with emphasis on piezoresistors is presented. An overview of current status of the electrical and mechanical properties of B-doped CVD diamond is presented. Chapter three gives details of the development of a 4" wafer hot filament reactor used for diamond deposition. The different types of samples used in this study are described. In chapter four, the effect of conducting substrate, anneal and electric field on the resistivity of B-doped CVD diamond are studied. Intra- and inter-grain conduction are investigated. Chapter five focuses on measuring the effect of electric field and temperature on the piezoresistive gauge factor of B-doped CVD diamond using a membrane and a cantilever beam setup. Chapter six deals with intra- and inter-grain gauge factor of polycrystalline diamond. The last chapter summarizes the work of this dissertation and presents suggestions for future related research.

# **CHAPTER 2**

# **Background**

#### 2.1 Introduction

This chapter presents an overview of the recent progress in diamond sensors with an emphasis on piezoresistive sensors. The concept of piezoresistance is introduced and the piezoresistive gauge factor (GF) is defined. Piezoresistive models for both single crystal and polycrystalline semiconductors are presented through the examples of silicon and polysilicon, respectively. Since both stress and resistance are needed to interpret piezoresistance data, a review of the major findings on the mechanical and electrical properties of CVD diamond is provided. Diamond film processes used in sensor fabrication such as deposition, doping, patterning and metallization are described.

#### 2.2 Diamond Sensors

Recent progress in the chemical vapor deposition (CVD) of diamond has led to inexpensive polycrystalline diamond films which make diamond electronic devices and sensors economically feasible. Numerous efforts continuously improve the properties of CVD diamond films aiming to reach those of single crystal, as indicated by Table 2.1. In the case of active electronic devices, such as diodes and field effect transistors, CVD

diamond's potential is challenged by the absence of well established n-type doping, stable native oxide and monocrystalline heteroepitaxial growth. In contrast, the use of diamond as a sensor material does not require n-type doping or monocrystalline diamond. Piezoresistive sensors, Negative temperature coefficient thermistors, flow sensors and chemical sensors have been fabricated using techniques similar or compatible with Si batch processing technology.

Table 2.1 Comparison of diamond properties and some commonly used semiconductors.

Properties	Si	GaÅs	SiC	Natural diamond	Polycrystalline diamond
Band gap, E <sub>g</sub> (eV)	1.12	1.42	3.0	5.45	
Electron mobility, $\mu_n$ (cm <sup>2</sup> /V.s) Hole mobility, $\mu_p$ (cm <sup>2</sup> /V.s)	1450 1500	8500 400	600	1800-200 1600	23 [3] 0.9-165 [4]
Break down field, E <sub>B</sub> (V/cm)x10 <sup>5</sup>	3	60	40	100	1-10 [12]
Electron saturation velocity, v <sub>s</sub> (cm/sec)x10 <sup>7</sup>	1	1	2.5	2.7	
Dielectric constant, $\varepsilon_{\rm r}$	11.7	10.9	9.7	5.5	6.7 [13]
Thermal conductivity, λ (W/cm.K)	1.5	0.5		20	4 - 21.8 [14]
Thermal expansion coef., κ (1/°C) x 10 <sup>-6</sup>	2.6	5.9	4.7	1.1	2.6 [15]
Lattice constant, a (A)	5.43	5.65	4.36	3.57	
Melting point (°C)	1412	1240	2540	4000	
Density (g/cm <sup>3</sup> )	2.328	5.317	3.216	3.52	
Hardness (GPa)	9	7	24.8	100	
Young's modulus, Y (GPa)	130-180	85	700	1050-1200	800-1180 [16]
Poisson ratio, v	.2224	.3132		.121	.071148 [16]
Johnson figure of Merit (WΩsec <sup>-2</sup> )x10 <sup>23</sup>	9	3651	10142	73938	
Keyes figure of Merit	444	90.3	6.3	13.8	

#### 2.2.1 Diamond piezoresistive sensors

Interest for diamond piezoresistive sensors grew with the first quantitative study of the piezoresistive gauge factor in homoepitaxial and polycrystalline diamond films [7]. Several groups have since confirmed the observed large piezoresistive gauge factor for different diamond films.

For synthetic diamond, the gauge factor, extracted from the work of Latsa et. al, was found to be higher than  $10^3$  [8]. The gauge factor for homoepitaxial diamond, measured using a boron doped type 2a film epoxied on a stainless cantilever beam, was reported to be at least 550, four times higher than the highest value for Si [8]. There is not enough information on the characteristics of the homoepitaxial and the synthetic sample to understand the difference in their GF, although differences in doping and defects were cited as potential reasons. Relatively few data are available for monocrystalline diamond probably due to high cost.

The piezoresistive property of polycrystalline diamond was studied for different structures, doping levels and temperatures using cantilever beam, three-point bending fixture and differential pressure setups. Table 2.2 lists most data published on room temperature GF for CVD diamond along with the corresponding sample specifications. A room temperature GF as high as 1000 has been attained [11]. GF is not always used to characterize the sensitivity of diamond piezoresistors. For example, applied pressure in the range of 0 - 250 mmHg to a free standing diamond membrane resulted in a room temperature sensitivity of 1.75 and 2.0 mV/V per 100mmHg for sample resistivity of 15 - 18 and 33 - 36 Ωcm, respectively.

Table 2.2 Summary of reported GF data for polycrystalline diamond.

Ref.	[8]			[6]				[10]		[11]	[17]		
additional information	<b>a</b>	was preceded by an		Grain size= 1-5 µm	Grain size= 5 µm	Grain size= 9 µm	Grain size= 5 µm			<ul> <li>undoped diamond</li> <li>mechanically polished</li> <li>doped diamond</li> <li>treated in oxygen</li> <li>plasma for 3 min</li> </ul>	Thickness = 5-10 µm		
Measurement setup	Film on oxidized Si	stressed by cantilever		Free standing film	epoxied on AIN	3-point bending		Cantilever beam		Gas pressure system	Film not removed from	Si substrate stressed by 3-point bending fixture	y point contains include
Doping	Insitu using	Boron pow-		Insitu using	solid Boron					$\mathrm{B_2H_6}$	Same as [9]		
Deposition	HFCVD	$H_2/CO/CH_4 = 100/13/7$	100/12/./	MPCVD	$H_2/CH_4=99/1$					MPCVD H <sub>2</sub> /CO/B <sub>2</sub> H <sub>6</sub> B/C=1000ppm	Same as [9]		
Substrate	SiO <sub>2</sub>			Si	Si	W	AIN			Si+20µm undoped CVD Dia- mond	Si	Si	Si
p (Ocm)	5	20	30	225	300	82	20.8	0.01	2	300	3	101	209
GF	5	10	15	50	100	75	6	2.3	5.4	1000	10	70	100

GF	p (Ocm)	Substrate	Deposition	Doping	Measurement setup	additional information Ref.	Ref.
8-10	1.2-1.5	Si	Same as [9]	Same as [9] Same as [9]	Same as [9]	Same as [17]	[18]
90-05	180-190						
90-100	195-205						
02-09	215-225						
9	9-10	Same as [8]	Same as [8]	Same as [8] Same as [8]	Same as [8]	Same as [8]	[19]
9-12	40-50						
16-20	65-75						

Table 2.3 Reported temperature dependence of GF of polycrystalline diamond for different resistivities.

ρ (Ωcm)	GF(RT)	$GF(T(^{O}C))$	Description of temperature effect	Ref.
NA	9~	~110(50)	GF increases nonlinearly	[7]
0.01	2.3	~ 2.1(60)	GF almost constant	[10]
2	5.4	13.7(60)	GF increases linearly	
300	1000	700(200)	GF decreases with T	[11]
195-205	90-100	2.7-3(200)	GF decreases nonlinearly	[18]
1.2-1.5	8-10	3.28-4.1(200)		
180-190	09-05	NA	Pressure sensitivity decreases nonlinearly	
NA	NA	NA	Pressure sensitivity constant	[20]

Based on samples with listed resistivity, GF seems to increase with resistivity. The fact that samples with the same resistivity have different GFs suggests that grain size, structure, substrate and processing maybe affecting piezoresistivity. No systematic study of these factors is available.

The piezoresistive effect of CVD diamond was studied above room temperature, up to 300°C. The reported results are summarized in Table 2.3. The samples being tested have different resistivity and possibly other characteristics such as substrate, doping method, post processing steps and contact metals. A general trend in the data could be distinguished when considering the temperature effect on piezoresistivity in relation to resistivity. The piezoresistive sensitivity seems to change from being constant with temperature at low resistivity, to increasing at intermediate resistivity and decreasing at high resistivity. The existence of films were the piezoresistive effect is preserved at high temperature strongly suggest the use of diamond piezoresistors in high temperature environments.

The results listed in Tables 2.2 and 2.3 demonstrate the feasibility and confirm the high sensitivity of B-doped CVD diamond piezoresistors. The current challenge for diamond piezoresistors is to deliver stable, reliable and reproducible performance especially under high temperature and harsh environment.

#### 2.2.2 Other diamond sensors

The negative temperature coefficient (NTC) of the resistivity of B-doped CVD diamond has been used for the fabrication of NTC thermistors by several groups [21][22][23][24]. Some of the advantages of diamond thermistors are: (i) high  $\beta$  factors in

the range of ~1000 to 5500 K [24][25], as compared to 2000 to 4000 K for conventional metal-oxide thermistors [26], (ii) operating temperature range up to 600°C in oxygen ambient (iii) chemical inertness and (iv) typical response time of 25 μs as compared to 115 ms for Pt resistive temperature detectors [21].

A hydrogen gas sensor was fabricated using a layered Pd/insulating-diamond/p-type -diamond configuration on tungsten substrate [27]. Current-voltage (I-V) and capacitance -voltage-frequency (C-V-F) measurements showed good hydrogen sensitivity for temperature and frequency as high as 85°C and 100KHz, respectively.

Thanks to its high thermal conductivity, the addition of a diamond interlayer in an Ni/Diamond/quartz (Ni/D/Q) structure was found to increase the frequency response of the Ni/Q flow sensor from 120kHz to above 220kHz [28]. This high frequency flow sensor will be useful for measuring high speed flow transitions.

Diamond radiation detectors are based on photoconduction and take advantage of diamond's large bandgap and high radiation hardness. Metal/diamond/metal structures are reported to detect the ultraviolet, X-rays,  $\gamma$ -rays, neutrons, high energy electrons and charged particle [29][30][32][31][33]. Diamond diodes [34] and p-channel MIS capacitors [35] showed good performance as UV radiation detectors.

#### 2.3 Theory of piezoresistance effect

#### 2.3.1 Definition of Gauge Factor

The gauge factor of a material is defined as the fractional change of resistance, R, of a material per unit strain, ε. The longitudinal gauge factor, GF<sub>1</sub>, for the simple geometry

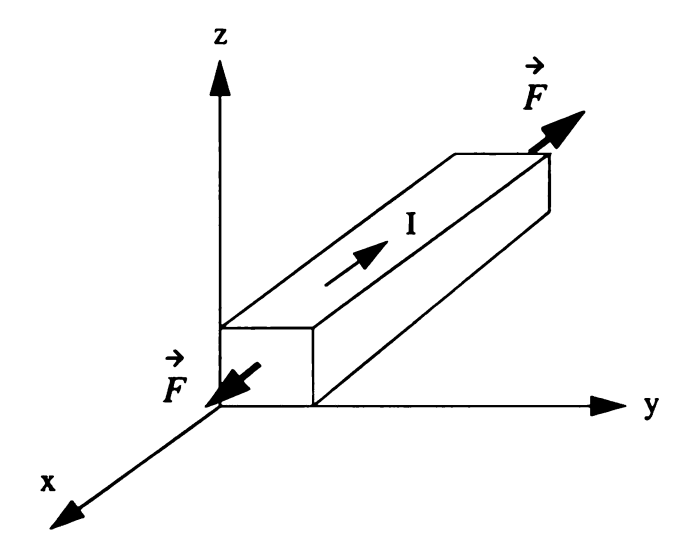


Figure 2.1 Simple geometry to define GF.

depicted in Figure 2.1 can be derived as follows:

$$R = \frac{\rho x}{yz} \tag{2.1}$$

Differentiating: 
$$dR = \frac{L}{yz}d\rho + \frac{\rho}{yz}dx + \frac{\rho x}{z}\left(\frac{-dy}{y^2}\right) + \frac{\rho x}{y}\left(\frac{-dz}{z^2}\right)$$
 (2.2)

Dividing by R: 
$$\frac{dR}{R} = \frac{d\rho}{\rho} + \frac{dx}{x} - \frac{dy}{y} - \frac{dz}{z}$$
 (2.3)

$$GF_{l} = \frac{1}{\varepsilon_{l}} \frac{dR}{R} = 1 + \upsilon_{y} + \upsilon_{z} + \frac{1}{\varepsilon_{l}} \frac{d\rho}{\rho}$$
 (2.4)

where  $\varepsilon_l = \frac{dx}{x}$ ,  $\upsilon_y = -\frac{(dy/y)}{(dx/x)}$  and  $\upsilon_z = -\frac{(dz/z)}{(dx/x)}$ . For semiconductors,

$$GF_l \approx \frac{1}{\varepsilon_l} \frac{d\rho}{\rho}$$
 (2.5)

The change of resistivity due to uniaxial longitudinal stress,  $\sigma_l$ , can also be written in terms of piezoresistive coefficient,  $\pi_l$  [36]:

$$\frac{d\rho}{\rho} = \pi_l \sigma_l. \tag{2.6}$$

Using this equation in conjunction with Hook's law,

$$\sigma_l = E\varepsilon_l \tag{2.7}$$

yields the following formula for the gauge factor:

$$GF_l = 1 + v_v + v_z + \pi_l E, \qquad (2.8)$$

where E is Young's modulus. For uniaxial stress in the longitudinal direction, the Young's modulus and Poisson ratios are given by [36]:

$$E = \frac{1}{S_l}, v_y = -\frac{S_y}{S_l} \text{ and } v_z = -\frac{S_z}{S_l},$$
 (2.9)

where  $S_v$ ,  $S_z$  and  $S_l$  are the compliance coefficients. This leads to a GF in the form:

$$GF_{l} = 1 - \frac{S_{y}}{S_{l}} - \frac{S_{z}}{S_{l}} + \frac{\pi_{l}}{S_{l}}$$
 (2.10)

#### 2.3.2 Piezoresistance in single crystal semiconductors

As seen from the definition of GF, two terms contribute to the piezoresistive response, one based on geometrical changes and the other due to a change of resistivity with strain. Since the geometrical factor is relatively low, the large GF reported for semi-conductors can only be due to the strain dependency of the resistivity. Without loss of generality, silicon, the most widely used semiconductor, is chosen as an example to explain the principle of piezoresistance in semiconductors. Since resistivity is dependent on the energy band diagram and the conduction and valence band structures are different, the explanation for the piezoresistivity is different for n- and p-type silicon.

#### ● N-type Silicon

The study of the energy band diagram for silicon as a function of wavenumber shows that the conduction band has six energy minima, along the [100], [700], [010], [010], [001] and [00T]. Figure 2.2 shows how the energy E around a minimum varies with k. In order to obtain a good insight into the three dimensional band structure, it is usual to plot the surfaces of equal energy in k-space. Figure 2.3, shows a plot of the energy valleys near the conduction band minima of Si. Applying an electric field in [100] results in electrons moving parallel to the field having an effective mass  $m^*$  and those perpendicular having  $m^*$ , where  $m^*$ , is defined by:

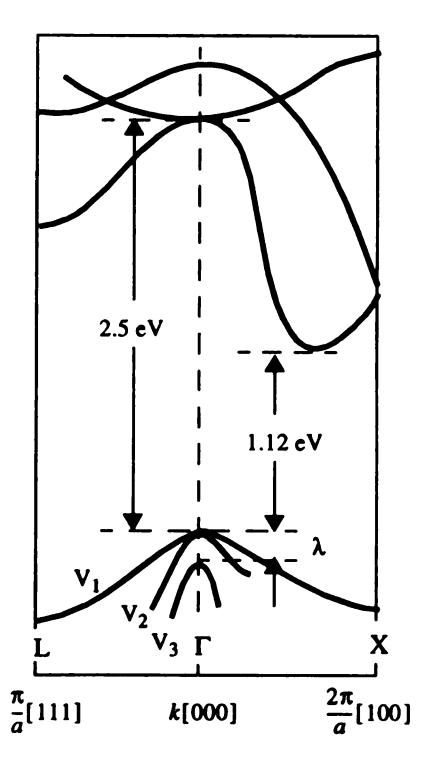


Figure 2.2 Energy band structure of Si [37].

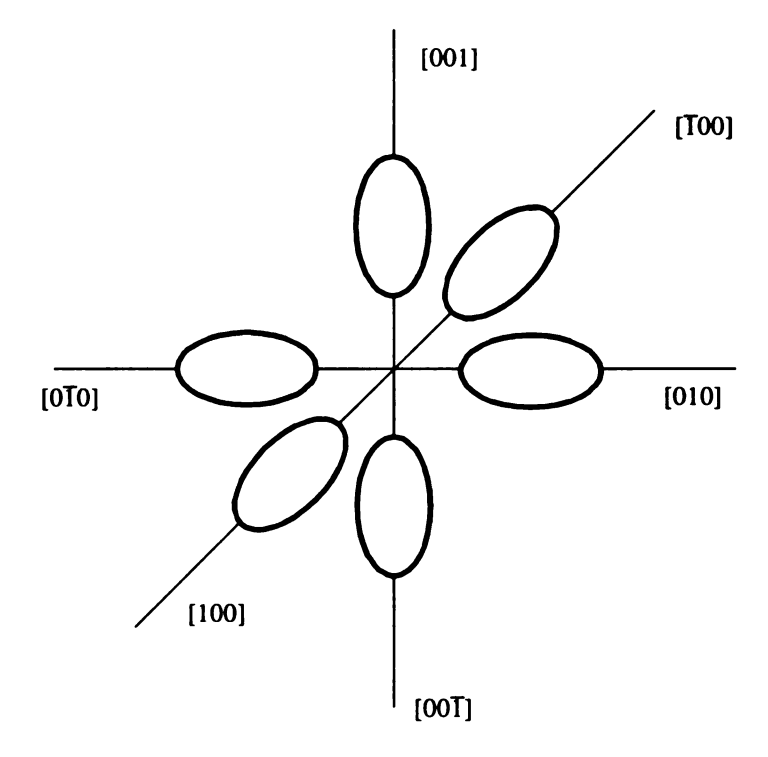


Figure 2.3 Constant energy ellipsoids near the conduction band minima of Si [37].

$$\frac{1}{m^*} = \frac{1}{\bar{b}^2} \frac{d^2 E}{dk^2} \tag{2.11}$$

and  $m^*_{\parallel} > m^*_{\perp}$  as illustrated in Figure 2.4a. The one dimensional equation of motion in each valley is written as:

$$\left(\frac{dv_x}{dt}\right)_{\alpha} = \frac{1}{m^*_{\alpha}} n_{\alpha} q E_x \tag{2.12}$$

where  $\alpha = 1, 2, ..., 6$ ,  $m_{\alpha}^*$  and  $n_{\alpha}$  are the effective mass and number of electrons in the valley, respectively. The total equation of motion is obtained by superposition:

$$\frac{dv_x}{dt} = \sum_{\alpha=1}^{6} \left(\frac{dv_x}{dt}\right)_{\alpha}.$$
 (2.13)

Under equilibrium and no strain, all valleys are equally populated. Thus,

$$n_{\alpha} = \frac{n}{6} \tag{2.14}$$

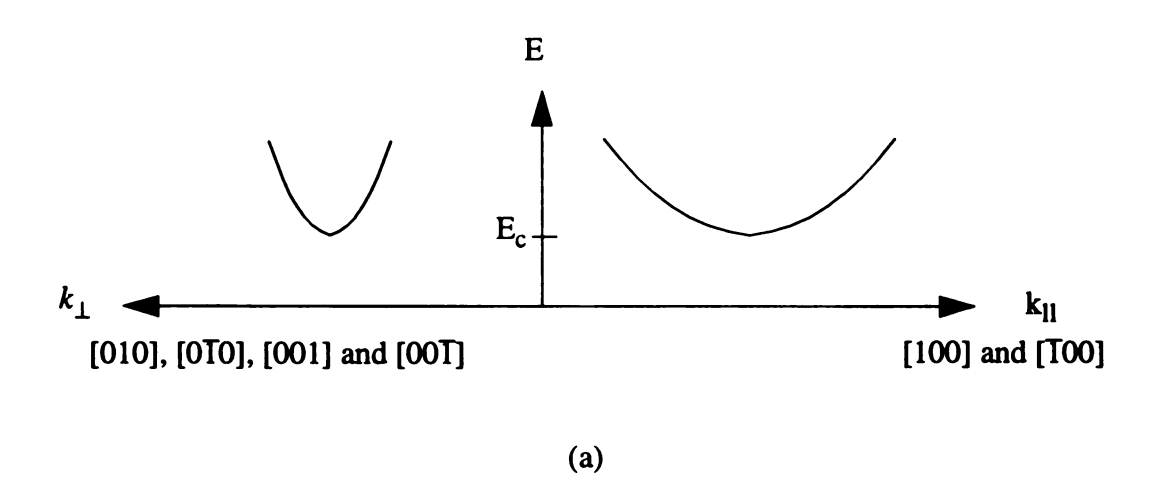
where n is the electron concentration. Since the effective mass of electrons in the [100] and [T00] minima is  $m^*_{\parallel}$  and those in [010], [0T0], [001] and [00T] is  $m^*_{\perp}$ , the equation of motion becomes:

$$\frac{dv_x}{dt} = 2\left(\frac{1}{m^*_{ll}}\frac{n}{6}qE_x\right) + 4\left(\frac{1}{m^*_{\perp}}\frac{n}{6}qE_x\right) = \frac{1}{3}\left(\frac{1}{m^*_{ll}} + \frac{2}{m^*_{\perp}}\right)nqE_x.$$
 (2.15)

The total effective mass is given by:

$$\frac{1}{m^*} = \frac{1}{3} \left( \frac{2}{m^*}_{\perp} + \frac{1}{m^*}_{\mu} \right). \tag{2.16}$$

When tension is applied in the [100] direction, assuming no change in volume, lattice spacing increases in [100] and [T00] directions, but decreases in the particular direc-



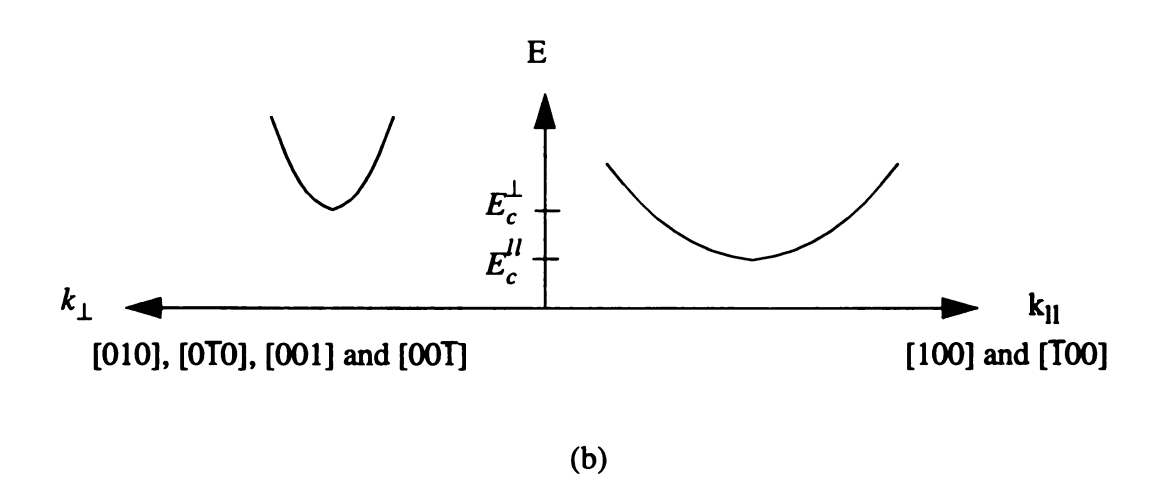


Figure 2.4 (a) Conduction band under zero strain and an electric field in the [100] direction, electrons moving parallel to the field, [100] and [T00], have larger effective mass than those moving perpendicular to the field, [010], [0T0], [001] and [00T]. (b) As a result of tension in the [100] direction, the [100] and [001] minima are lowered.

tions, [010], [0T0], [001] and [00T]. Since increase of the lattice constant in silicon was found to decrease the bandgap [38], the energy band minima in the direction of tension become lower than the other four directions, as shown in Figure 2.4b. Consequently, the proportion of electrons in the [100] and [T00] valleys, which see the larger effective mass  $m^*$ <sub>||</sub>, increases. Since resistivity is defined by:

$$\rho = \frac{m^*}{nq^2\tau} \tag{2.17}$$

where  $\tau$  accounts for inter- and intra-valley scattering, the increase of the total effective mass with tension results in an increase of resistivity.

It is worth mentioning that the effect of strain on resistivity is not limited to changing the equilibrium population of the conduction valleys. A detailed discussion of the ways in which strain can affect resistivity showed that strain-induced changes in effective mass within a valley and intra-valley scattering are small and that the effect of strain on inter-valley scattering is only important at high temperatures when inter-valley scattering is appreciable [39].

It has been observed experimentally that the piezoresistive GF depends on doping and temperature. Figure 2.5 shows these effects in terms of the factor P(N,T), defined by:

$$P(N,T) = \frac{GF(T)}{\pi_{RT}} \tag{2.18}$$

where N, is the donor concentration and  $\pi_{RT}$  is the piezoresistance coefficient at room temperature [40]. Assuming that the strain induced shift in band minima is independent of doping, the proportion of conduction electrons displaced due to strain is smaller for higher doping. Consequently, the relative change of resistivity, and hence GF, is smaller for

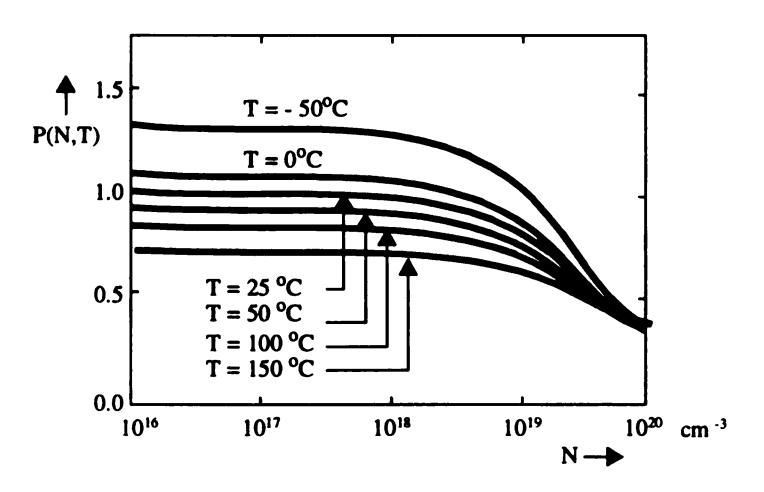
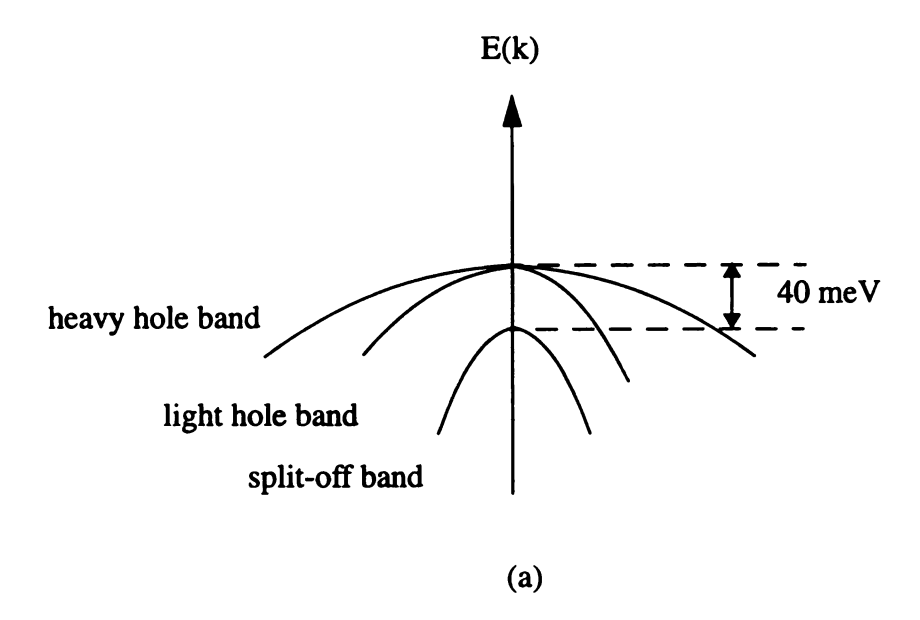


Figure 2.5 The factor P(N,T) with which the piezoresistive coefficient at room temperature must be multiplied to obtain GF at temperature T and donor concentration N in Si [40].

higher doping. The decrease of GF at high temperature is due to increased intervalley lattice scattering [41]. Since lattice scattering is more prominent at lower doping, the effect of temperature on GF is more prominent at lower doping.

## ● P-type Silicon

Experimentally, it has been found GF of p-type Si is larger than that of n-Si and thus most applications use p-Si [40]. In order to understand this difference, the effect of strain on the valence band structure must be investigated. As seen in Figure 2.2, there are two valence sub-bands, heavy- and light-hole bands, degenerate at k=0, and a split-off band 40 meV below these bands. Since the difference in the sub-bands effective masses and mobilities is not the same for all crystal directions, constant energy surface cannot be described as ellipsoids or spheres. Constant energy surfaces are warped/coupled in such a way that they have cubic symmetry individually [42]. When stress is applied, the valence bands split and redistribution of holes takes place [42]. Due to the large energy separation between the split-off band and the other two, the effect of stress on this band is usually neglected. Based on the experimental result that tension leads to an increase of the resistivity of p-Si [43], it was inferred that tension causes the sub-band with the high effective mass to move up relative to the sub-band with low effective mass [40], as illustrated in Figure 2.6. This results in an increase in the proportion of electrons having higher effective mass and consequently lower mobility and higher resistivity. The fact that the difference in the sub-band energies is larger in the [111] direction explains the higher piezoresistive effect measured in that direction [40]. Similar to n-Si, GF decreases with doping and temperature.



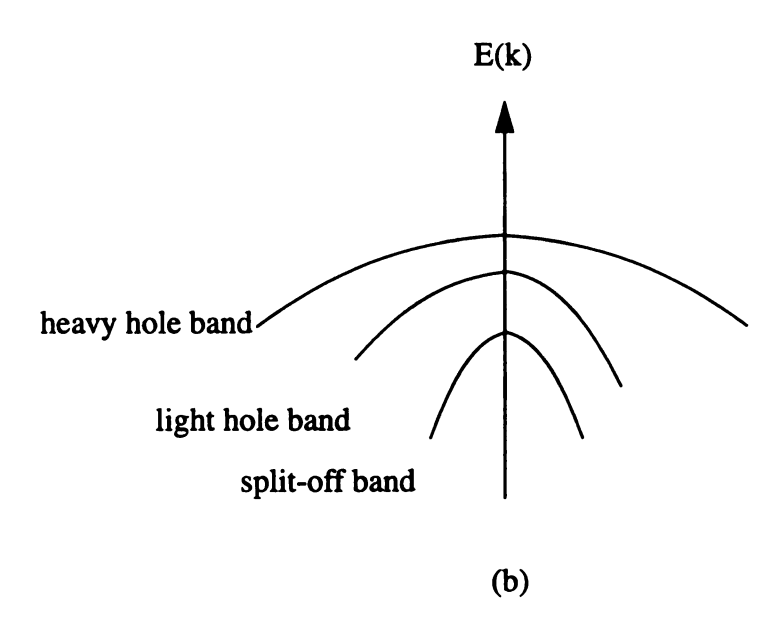


Figure 2.6 Simplified and roughly drawn valence band diagram of Si under (a) zero stress and (b) uniaxial tension.

#### 2.3.3 Piezoresistance Models in polycrystalline semiconductors

In general, polycrystalline materials consist of crystalline grains interconnected by grain boundaries. This deviation from a single crystal lattice affects conduction and hence requires a change in piezoresistive theory. Since polysilicon is the most studied polycrystalline semiconductor and both polysilicon and polycrystalline diamond have the same columnar structure, this section is devoted to reviewing the piezoresistive models of polysilicon. In order to talk about piezoresistive models for polysilicon, conduction models in polysilicon must first be covered.

#### Conduction in polysilicon

A schematic diagram of a grain and surrounding GBs in polysilicon is shown in Figure 2.7a. Grains are considered as small single crystals with the same lattice structure and hence the same energy band diagram as single crystal Si. The grain boundaries (GBs) are composed of disordered atoms and contains a large number of defects and dangling bonds which act as trapping states and/or segregation sites [44][45]. Figure 2.7b shows the corresponding band structure assuming p-type doping and neglecting the physical dimension of GB. Trapping of holes creates a potential barrier at the boundary and a depletion region into the grains [44][45]. In the early works, the junction between neighboring grains was modeled by an abrupt Schottky barrier [44][45] (Figure 2.7b). Later, Lu et al. [46] and Mandurah et al. [47] proposed to model energy band discontinuity and scattering in GB by an additional potential barrier, as shown in Figure 2.7c.

Based on the disordered nature of GBs and the presence of the GB potential barriers, it was inferred that GB resistivity is very high and that carrier transport is dominated

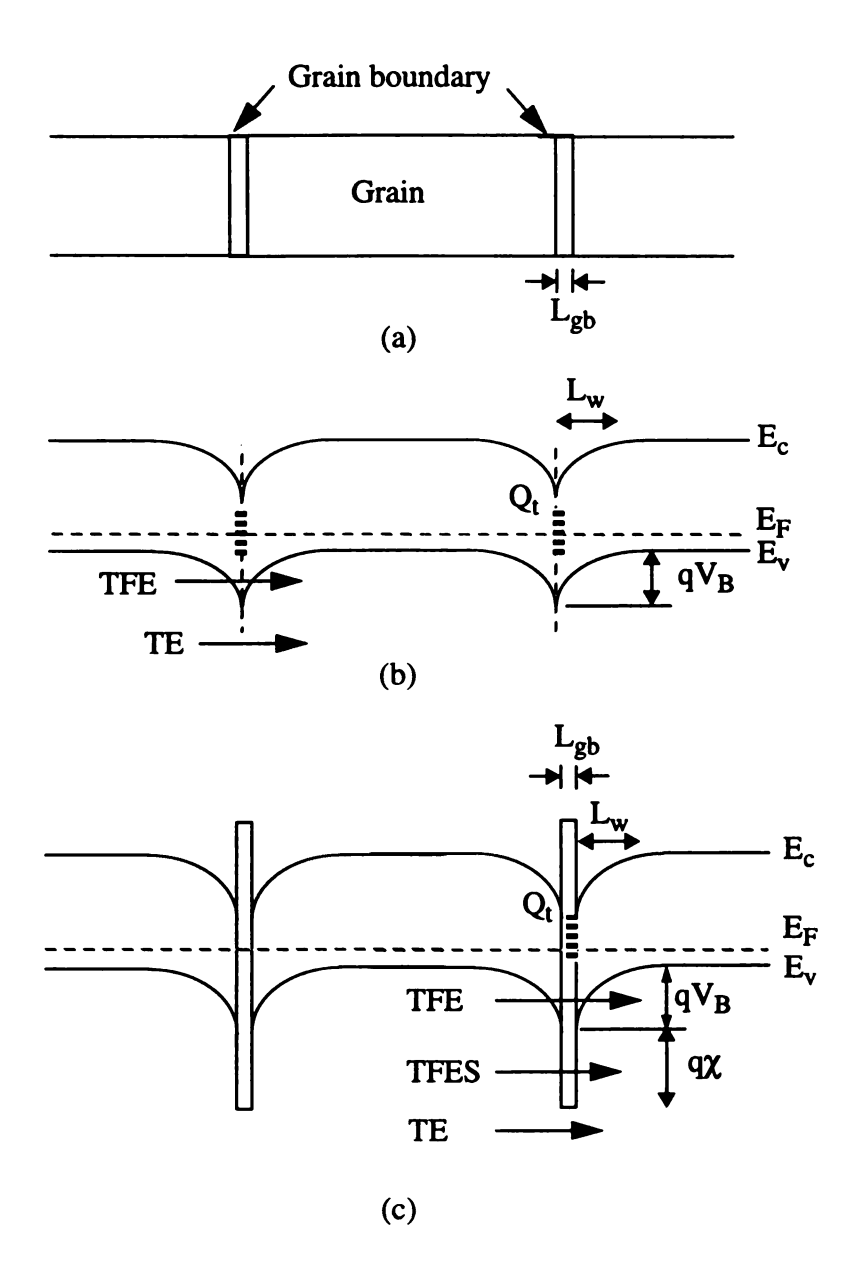


Figure 2.7 (a) Schematic of a grain and surrounding GBs in polysilicon. (b) Corresponding energy band diagram assuming p-type doping and neglecting the physical width of GB. Traps with density  $Q_t$  having energy in the bandgap capture holes creating a barrier potential  $qV_B$  and a space charge region,  $L_w$  [44][45]. (c) Additional barrier,  $q\chi$ , introduced to account for scattering in GB. The different components of carrier transport across the barrier are indicated [47].

by motion from one grain to the other across GBs [44]. Transport in the grain obeys the same principles as in single crystal Si. Transport across GB was modeled by two different approaches. The first approach considers different emission processes across GB namely thermionic emission (TE) over the GB barrier and thermionic field emission (TFE) or tunneling [45][48]. TFE was sometimes divided in two components: thermionic field emission through the space charge barrier, referred to as TFE, and thermionic field emission through the scattering potential, referred to as TFES [46][47]. In the second approach GB was regarded as an amorphous semiconductor where carriers move via hopping and diffusive scattering [49][50].

Irrespective of the approach being used to model transport across GB, the effective resistivity of a grain-GB pair can be written as:

$$\bar{\rho} = \rho_g \frac{L_g}{L} + \rho_w \frac{L_w}{L} + \rho_{gb} \frac{L_{gb}}{L} \tag{2.19}$$

where  $\rho_g$ ,  $\rho_{gb}$  and  $\rho_w$  are the resistivities and  $L_g$ ,  $L_{gb}$  and  $L_w$  are the widths of the undepleted grain, the GB and the depletion region, respectively, and  $L = L_g + L_{gb} + L_w$ . Usually  $\rho_{gb}$  and  $\rho_w$  are lumped in one term that refers to conduction in both GB and the depletion region. The exact forms for  $\rho_{gb}$  and  $\rho_w$  depend on the assumptions for each approach and on the doping concentration, grain size and orientation and density and energy distribution of traps.

## • Piezoresistance in polysilicon

Assuming that the small signal effective resistivity of a grain-GB pair can be written in terms of the resistivity of the undepleted grain,  $\rho_g$ , and that of the depletion region plus

GB,  $\rho_b$ , and that the grain and GB are uniformly strained, the longitudinal GF can be written as [51]:

$$GF = 1 - \sum_{ij}^{S} \frac{ij}{S_{ii}} (1 - \delta_{ij}) + \frac{1}{S_{ii}} \cdot \left( \frac{\rho_g \pi_{lg}}{\rho_g + \rho_b L_b / L_g} + \frac{\rho_b \pi_{lb}}{\rho_b + \rho_g L_g / L_b} \right)$$
(2.20)

where  $\delta_{ij}$  is the Kronecker delta,  $S'_{ii}$  and  $S'_{ij}$  are the compliance coefficients of crystalline Si for the axis system aligned with the crystal lattice and the axis system aligned with the longitudinal direction, respectively, and  $L_g$  and  $L_b$ , and  $\pi_{lg}$  and  $\pi_{lb}$  are the thicknesses and longitudinal piezoresistive coefficients, of the undepleted grain and the depletion region plus GB, respectively. As for polysilicon GF >> 1, the geometrical piezoresistive effects can be neglected and GF can be approximated by:

$$GF \approx \sum \frac{\pi_{lg}}{S_{ii}} \cdot \frac{1 + \alpha(\pi_{lb}/\pi_{lg})}{1 + \alpha},$$
 (2.21)

with  $\alpha = \frac{\rho_b}{\rho_g} \cdot \frac{L_b}{L_g}$ . In order to get GF of a polysilicon film, the equation for GF of a single grain-GB pair should be averaged over all grain orientations taking into consideration their distribution in the film.

The lower GF reported for polysilicon compared to single Si is consistent with the above equation as long as  $\pi_{lb}$  is lower than  $\pi_{lg}$ . Moreover, it is clear that GF changes with  $\alpha$  and hence with the relative contribution of grain and GB to resistivity. Early works on GF of polysilicon [52] assumed that GB resistance does not change with strain but found poor agreement for lower doping concentration. Assuming that (i) transport over the GB barrier is due to both thermionic emission and diffusion, (ii) the height of GB barrier is not affected by strain and (iii) the effect of strain on the grain band structure follows the band-shift and band warpage models for n- and p-type polysilicon, respectively, French et al. [51] calculated  $\pi_{lb}$ . GF values calculated using this model for polysilicon films dominated by [100], [110], [111] and random grain orientation are shown in Table 2.4. The variation of

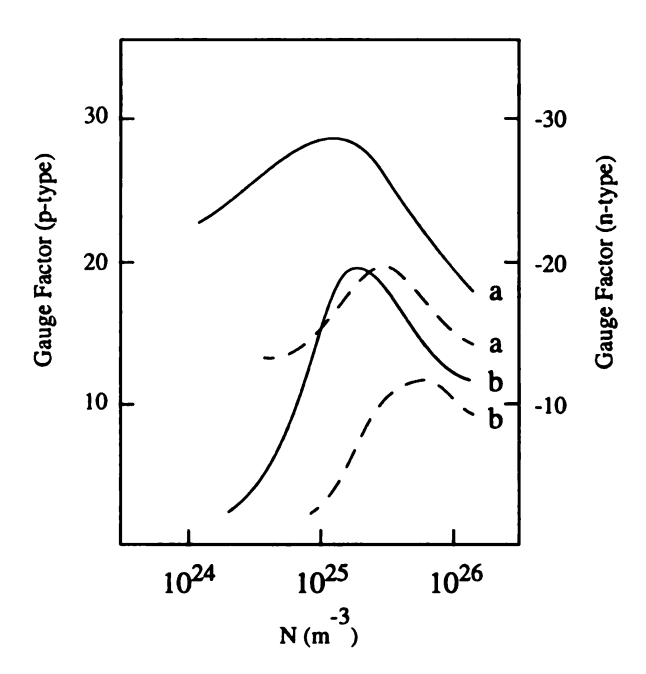


Figure 2.8 Longitudinal gauge factor as a function of doping concentration for Boron (\_\_) and Phosphorus (---) doped polysilicon. The calculation are based on a grain size of 60 nm and a texture dominated by [110] orientation. Curves b show the same calculation with GB assumed to be insensitive to strain [51].

GF with film texture is due to the anisotropic nature of the piezoresistive effect in Si. The model was also used to calculate the effect of doping on GF for a [110] textured film with average grain size of 60 nm. The shape of the graph shown in Figure 2.8 was explained by the effect of doping on the relative contribution of grain and GB to resistivity. At high doping the film is dominated by grain effects and the decrease of GF is due to the same high doping effects in single crystal Si. At low doping, GB effects are more prominent and the decrease of GF is due to the lower piezoresistive sensitivity of the GB barrier.

Table 2.4 Longitudinal GF for films dominated by [100], [110], [111] and random grain orientation [51]

Texture	[100]	[110]	[111]	Random
GF (n-type)	-97.2	-61.4	-53.4	-82.1
GF (p-type)	61.5	111.7	122.9	87.5

#### 2.4 Current Understanding of Diamond piezoresistance

#### 2.4.1 Single crystal diamond

Since the valance band structure of p-type silicon and diamond are similar to a certain degree, Taher et al. extended the interpretation of the piezoresistive property of the former to the latter [8]. Observing that the split-off band in diamond is separated from the heavy- and light-hole bands by only 6 meV, as compared to 40 meV for Si, the authors suggested that the effect of stress on the split-off band may be the reason for the higher GF in monocrystalline diamond, as compared to Si.

## 2.4.2 Polycrystalline CVD diamond

Although, p-type diamond has been used to fabricate sensors [22], heaters [25] and field emitters [53], the role of grains and GBs in electronic and mechanical properties is not well understood. Such understanding is necessary in order to establish a piezoresistive model.

## • Electrical Properties

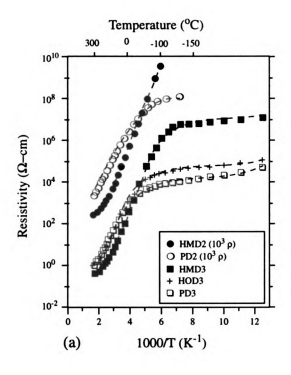
The effect of GBs on the electrical properties of polycrystalline diamond has been addressed by measuring and interpreting the effective electrical properties of CVD diamond. For the so called not-intentionally doped CVD diamond films, p-type conduction has been identified and space-charge-limited-current (SCLC) [54][55], variable range hopping [56] and GB-barrier [57] conduction mechanisms have been suggested. Poole-Frenkel conduction [12][56] was observed at high fields. Trap levels of 0.62, 1.38 and 0.95 eV [58] were evaluated from frequency and temperature conductance measurements. The existence of these traps was attributed to the polycrystalline nature of the film. Recently, contact current mode scanning force microscopy (CCM-SFM) revealed that grains have lower conductance than GBs for undoped films [59]. It is worth mentioning that the origin of conduction in the undoped films is not clear.

For B-doped CVD diamond films, frequency conduction measurements for different doping levels showed activation energies in the range of 0.18 to 1.07 eV and identified three conduction mechanisms namely band conduction, hopping conduction and frequency-dependent thermal emission of carriers from trap levels [58]. Werner and co-authors reported that variable range hopping conduction dominates at room

temperature, and that metallic conduction appears at doping concentrations about 8x10<sup>20</sup> cm<sup>-3</sup> [60][61]. Examples of all and resistivity measurements of simultaneously deposited polycrystalline and homoepitaxial films with different doping levels are shown in Figure 2.9 [62]. Comparison of the homoepitaxial and polycrystalline properties in [62] showed that:

- (i) two conduction mechanisms are present for polycrystalline and homoepitaxial films: valence band conduction at high T, and nearest-neighbor hopping conduction at low T, with a higher transition T for polycrystalline films. Additionally, impurity band conduction appears at high doping.
- (ii) the mobility of polycrystalline films is 2 orders of magnitude lower than that of homoepitaxial films.
- (iii) the temperature behavior of polycrystalline mobility could not be correlated to any of the following individual scattering models: GB-barrier, dislocations, stacking faults, impurities.
- (iv) the 3 5 times higher compensation ratio for polycrystalline films suggests trapping and/or segregation at GB.
  - (v) highly oriented polycrystalline films showed improved electrical properties.
  - (vi) parallel conduction in GB is possible.

As seen from this review, although various conduction mechanisms have been suggested to explain the measured effective electrical properties of CVD diamond, a band diagram of a grain-GB pair is not available and the question of whether conduction is higher in GB or in grains has not been answered.



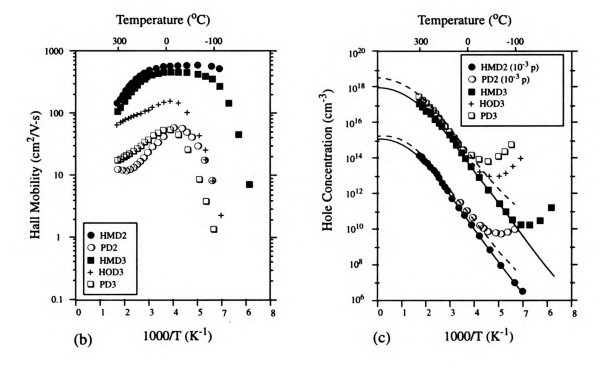


Figure 2.9 (a) Resistivity, (b) Hall mobility and (c) hole concentration measurements of simultaneously deposited polycrystalline (PD), homoepitaxial (HMD) and highly oriented (HOD) films. Films deposited in the same run have the same number [62].

### Mechanical Properties

When modeling piezoresistivity in polycrystalline material, it is important to consider the stress/strain distribution. Evidence of internal stress in CVD diamond has been reported based on Raman spectroscopy [63]. Inhomogeneous and highly localized stress distribution has been observed by several groups [63]. Larger internal stresses are observed at the growth surface as compared to the nucleation surface. Although the average internal bulk stress appears to be small, large stress concentrations near GB and twin boundaries are revealed by finite element modeling and micro-Raman [63]. Internal stresses/strains in CVD diamond are believed to be the result of lattice and thermal mismatch between diamond film and the non-diamond substrate, interaction between GBs, twin boundaries, defects associated the presence of impurities such as hydrogen, and limited growth space in continuous films. The presence of internal stress/strain gradients in CVD diamond results in non-uniform stress distributions even when a uniform external stress is applied.

#### 2.5 Diamond film technology

For the exploitation of diamond's potential as a semiconductor, successful deposition, doping, patterning and metallization processes must be achieved.

#### 2.5.1 Chemical vapor deposition of diamond

The growth of diamond by high pressure techniques is well established since the 1950s when GE researchers succeeded in transforming graphite to monocrystalline synthetic diamond [64]. The high pressure high temperature conditions required to reach the

thermodynamically stable region for diamond make such process costly and only suitable for small area coverage. Interest in diamond was renewed by successful chemical vapor deposition from hydrocarbon mixture in a lower pressure temperature domain where diamond is thermodynamically metastable [65]. Deposition rates in the range of 10 nm/hr and co-deposition of graphite jeopardized the future of CVD techniques, until the discovery that addition of atomic hydrogen allowed for preferential etching of graphite. Since then several methods and reactor configurations have been developed for decomposing carbon carrier gases and producing atomic hydrogen. Three types of growth techniques can be distinguished:

- (i) Hot filament chemical vapor deposition (HFCVD): An electrically heated filament thermally cracks H<sub>2</sub> into atomic hydrogen, activates and dissociates the hydrocarbon gases and enhances surface processes such as diffusion, chemical reactions via thermal excitation and electron bombardment [65].
- (ii) Plasma enhanced chemical vapor deposition (PECVD): Activation of the hydrocarbon gas mixture is achieved by D.C., R.F., microwave plasmas or their modifications.
- (iii) Combustion growth: The hydrocarbon gas mixture is burned at atmospheric pressure using a simple welding torch. The simplicity and high growth rate of this technique are offset by non-uniform deposition [65].

For HFCVD and MPCVD, a less than 5% methane to hydrogen mixture is usually used. Sometimes other carbon carrier gases are used instead of methane. Oxygen has been frequently added either directly, O<sub>2</sub>, CO or CO<sub>2</sub>, or as part of the carbon carrier gas. Bachmann and co-authors compiled numerous published CVD recipes and constructed the C/H/O phase diagram plotted in Figure 2.10 [66]. The diagram shows that all successful dia-

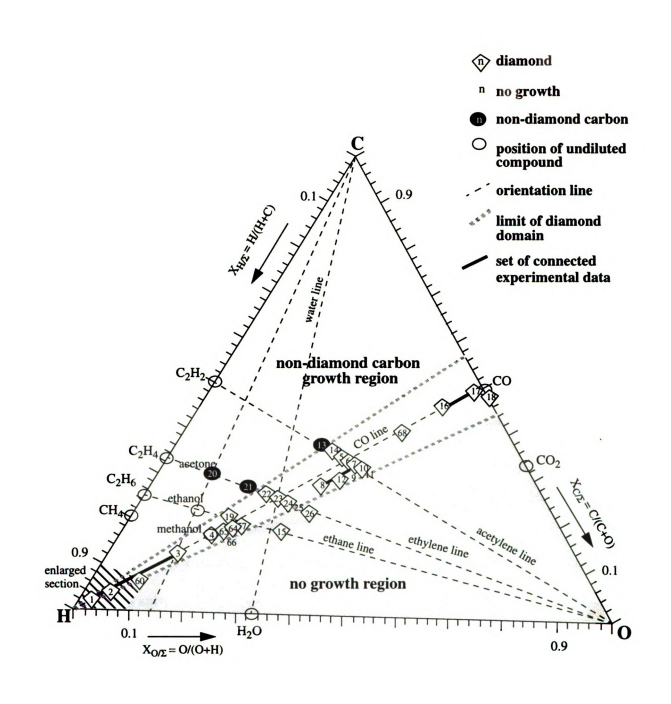


Figure 2.10 Atomic C-H-O diamond deposition phase diagram indicating the diamond growth domain [66].

mond growth experiments appear within a well defined "diamond domain." One of the general trends revealed by Bachmann's review is the improvement in diamond film quality at the expense of growth rate with the decrease of carbon content and increase in oxygen content. He correlated the temperature of the CVD gas phase with the growth rate and deposition method, as shown in Figure 2.11. The increase in deposition rate with gas temperature is generally attributed to a more efficient supply of the diamond growth species. Investigations of diamond growth mechanisms show that methyl and acetylene are the main growth species [67]. Besides gas composition and temperature, gas pressure and substrate temperature control the diamond deposition process. Successful diamond deposition was reported for substrate temperature in the range of 400 - 1350 °C where poor quality sets the low temperature limit and absence of growth the high one. Bachmann observed that the "diamond domain" narrows as substrate temperature increases. Deposition pressures in the range of 1 - 200 Torr were used depending on the substrate temperature, gas temperature and gas composition.

CVD diamond Films have been deposited on different substrate materials. Monocrystalline diamond substrates lead to homoepitaxial films whereas non-diamond and polycrystalline diamond substrates result in the deposition of polycrystalline diamond. For non-diamond substrates a nucleation procedure is necessary to produce the diamond precursors. The most widely used pre-deposition techniques are diamond powder or other types of abrasive polishing and ultrasonic agitation in a diamond powder suspension. An in-situ nucleation procedure consisting of a pre-deposition phase with 5% methane and negatively biased substrate was shown to produce a nucleation density as high as 10<sup>10</sup> cm<sup>-2</sup> on Si [68]. The first polycrystalline diamond films consisted of randomly oriented

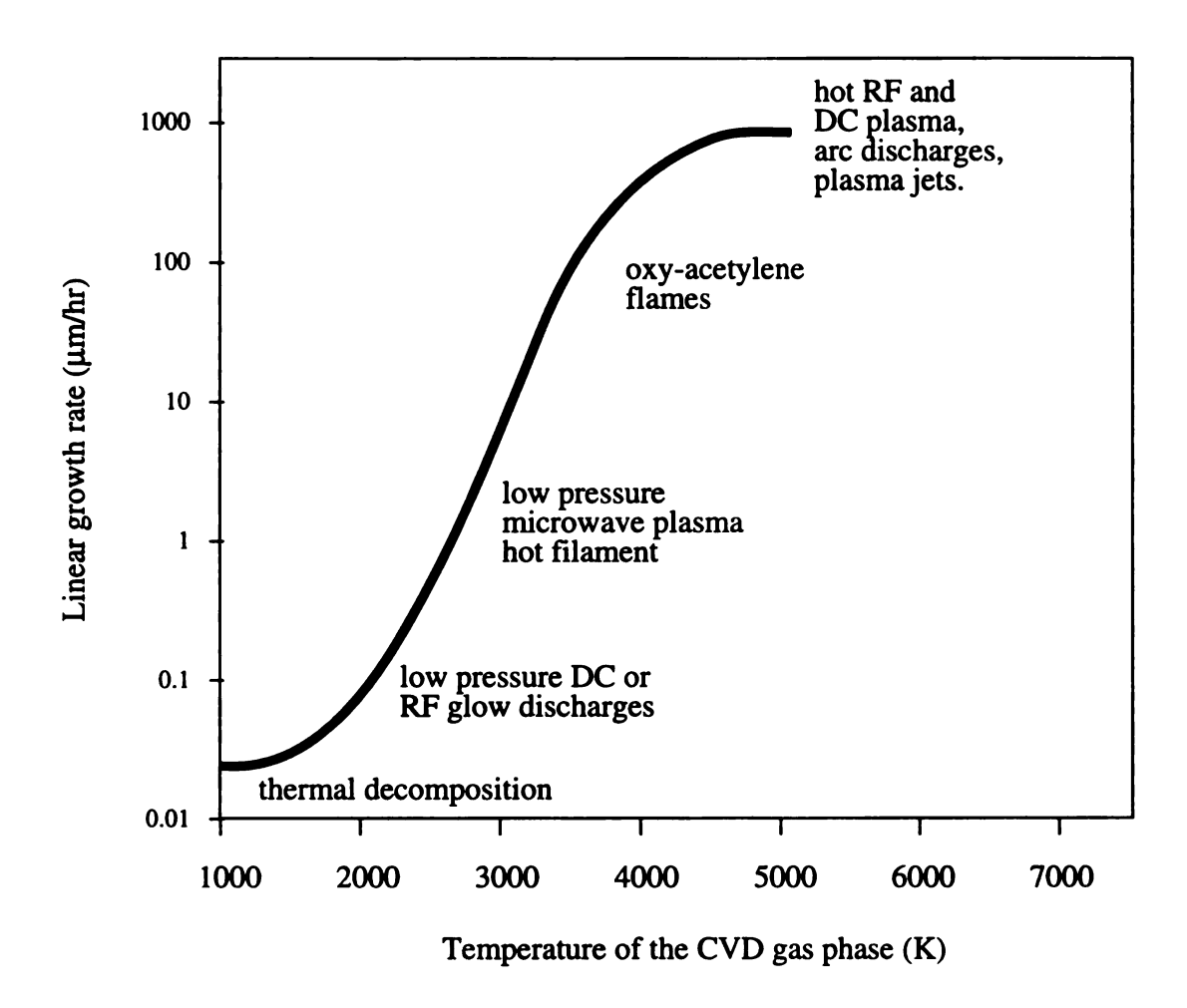


Figure 2.11 Growth rate for different CVD methods correlate with the temperature of the gas mixture needed for growth [66].

grains interconnected by grain boundaries. The search for polycrystalline diamond films with improved electronic properties lead to the development of deposition techniques for highly oriented films.

As CVD diamond technology matures designers of deposition reactors are pressured to deliver cheaper and better diamond quality. Some of the challenges they face involve achieving low temperature deposition, large area uniform films, 3D coatings, oriented and homoepitaxial films and high growth rates.

## **2.5.2 Doping**

Because the 2000 K temperature necessary for effective diffusion in diamond is too high [69], diamond doping is performed either during growth, or by subsequent ion-implantation. Boron, aluminum, phosphorus, lithium and nitrogen have been tested as dopants for diamond [70]. Currently boron is the only dopant successfully used to fabricate diamond devices and sensors. P-type conduction in B-doped films was established by Seebeck and Hall effect measurements. Diborane (B<sub>2</sub>H<sub>6</sub>) [71], boron trioxide (B<sub>2</sub>O<sub>3</sub>) [72] and boron powder [21] have been used as source for in-situ doping. IR measurements have confirmed that boron atoms occupy substitutional sites [72]. Boron incorporation was observed to be higher for [111] orientation and to increase with twinning and grain boundary (GB) angle [73]. Diamond quality, grain size, growth rate, hydrogen and oxygen contents, and twinning, dislocation and planar defect densities are affected by boron doping; but the effect varies with doping level [73][74][75][76]. The boron activation energy in polycrystalline diamond was found to decrease with doping starting at about 0.37 eV [21]. This decrease has been attributed to the appearance of an impurity band that increases in

width until the onset of metallic conduction at B concentrations greater than  $10^{21}$  cm<sup>-3</sup> [60]. Hall, resistivity and secondary ion mass spectroscopy (SIMS) measurements showed a high compensation ratio, that decreases with doping level, in B-doped polycrystalline diamond [62]. A diamond Irvin curve relating hole concentration and resistivity was compiled and is shown in Figure 2.12 [60]. Although B-doped diamond films have been extensively characterized, dopant segregation and/or trapping at GBs are neither confirmed nor refuted [62].

## 2.5.3 Patterning

Because of diamond's resistance to chemical attack, standard wet etch patterning techniques are not possible. Two patterning techniques can be applied to diamond: selective deposition and selective dry etching.

Selective deposition is achieved by selective nucleation or by masking the areas where growth is not desirable. SiO<sub>2</sub> was successfully used as a masking layer by Masood et al. [77], Roppel et al. [78] and Davidson et al. [79]. Hirabayashi et al. first nucleated the Si substrate by ultrasonic treatment, then used a photoresist mask for etching Si to 60-70nm using an Ar<sup>+</sup> ion beam [80]. A simple selective nucleation technique, which consist spinning a layer of photoresist pre-mixed with diamond powder and lithographically patterning it, was developed by researchers at Michigan State University [77]. A variation of this technique achieved a very high nucleation density of 10<sup>11</sup> cm<sup>-2</sup> [81].

Selective etching of CVD diamond with SiO<sub>2</sub> or Si<sub>3</sub>N<sub>4</sub> as mask, was performed at atmospheric pressure, in oxygen environment at 700°C, in a rapid thermal processor [77].

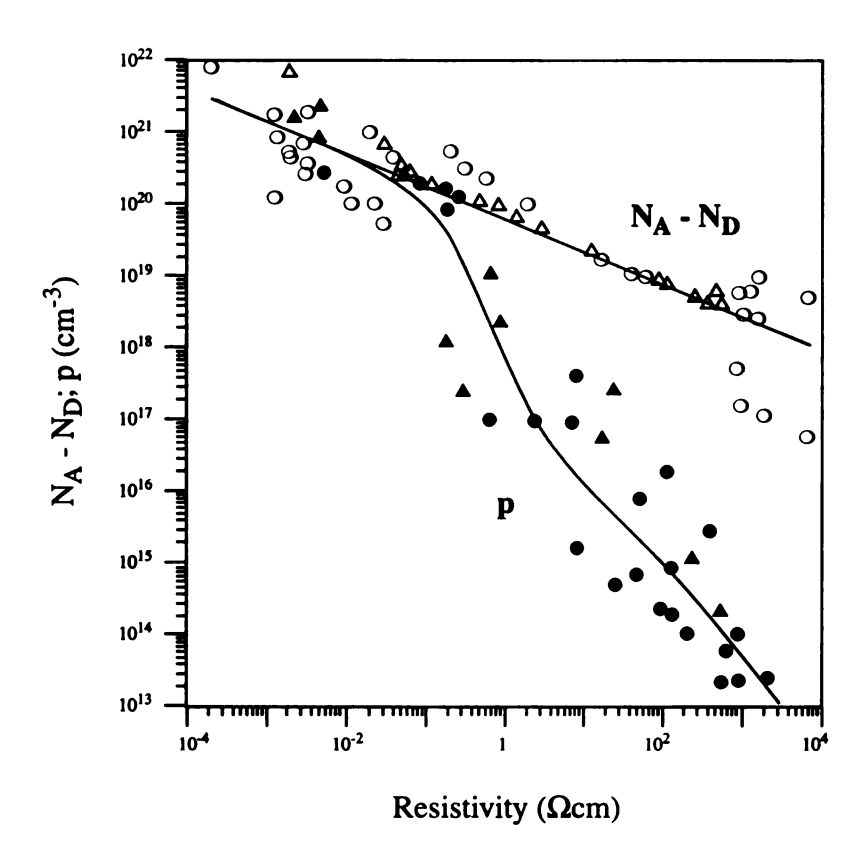


Figure 2.12 Irvin curve for single crystal ( $\bullet$ ) and polycrystalline ( $\blacktriangle$ ) B-doped diamond. The open symbols refer to effective doping concentration,  $N_A$ - $N_D$ , and the closed symbols to the free hole concentration, p [60].

#### 2.5.4 Metallization

Metal contacts to diamond have been extensively studied due to their importance in the electrical characterization of diamond films. Two general categories of metals have been used, namely carbide and non-carbide forming metals. Carbide forming metals such as Ti, Mo and Ta [82][83][84] were shown to give ohmic contacts upon anneal. Recently, the work of Tachibana et al. [85] on Ti contacts revealed that a TiC layer creates a surface layer rich in electrically active defects resulting in the observed ohmic behavior. Reported values of metal barrier heights on single crystal diamond were in the range of 1.5-2 eV independent of the metal [85]. Since the Fermi level was found to be pinned at the diamond surface [86], surface modification was suggested as a means to achieve ohmic contacts. Laser radiation [87], argon sputtering [88], hydrogenation [84] are found to results in ohmic contacts to various metals. However, it has been shown that, for non-carbide forming metals, the ohmic behavior changes to rectifying after annealing because the absence of there is no carbide layer to prevent the altered diamond surface from diffusing into the metal [88]. The metal-diamond band diagram shown in Figure 2.13 was proposed [88] to illustrate the effect of sputtering and carbide formation on the depletion width and consequently tunneling current. Ohmic contacts were observed after heavy boron doping either in-situ or implanted, regardless of the metal being used [89][90][91]. Heavy doping is believed to narrow the width of the depletion region at the metal-diamond interface which increases tunneling current. Al and Mg contacts change from ohmic to rectifying as the resistivity of B-doped diamond increases while Au contacts are ohmic even at 140 Ωcm [90]. Al/W, Ni/W and Ni/Ti/W ohmic contacts to B-diamond were stable even after annealing at 650°C for 78hrs [92]. Since the adhesion and stability of Ti/Au contacts dete-

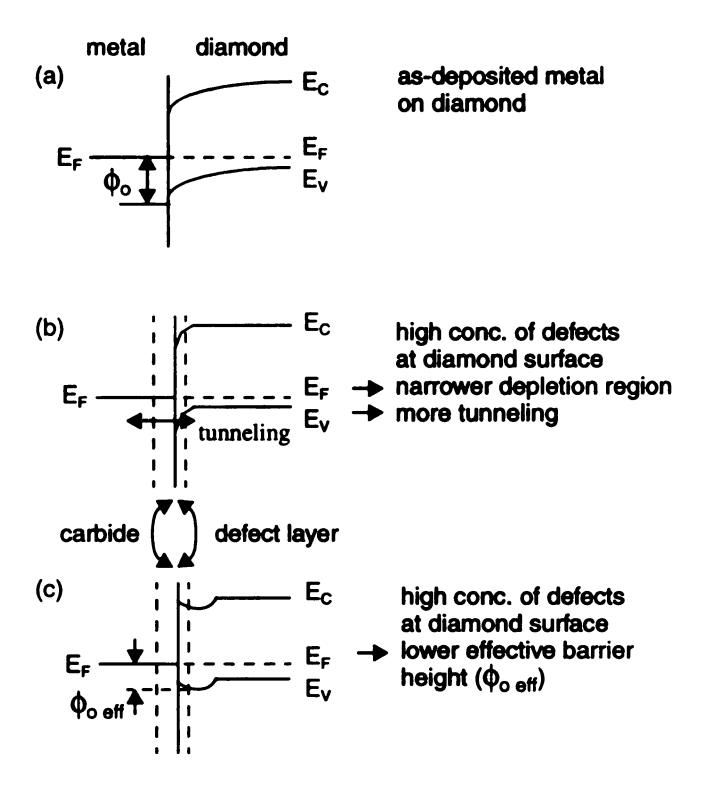


Figure 2.13 Interface band diagram of Ti on diamond: (a) as deposited Ti, (b) high concentration of electrically active defects created via carbide formation and/or ion bombardment, (c) the defects created in (b) decrease the effective Ti/diamond barrier height [85].

riorates after cycling at 400°C due to interdiffusion of the two metals, a Ti/Ti-Si-N/Au combination was tested and did not show any interdiffusion even after 100 hr heat treatment [93].

## 2.6 Summary

This overview of the current status of diamond sensors shows major achievements in sensor fabrication and characterization. Although piezoresistive diamond sensors have been successfully fabricated and a GF as high as 1000 has been measured, the observed scattering in sensor response and the role of grains and GBs in electrical conduction are still not understood.

## **CHAPTER 3**

# **Diamond Film Technology**

#### 3.1 Introduction

For the exploitation of diamond's potential as a semiconductor, successful deposition, patterning, doping, post-deposition anneal and metallization processes must be achieved. Details of the 4-inch wafer deposition system and of the initial tests performed to optimize its operation are given in the first section. Sample fabrication processes are described in the second section.

## 3.2 Hot Filament chemical vapor deposition reactor

The doped diamond films used in this work were deposited in HFCVD reactor designed and built with the help of A. Masood and D.S. Hong. This reactor extends the deposition area of a 2 inch reactor previously built at Ford Motor Co. by J. Potter and M. Tamor, to 4 inches. A schematic of the system is shown in Figure 3.1. The reaction chamber consist of an 18 inch diameter stainless steel vacuum chamber with a 10-inch door to insert the samples. Ultra-pure (99.995%) methane (CH<sub>4</sub>) and hydrogen (H<sub>2</sub>) are used as the reactant gases and their flow rates are independently controlled by MKS type 1159 mass flow controllers. The operating pressure is controlled by a MKS type 250 pressure

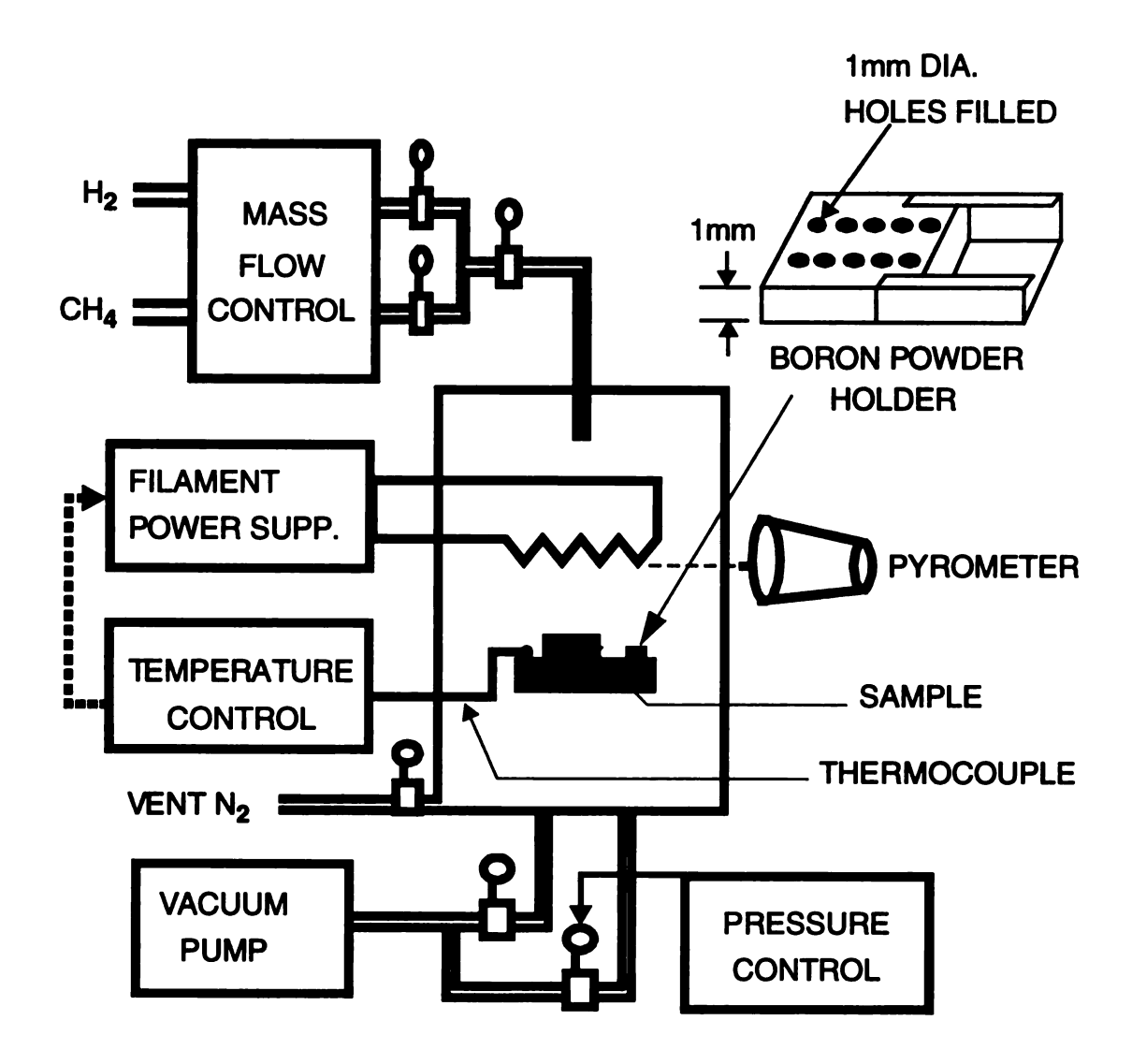


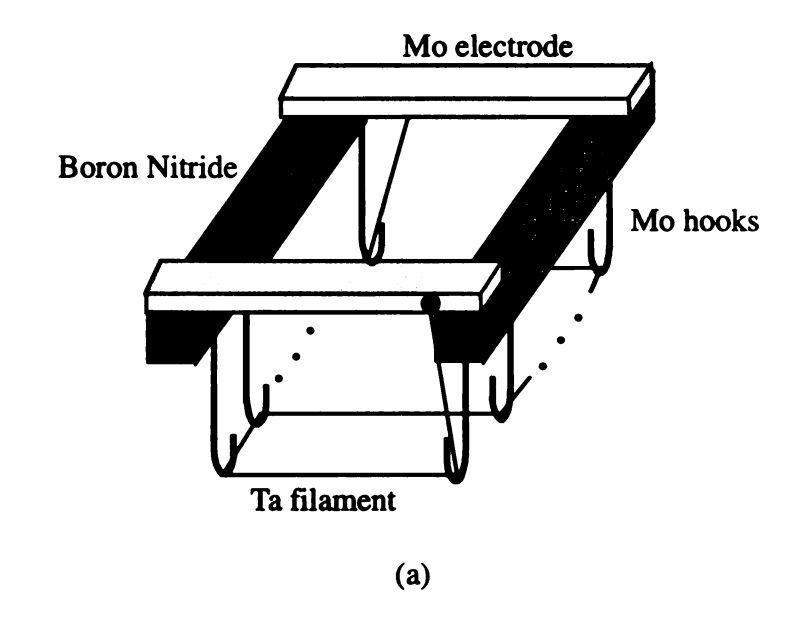
Figure 3.1 Schematic of the hot filament reactor.

controller and a type 248 upstream valve. The base pressure is measured by a MDC thermocouple vacuum gauge.

The filament assembly consists of ten 5 inch long and 0.02 inch diameter cross section Tantalum filaments mounted as shown in Figure 3.2a. The frame is made of two Molybdenum bars which serve as electrodes, and two Boron Nitride (BN) electrically insulating bars which make it possible to connect the filaments in series. Molybdenum hooks support the filaments and provide tension to diminish sagging. The filament temperature is measured optically by a dual wavelength series 8125G-CT Williamson pyrometer. Either a 4 inch Si wafer or a graphite plate is used as a substrate holder. The substrate holder is attached to a moving stage using Mo nuts and Ta rods, as depicted in Figure 3.2b. The stage is designed with the capability to adjust the filament to substrate distance, D(F,S), in the range of 0 - 3 cm. The Ta rods are used to protect the moving mechanism from the high temperature environment near the filament and to minimize heat loss from the substrate to the body of the chamber.

## 3.2.1 System testing and optimization

The 4.5 x 5 inch<sup>2</sup> filament array generates enough heat to reach very high substrate temperature without any external heating. Due to the limitation of the K-type thermocouple used for measuring the temperature, the maximum recorded substrate temperature is 1000°C. Several measurements are performed to characterize the temperature profile on the substrate as a function of operating conditions and filament aging.



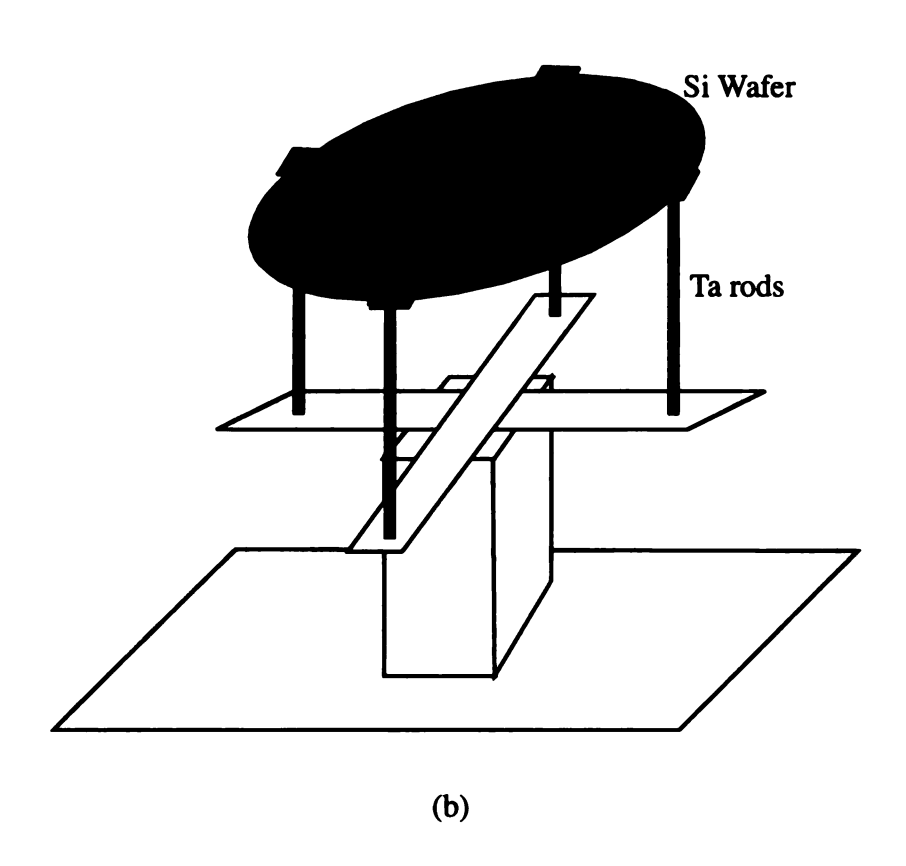


Figure 3.2 (a) Filament assembly and (b) substrate holder.

### • Effect of deposition conditions

The effect of filament temperature,  $T_f$ , filament to substrate separation, D(F,S), operating pressure, P, gas flow rate and gas composition on the substrate temperature are investigated. Major results are summarized as follows:

- (i) The substrate temperature increases nearly linearly with filament temperature, as shown in Figure 3.3.
- (ii) As D(F,S) increases the substrate temperature that corresponds to a given filament temperature, decreases as illustrated by Figure 3.3.
- (iii) Figure 3.4 shows that for the same total gas flow of 200 sccm, the presence of CH<sub>4</sub> in the gas results in slightly higher substrate temperatures.
- (iv) Using three K-type thermocouples connected as indicated in Figure 3.5, reveals that the substrate is not uniformly heated. The hottest spot in the substrate is the center point Tc1 and the temperature decreases symmetrically towards the edges. The maximum temperature gradient, Tc1-Tc3, increases with filament temperature.
- (v) Figure 3.6a reveals that, for the same filament temperature, the substrate temperature increases with P up to 50 Torr. Above 50 Torr, substrate temperature starts to decrease probably due to heat loss to the surroundings caused by increased and unconstrained gas species. The maximum temperature gradient is also affected by pressure and seems to reach its lowest value around 50 Torr.
- (vi) The effect of gas flow rate on substrate temperature was measured for filament temperatures, T<sub>f</sub>, of 2142 and 2205 °C. The results plotted in Figure 3.6b reveal that the substrate temperature does not change with flow at 2142 °C. However, at 2205 °C the effect of flow is slightly noticeable. At low flow rate, the sensitivity of substrate tempera-

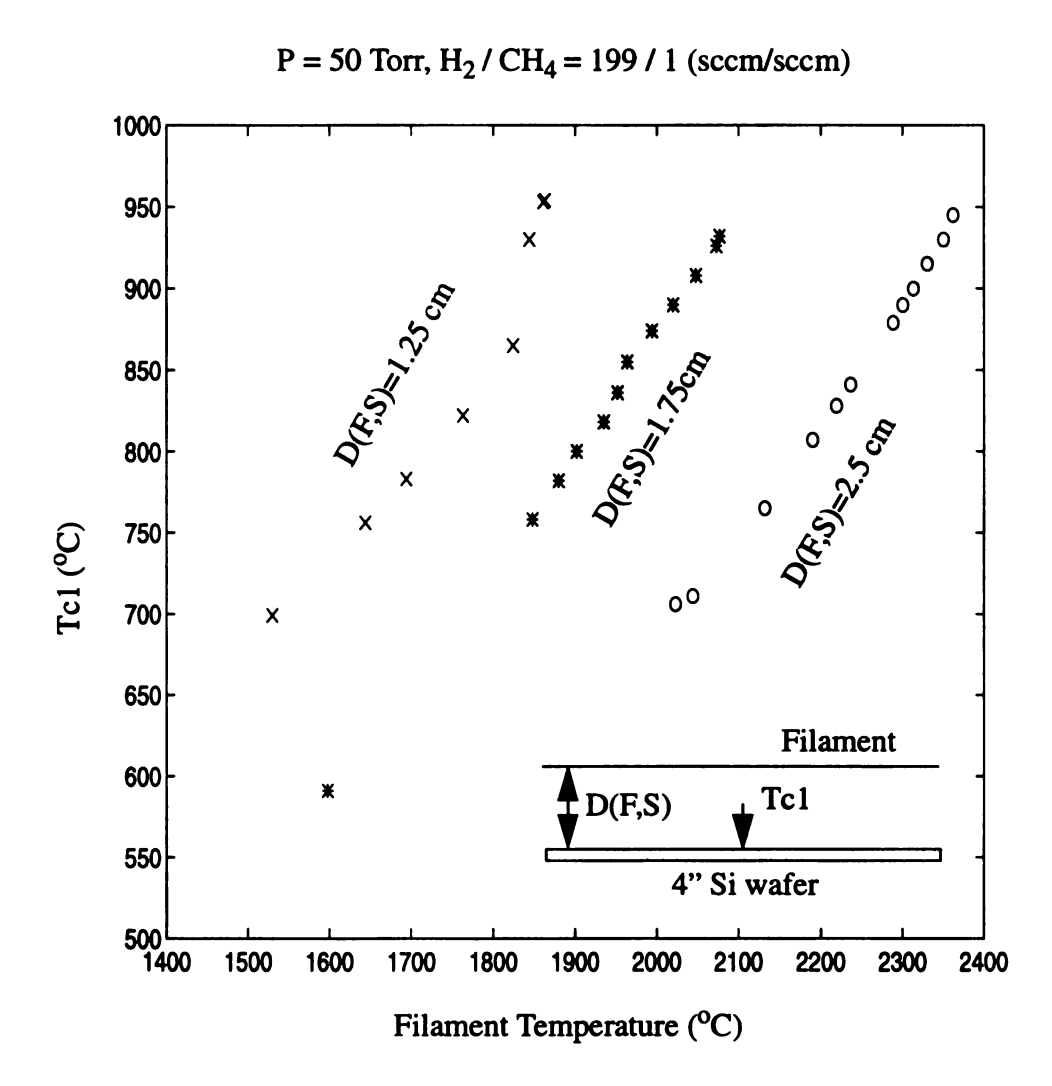


Figure 3.3 Effect of filament to substrate separation.

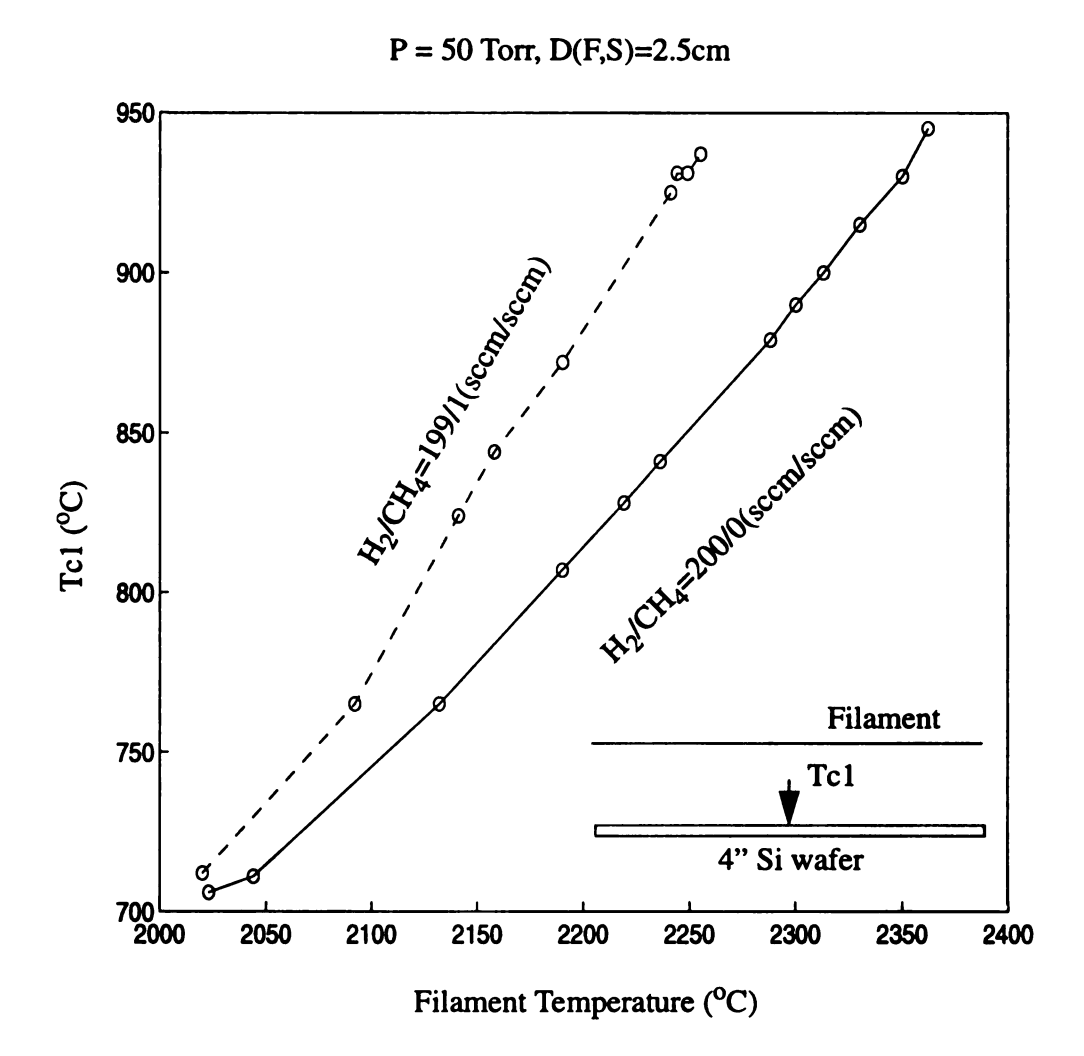


Figure 3.4 Effect of methane.

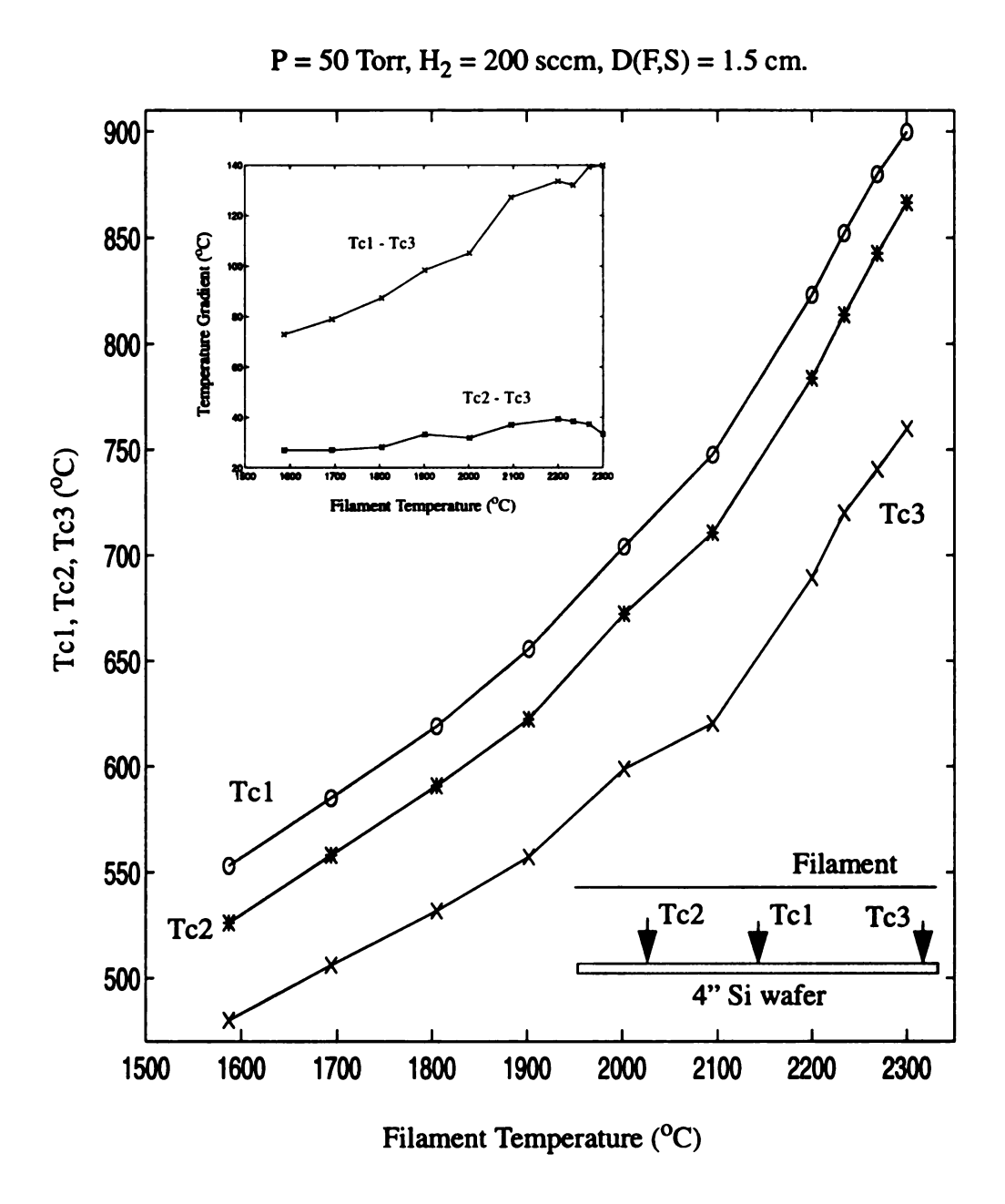


Figure 3.5 Temperature gradient over the 4 inch substrate.

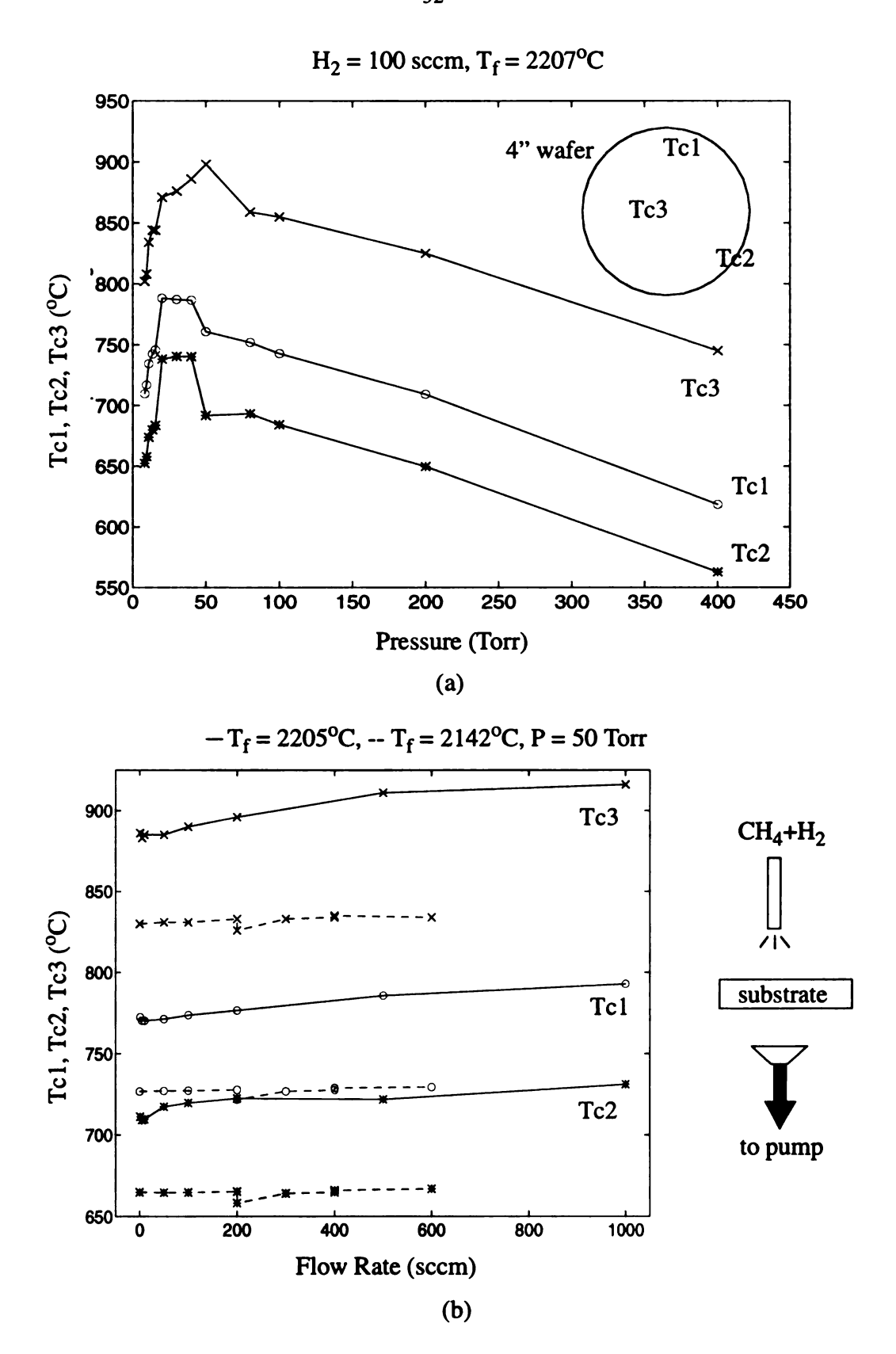


Figure 3.6 Effect of (a) pressure and (b) gas flow rate at D(F,S) = 2.5 cm.

ture is slightly higher and the temperature gradient slightly lower.

## Effect of filament aging

Before using the filament as a source of heat for the substrate, it is important to study its long term behavior. When current is increased through a new filament for the first time, its temperature first increases then it slowly decreases reaching a steady state value. These instabilities result in unstable substrate temperature as shown in Figure 3.7. However, after the first high temperature cycle, the filament temperature stabilizes. To avoid these instabilities, each new filament is subjected to a high temperature curing cycle prior to actual deposition runs. The curing cycle is carried out in H<sub>2</sub> environment and lasts for almost 2 hours. The filament temperature is increased by 10°C at a time and allowed to reach a steady state.

Besides stability, long term repeatability of the filament behavior is important. Several runs revealed that the filament temperature needed to reach a given substrate temperature increases with filament use. For example, Figure 3.8 shows that a filament temperature of 2100°C heats the substrate to 875 and 575°C after 9 and 24 hours of operation, respectively. Interestingly, the room temperature resistance of the filament also changes with use: first it increases then it stabilizes, as shown in Figure 3.9. Quick examination of cross sections of used filaments reveals they get covered by an outer shell believed to be Tantalum carbide. This change in filament material maybe the reason for the observed increase in filament resistance and change in heat radiation.

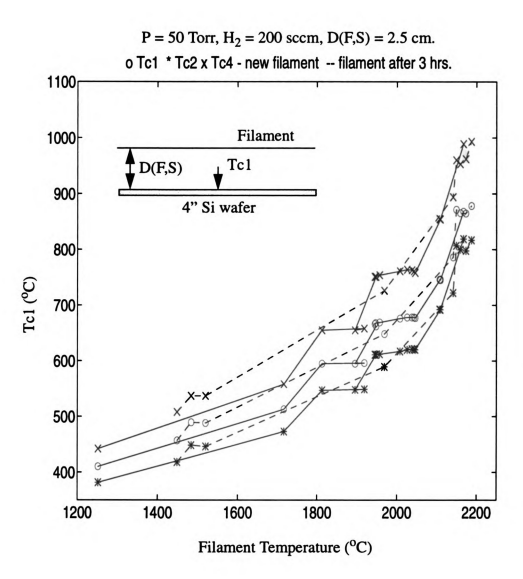


Figure 3.7 Effect of initial high temperature cure on filament.

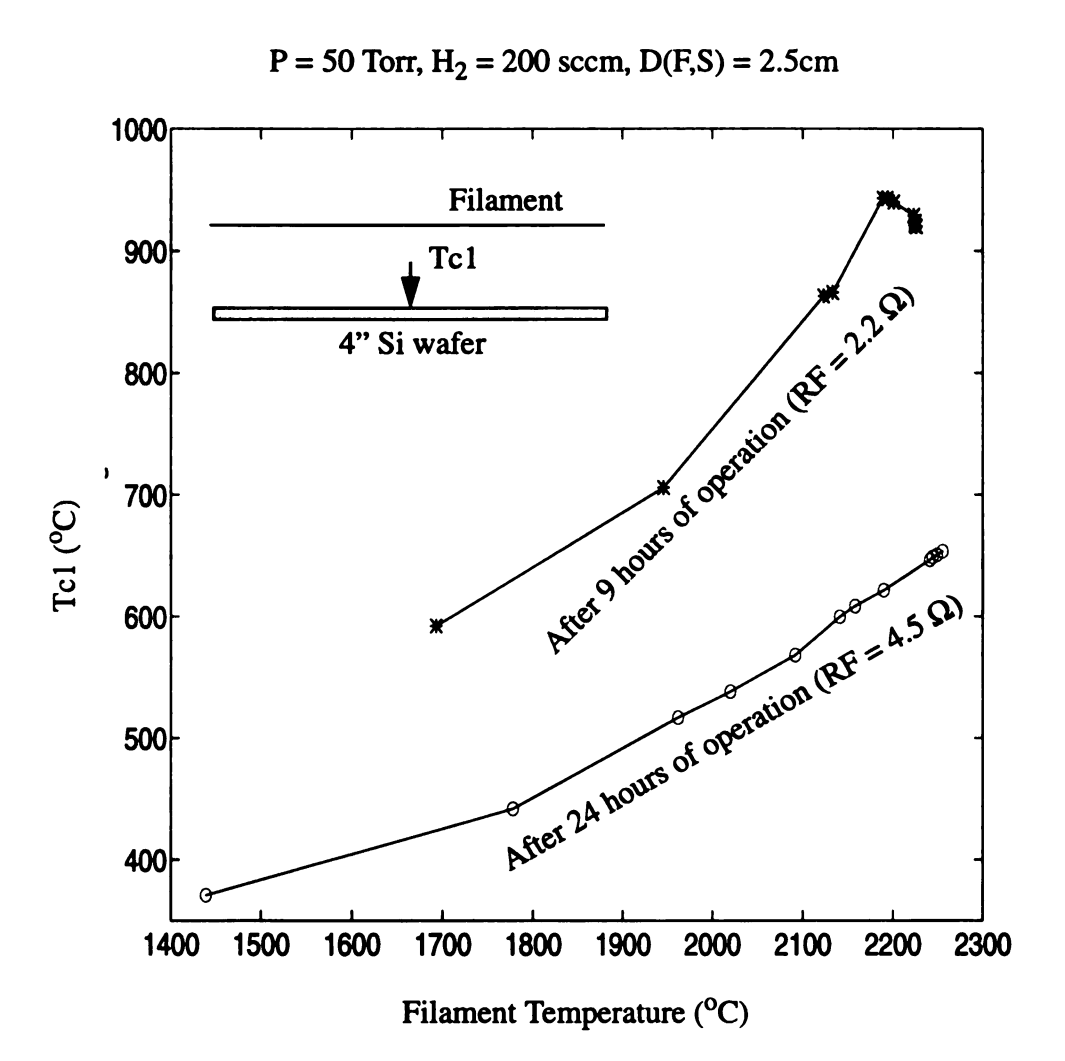


Figure 3.8 Effect of repeated use on filament.

 $P = 50 \text{ Torr}, H_2 = 500 \text{ sccm}, CH_4 = 2.5 \text{ sccm}, D(F,S) = 1.5 \text{cm}$ 

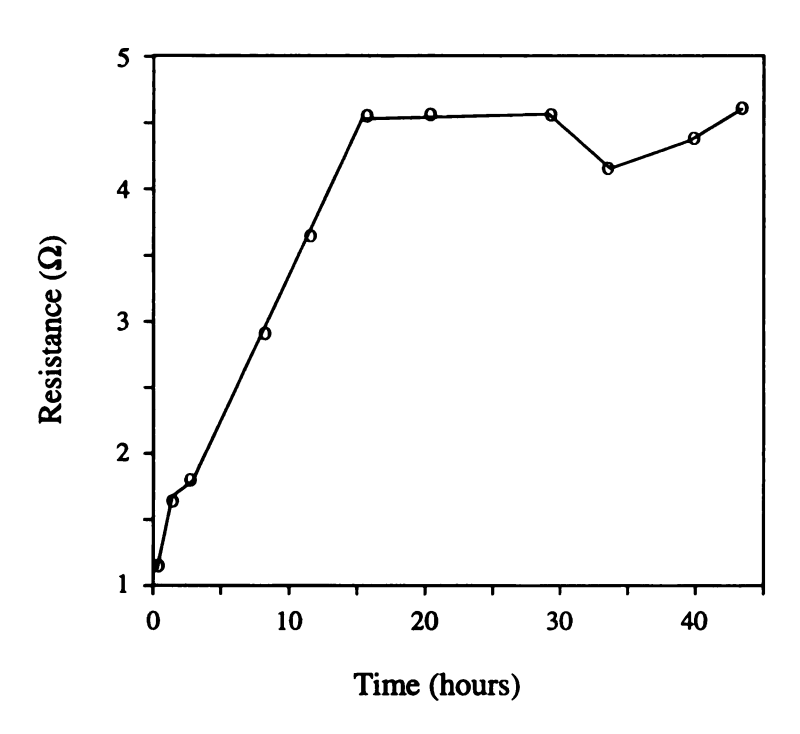


Figure 3.9 Effect of multiple runs on the room temperature filament resistance.

## ● New temperature control scheme

Based on the observed changes in filament with time, it appears that if constant filament temperature control is used, the substrate temperature will vary between runs by as much as 250°C. Whereas, if a constant substrate temperature profile is to be maintained for all runs, filament temperature may need to be varied by as much as 200 °C. A systematic study of the effect of filament temperature in the range of 2200 - 2500°C showed a variation in deposition rate but not diamond quality [94]. Consequently, it seems more reasonable to adopt a constant substrate temperature control scheme. This is achieved by using the substrate temperature signal as an input to a temperature controller, setting the set-point equal to the desired substrate temperature and connecting the generated control signal to the filament power supply.

## 3.2.2 System operation

Typical deposition conditions used through out this work are listed in Table 3.1.

The system start up and shut down procedures are kept the same for all runs as described next:

## **Curing procedure for new filaments:**

- (1) Pump down the deposition chamber to a base pressure of 10 mTorr.
- (2) Introduce H<sub>2</sub> and wait for the pressure to reach 50 Torr.
- (3) Manually increase the filament temperature until the low temperature limit of the pyrometer is reached (~900 °C).
  - (4) Manually increase the filament temperature by 25°C and wait for it to reach a

steady state value (~3 min).

(5) Repeat (4) until desired operating filament temperature is reached.

## Start up procedure:

- (1) Load the samples and doping source and adjust D(F,S).
- (2) Pump down the deposition chamber to a base pressure of 10 mTorr.
- (3) Introduce H<sub>2</sub> and wait for the pressure to reach 50 Torr.
- (4) Manually increase the filament temperature to reach the desired substrate temperature, then switch the temperature control to automatic and wait for the substrate temperature to stabilize.
  - (5) Introduce CH<sub>4</sub> and record the time of the start of deposition.

## Shut down procedure:

- (1) Turn off CH<sub>4</sub> to terminate deposition.
- (2) Keep H<sub>2</sub> on for another 5-10 min. This treatment removes a surface carbon-aceous layer believed to be the reason for the observed conduction in undoped CVD diamond films [21].
- (3) Manually decrease the filament current to zero (~20 min) and shut off its power supply.
  - (4) Evacuate the chamber and wait for the system to cool down.
  - (5) Back fill the chamber with nitrogen and remove the samples.

Table 3.1: Typical deposition parameters.

Filament temperature (°C)	2100-2300
Substrate temperature (°C)	850-900
Gas composition (CH <sub>4</sub> /H <sub>2</sub> sccm)	400/4
Filament to substrate separation (cm)	1-1.2
Base pressure (mTorr)	10
Deposition pressure (Torr)	50

## 3.3 Sample fabrication

As shown in Figure 3.10, three types of CVD films are used in this study: small grain films deposited on oxidized silicon, large grain films deposited on commercially available free standing polycrystalline diamond and homoepitaxial films deposited on single crystal substrate.

#### 3.3.1 Small grain film

The oxidized silicon substrate is selectively nucleated using a selective nucleation technique, developed at Michigan State University in collaboration with Ford Motor company. As shown in Figure 3.11, the wafer is spin coated with a mixture of diamond powder and photoresist (DPPR) then lithographically patterned. This procedure is compatible with IC process technology and ensures that no mechanical damage is imposed on the substrate. The wafer with the DPPR pattern is introduced into the deposition chamber, the photoresist burns off as soon as the filament heats up leaving the diamond seeds behind. The diamond seeds grow in all directions until a continuous 1-2µm thick

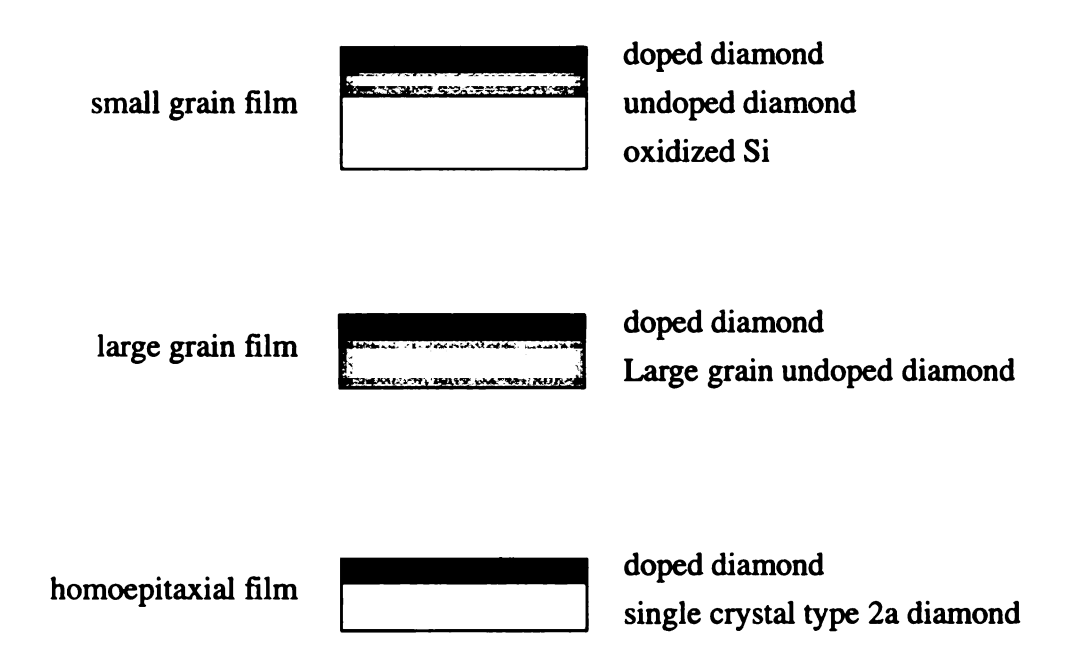


Figure 3.10 Types of CVD diamond films used in this work.



Figure 3.11 Nucleation and patterning.

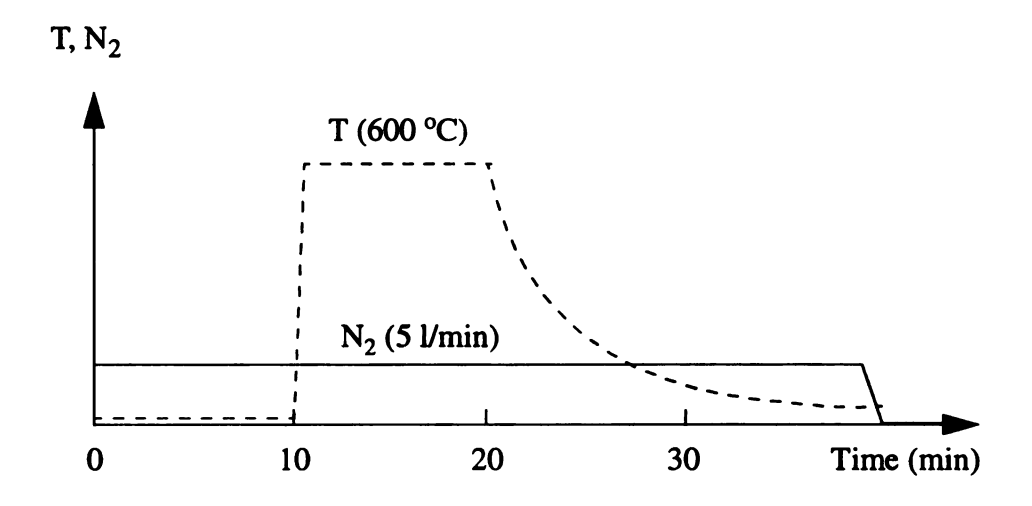


Figure 3.12 Temperature and gas profiles during RTP anneal.

undoped diamond layer is deposited. A 1-1.5 µm thick B-doped layer is deposited in a subsequent run. The undoped layer isolates the doped diamond from the substrate resulting in better electronic properties [95].

Boron doping is achieved in-situ using two types of doping sources: (i) boron powder [8], for low resistivity samples and (ii) boron wafer [96], for high resistivity samples. The doping level was varied by (i) filling less holes of the boron powder holder depicted in Figure 3.1, (ii) using a fresh vs. partially depleted boron wafer or (iii) changing the distance between the doping source and the wafer.

The films are annealed in a rapid thermal processor (RTP) in  $N_2$  environment following the cycle depicted in Figure 3.12. Evaporated Al, annealed in RTP at 450°C in  $N_2$ , is used to achieve ohmic contacts to the B-doped diamond.

Figure 3.13a shows a fully processed 4" wafer which yields 6 different samples. Details of a diamond resistor are shown in Figure 3.13b. The diamond film is characterized using scanning electron microscopy (SEM) and Raman spectroscopy (514 nm, 300 mW and spectral resolution of 4.9 cm<sup>-1</sup>). Representative SEM and Raman are shown in Figure 3.13c and 3.13d.

#### 3.3.2 Large grain film

Commercially available undoped (170 µm thick) optically smooth free standing polycrystalline diamond obtained from Diamonex is used as a substrate. A 1-2 µm Boron-doped film is grown in the HFCVD using Boron powder as a source. The deposition conditions are the same as those listed in Table 3.1, with substrate and filament temperatures of 900°C and 2300°C, respectively. The Raman spectrum of the

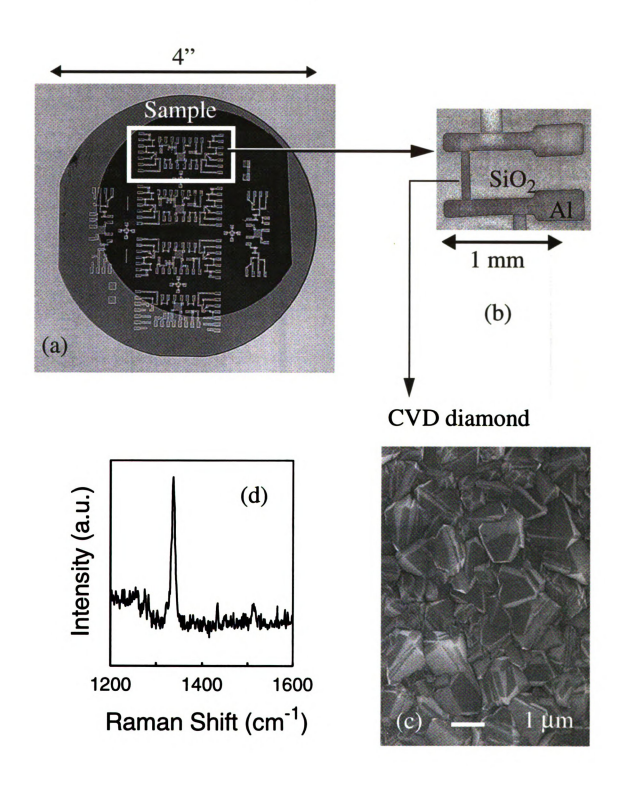


Figure 3.13 (a) processed 4" wafer, (b) CVD diamond resistor (c) SEM and (d) Raman.

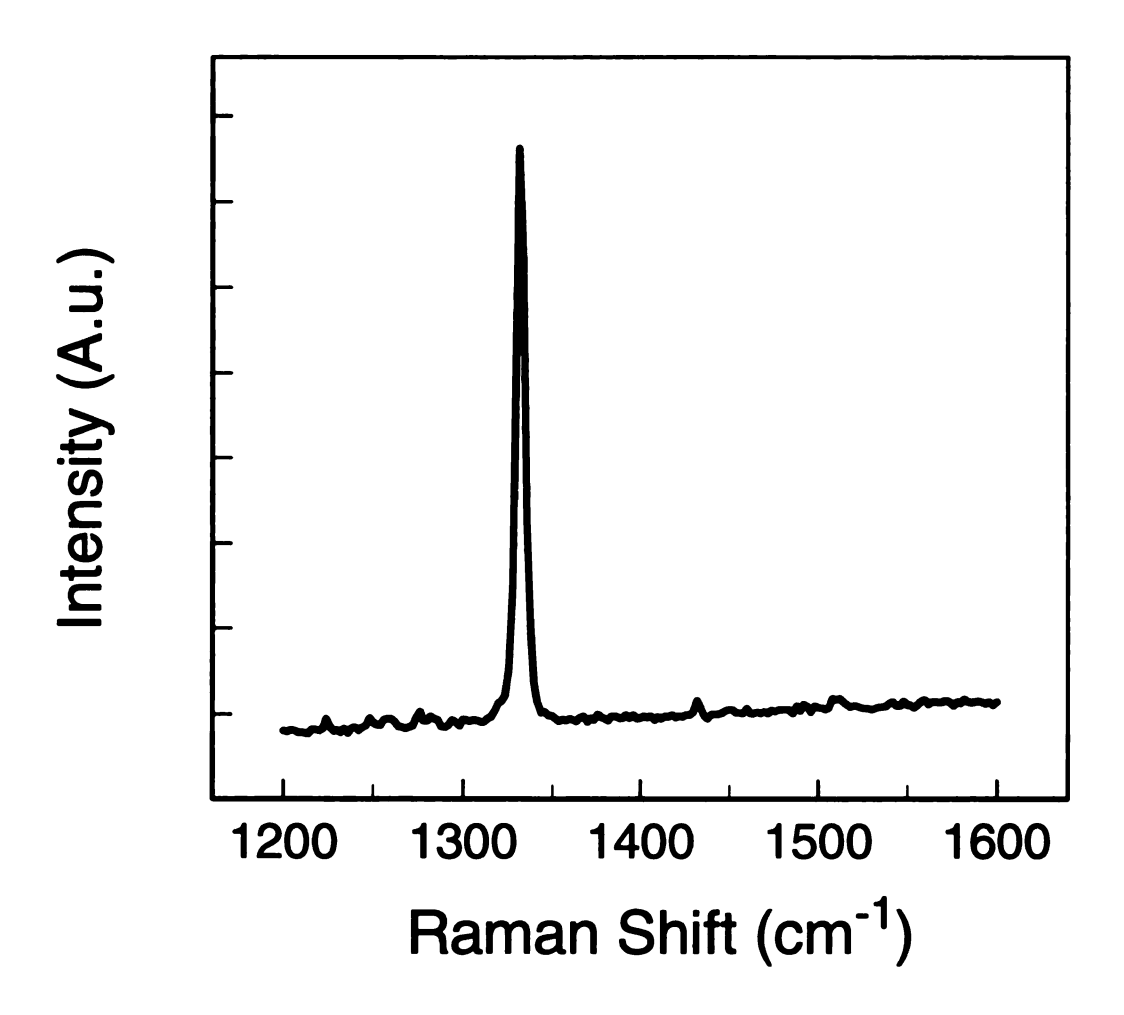
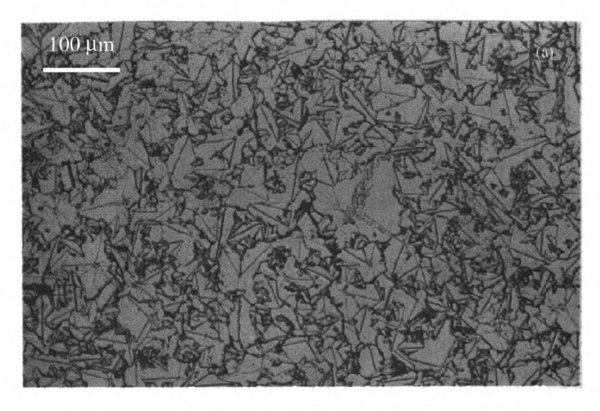


Figure 3.14 Raman Spectra of the B-doped large grain film.



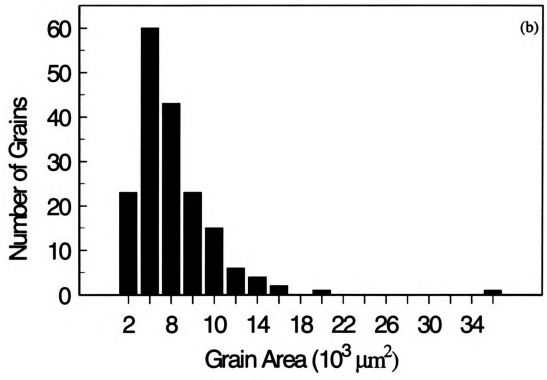
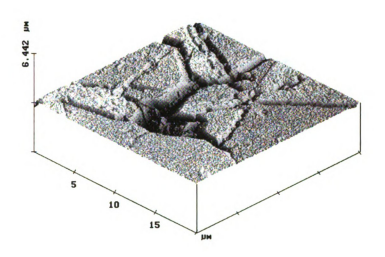


Figure 3.15 (a) Light microscope photo of doped CVD film and (b) corresponding grain size distribution.



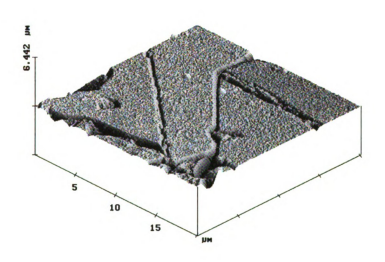
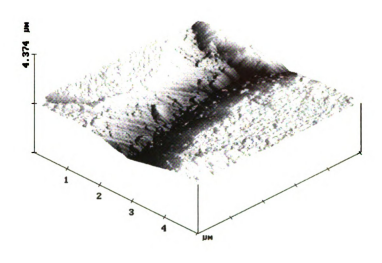


Figure 3.16 AFM of different types of GBs.



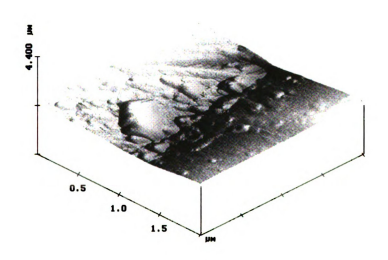


Figure 3.17 AFM of typical well defined grooves.

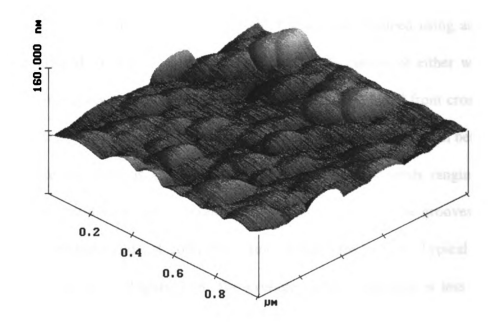


Figure 3.18 Typical intra-grain AFM.

doped film, shown in Figure 3.14, displays excellent diamond quality. Using the method of line intercepts [97] the grain size distribution of the doped film was determined from the representative light microscope photo shown in Figure 3.15a. The histogram shown in Figure 3.15b, generated by Mario Gatto, an undergraduate student at the Electrical Engineering Department at Michigan State University, indicates that the majority of grain sizes are in the range of 50 - 80 µm. The volume fraction of the inter-grain area is around 12%. Finer details of the film surface structure are obtained using atomic force microscopy (AFM). Figure 3.16 shows that typical GBs consist of either well defined grooves or irregularly shaped voids 0.2 - 0.5 µm deep, as obtained from cross-sectional analysis at 10 different locations in the sample. The grooves range in width between 0.5 -1 μm and are not steep as seen in Figure 3.17. The irregular voids ranging in width between 1.6 - 7 µm sometimes contain smaller grains or twins. The grooves and voids suggest that polishing did not completely smooth the film surface. Typical intra-grain morphology is shown in Figure 3.18. The average surface roughness is less than 5 nm. The observed microstuctures are consistent with those observed on film deposited on [111] synthetic diamond and attributed to multi-nucleation homoepitaxy [98].

#### 3.3.3 Homoepitaxial film

A 1-2 µm thick B-doped layer is deposited in a HFCVD on a 3mm x 3mm type 2a [100] oriented diamond wafer purchased from Bubbledee Harris. The doped diamond layer shows excellent Raman spectra, as seen in Figure 3.19. Metal contacts are established by sputtering a double layer of Ti and Pt.

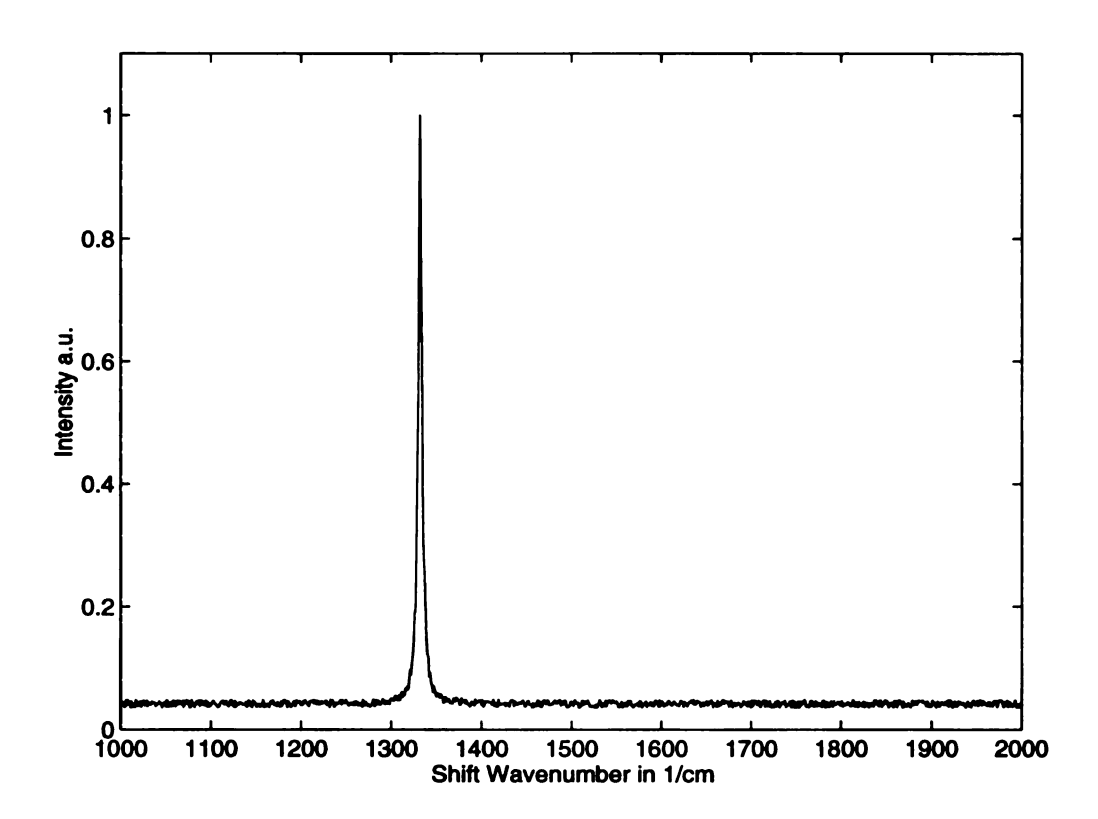


Figure 3.19 Raman Spectrum of B-doped homoepitaxial diamond.

### 3.4 Summary

In this chapter, the newly designed 4 inch HFCVD system used to deposit diamond films for this work is characterized. A special temperature control scheme is implemented to use the heat generated by the 4.5 x 5 inch filament array for substrate heating without degrading diamond quality. Sample fabrication processes namely nucleation, patterning, doping, anneal and metallization are described. Distinction is made between the three types of samples used in this work: small grain, large grain and homoepitaxial.

The films were characterized by light microscopy, scanning electron microscopy, atomic force microscopy and Raman spectroscopy.

## **CHAPTER 4**

# **Resistivity Characterization**

#### 4.1 Introduction

As resistivity is the sensing parameter for piezoresistive sensors, characterization of the resistivity of B-doped CVD diamond films is needed in order to understand the operation and improve the design of diamond piezoresistors. Although the resistivity of doped and undoped CVD diamond films has been characterized, (i) most studies are performed on films grown on conducting Si and (ii) there is a scatter in the reported resistivity behavior. Since the aim of this research is to develop stable piezoresistive sensors, it is important to (i) study the effect of substrate on conduction and (ii) understand the scattering in resistivity data.

In this chapter the effect of substrate on resistivity is studied for films grown on n-Si, p-Si and oxidized Si. The effects of annealing and electric fields on resistivity are investigated. Four point probe resistivity, potential profile, intra- and inter-grain I-V measurements are performed. A simple model that distinguishes between large grain and small grain current paths is proposed to interpret the data.

#### 4.2 Effect of substrate conduction

Some CVD diamond films generally referred to as not intentionally doped, were observed to be electrically conducting even though they were grown without a doping source [55]. Neither the origin of conduction nor the effect of the non insulating substrate are well understood. Since in this research Si is used as substrate, it is important to investigate the effect of substrate conduction on film conduction.

Undoped diamond is deposited on three substrates: n-Si, p-Si and oxidized Si, in the same run. The as grown resistivity is characterized using a four-point probe station. The results show that the films grown on p-Si and n-Si are observed to be conducting. The origin of conduction in these so called not intentionally doped films has been attributed to surface conduction as well as substrate shunting [99]. The films grown on insulating oxidized Si are not conducting which makes oxidized Si a good choice to grow diamond samples for sensor applications.

### 4.3 Effect of Annealing on Resistivity

Annealing has been observed to improve the reliability and high temperature stability of diamond resistors [21]. For CVD diamond on Si, it has been observed that resistivity increases with annealing in neutral environments at temperatures in the range of 350 -  $800^{\circ}$ C for undoped films [100][101][102], but stays constant for B-doped (10  $\Omega$ cm) [103]. The undoped films were observed to be electrically conducting even though they were grown without a doping source.

As there is no study of the effect of annealing on the resistivity of p-type diamond as a function of doping for films deposited on insulating substrates, the effect of annealing

on resistivity is studied as a function of doping level and quality, as determined by Raman, for in-situ B-doped polycrystalline diamond films deposited on oxidized Si.

## 4.3.1 Experimental details

The diamond films used in this study are of the small grain type described in section 3.3.1. In order to span a resistivity range of 0.27-535 Ωcm three series of films, OP, A and D, are doped in three different runs. The doping level and diamond quality of each sample are controlled by varying their distance from the doping source and the doping method, and their position under the filament, respectively. Samples in series OP are doped using boron powder [8]. A fresh boron wafer is used for A, whereas a boron wafer that has been partially depleted through previous runs is used for D. A four-point probe setup is used for resistivity measurement thus eliminating the problem of the effect of contact resistance [104]. The resistivity is computed using the four-point probe data and the thickness of the doped layer.

#### 4.3.2 Results

The effect of annealing on the resistivity of series OP, A and D is illustrated in Figure 4.1. For as-grown resistivity above 1  $\Omega$ cm, the resistivity after anneal,  $\rho_{aa}$ , is higher than that before annealing,  $\rho_{ba}$ . The ratio of the resistivity after anneal to that before, plotted in the inset of Figure 4.1, suggests that the effect of anneal increases with the as-grown resistivity. Samples from series A and D exhibit higher sensitivity to anneal than those from series OP.

In order to understand this difference, Raman and SEM of annealed samples are carefully studied as shown in Figure 4.2. All samples show small peak around 1520 cm<sup>-1</sup>

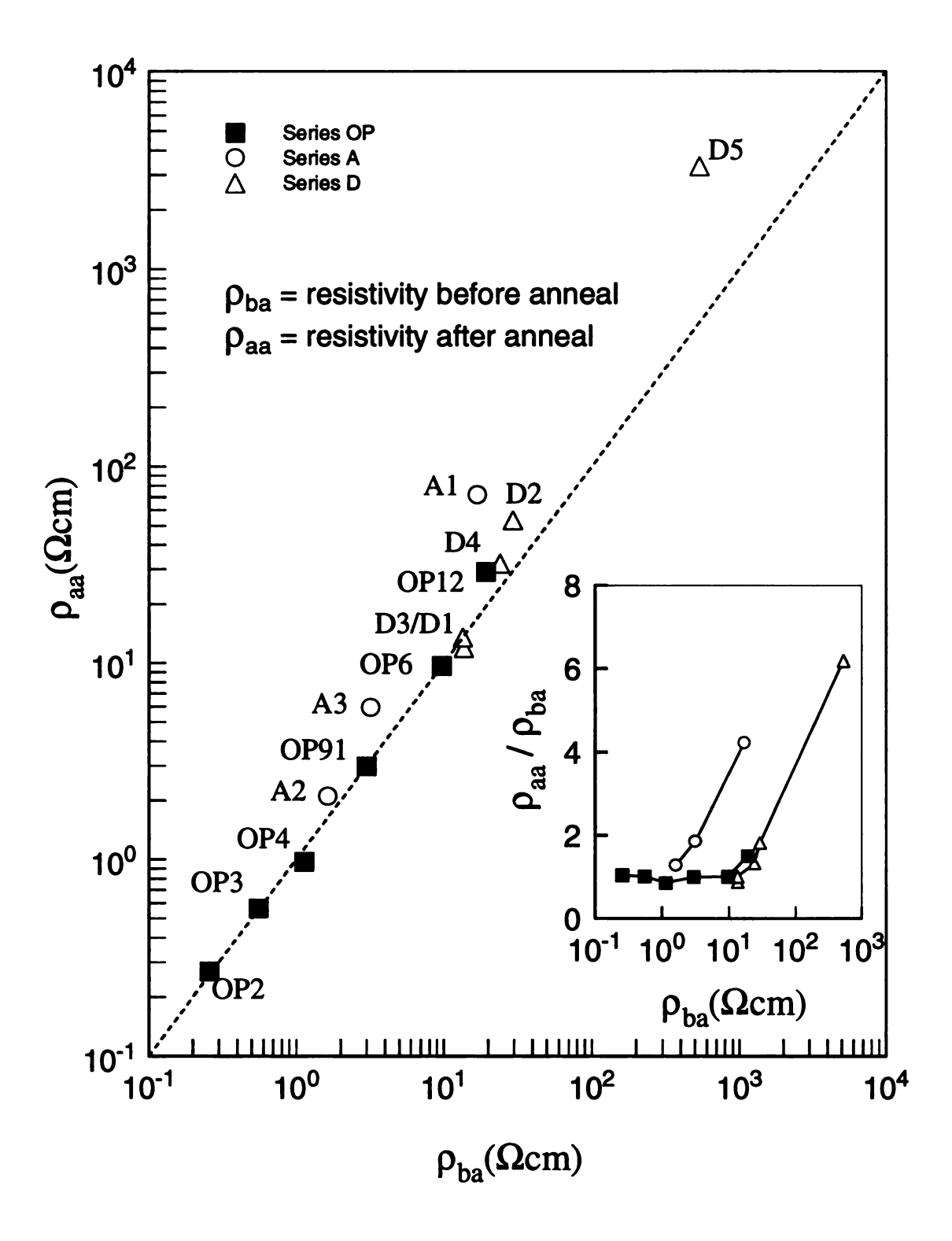


Figure 4.1 Resistivity after anneal vs. resistivity before anneal. Inset: ratio of resistivity after anneal to that before anneal.

characteristic of clusters of sp<sup>2</sup> carbon [105]. This peak tends to be very noisy and weak, indicating that the films contain relatively little sp<sup>2</sup> (to which the Raman probe is 50 times more sensitive than to sp<sup>3</sup>). The spectra show that, as doping increases, the graphitic peak decreases for all samples; whereas the diamond peak becomes sharper for series D but deteriorates for series OP and A. A similar trend has been reported [106] with the difference that high doping has been observed to result in needle-like structures. Based on the representative SEMs shown in Figure 4.2, the grain size and surface morphology are different even among samples from the same series. The Raman spectra of Figure 4.2 along with the resistivity data in Figure 4.1 suggest that there is a correlation between the Raman spectra and the effect of anneal. Samples with comparable as-grown resistivity but different diamond quality, as determined by Raman spectra, such as OP91/A3, OP12/A1 and D4/A1 reveal that the effect of anneal on resistivity increases with diamond quality. For samples with comparable diamond quality, such as A1-A3, the resistivity increase due to anneal is highest for the lowest doping level.

#### 4.3.3 Discussion

The previous results suggest that resistivity increase with anneal is more prominent for low doping level and high quality diamond. The effect of anneal on the lightly doped samples is consistent with the observed increase of the resistivity of undoped films deposited directly on Si [100]. The anneal effect was attributed to an increase in trap density due to hydrogen outdiffusion [100]. A decrease of the C-H bond absorption peaks in the IR spectra of B-doped films after anneal was reported [107]. While the role of surface conduction as compared to bulk conduction is not clear, it may be assumed that in the case

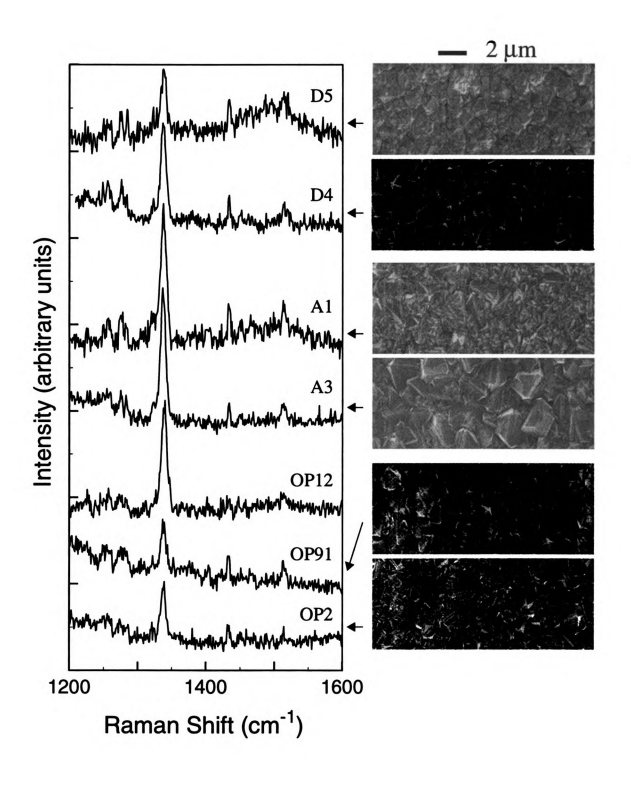


Figure 4.2 Raman spectra and SEM of samples used in the anneal study.

of doped films, the traps vacated by hydrogen outdiffusion are to be filled by holes. Assuming that the average density of traps generated by hydrogen is the same for all doping levels and that these traps may capture holes, one can expect trapping to result in wider depletion region at the grain boundary of lightly doped films [108]. This will increase the resistivity through anneal more for low doping than for high doping.

The fact that variation of resistivity with anneal is affected by diamond quality suggests that the C-H content and/or traps may vary with quality. The characterization of H-content and trap density in B-doped CVD diamond as a function of film quality is necessary to understand the correlation between annealing and diamond quality.

### 4.4 Effect of Electric Field on Resistivity

In the course of investigating the effect of anneal on resistivity, the resistance value is observed to vary with the current and/or voltage applied to measure it. Given that GF is computed from resistance data, it is important to investigate the effect of electric bias on the measured resistance. Studies of the high field behavior of the resistivity of homoepitaxial and undoped polycrystalline films have reported nonlinear characteristics. This effect has been attributed to extra carrier generation via impact ionization [109] and Poole-Frenkel conduction [12][110]. There is no similar study done for p-type polycrystalline diamond grown on insulating substrate. In this section the effect of electric field on the resistivity of p-type CVD grown on oxidized Si is investigated for different doping levels and grain size and orientation.

## 4.4.1 Experimental details

Table 4.1 lists the specifications for the CVD diamond films used in this section. With the exception of the highly oriented sample, described in [111], all films are doped in situ in HFCVD using boron powder [77]. Diamond quality and continuity are characterized by SEM and Raman. The electric field and the resistivity are computed based on I-V data and sample dimensions. The highest applied field is limited by the voltage limit of the current source used in the experiment. All measurements are carried at room temperature under atmospheric pressure.

Table 4.1 Sample Specifications

Sample	Source	Grain (µm)	Undoped	Anneal	Contact	ρ (Ωcm)
Homoepitaxial	Dubbelldee Harris Corp.	NA	Type 2a	600 °C, 10 <sup>-7</sup> Torr	Ti-Pt	1.13
Highly oriented	Kobe Steel USA.	10-100	Plasma CVD on high ρ p-Si	600°C, 10 <sup>-7</sup> Torr	Ti-Pt	136
Large grain	Diamonex Company	40-170	Plasma CVD on SiO <sub>2</sub>	600°C, N <sub>2</sub>	Al	1.26
Small grain	Michigan State Univ.	1-2	HFCVD on SiO <sub>2</sub>	600°C, N <sub>2</sub>	Al	21.13

## 4.4.2 Electric field effect as a function of doping

Figure 4.3 shows the room temperature resistivity of four small grain diamond resistors as a function of electric field. All resistors have the same dimensions and are cut out of a single wafer processed in the same run to minimize structural differences. The variation in doping level is probably due to the samples not being at the same distance from

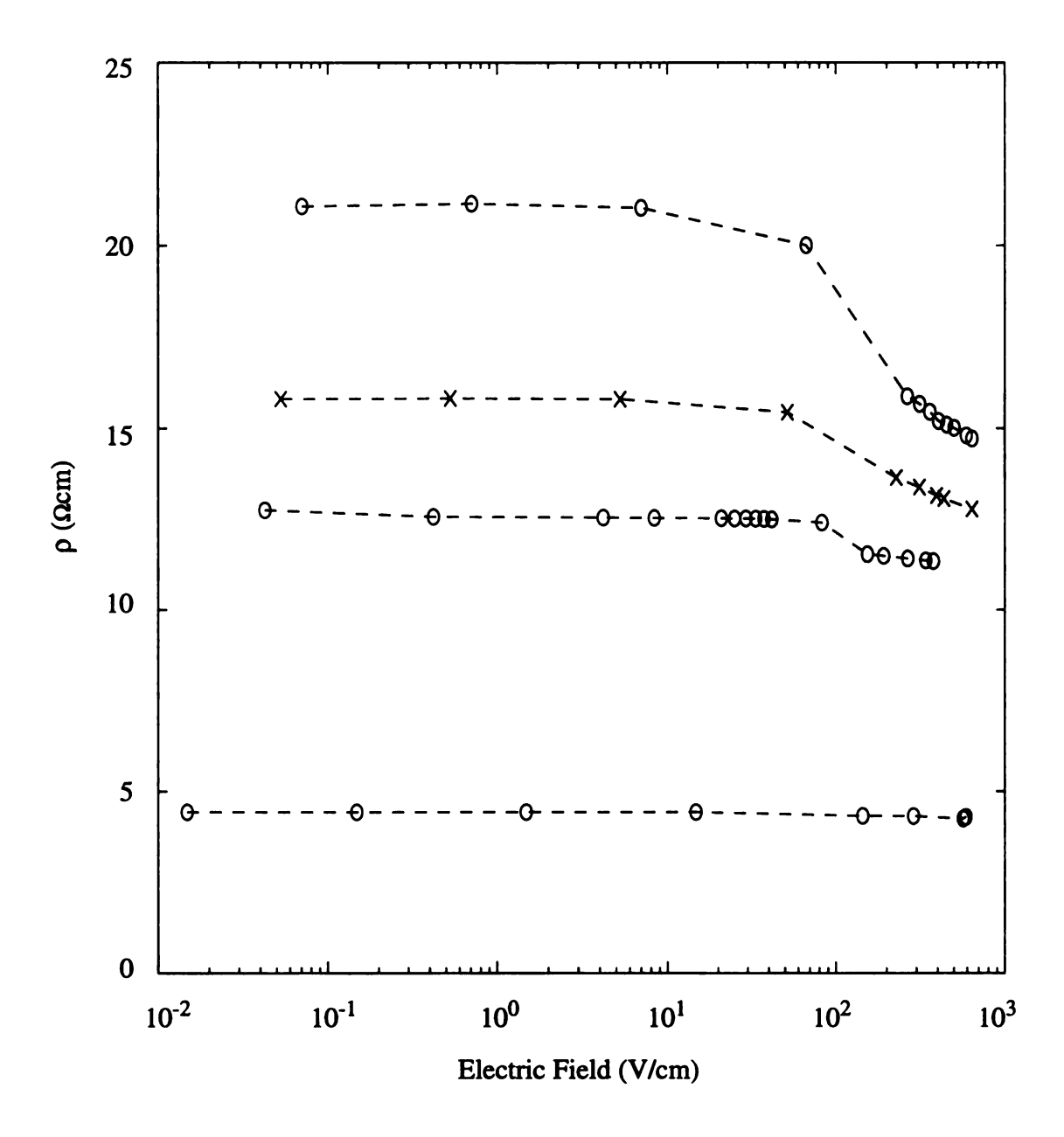


Figure 4.3 Effect of electric field on resistivity for different doping levels.

the holder containing the boron powder during in situ doping. For all samples, the low field I-V data shows ohmic behavior and the resistivity is constant. At higher fields the resistivity shows a nonlinear decrease. The resistivity of samples with lower doping starts to decrease at lower fields with a faster rate for fields up to 10<sup>3</sup> V/cm. The field effect is almost undetectable for the low resistivity sample. These results suggest that the field effect on the resistivity of the samples is sensitive to doping.

## 4.4.3 Electric field effect as a function of temperature

The effect of temperature on the observed resistance non-linearity is studied in the temperature and field ranges of 296 - 633K and 40 - 600V/cm, respectively. In order to present the resistivity data for different temperatures in one graph the normalized resistivity,  $\rho_E/\rho_{40}$ , where  $\rho_E$  and  $\rho_{40}$  denote the resistivities measured at E (V/cm) and 40 V/cm, respectively, is plotted in Figure 4.4. The resistivity starts to decrease at approximately 40V/cm for all temperatures. For each temperature, the percentage of resistivity decrease due to field is defined as  $\Delta\rho/\rho = (\rho_{40} - \rho_{600})/\rho_{40}$ . As illustrated in the inset of Figure 4.4, the resistivity dependence on field seems to be enhanced in the range of 300 - 530K but attenuated between 530-633K.

## 4.4.4 Electric field effect as a function of morphology

To study the effect of film morphology on the observed resistivity decrease with electric field, homoepitaxial, highly oriented and small grain diamond films were tested. Because of the wide range of resistivity, the normalized resistivity,  $\frac{\rho}{\rho_0}$ , where  $\rho_0$  denotes the resistivity at low field, is plotted in Figure 4.5. Whereas the resistivity of the homoepitaxial

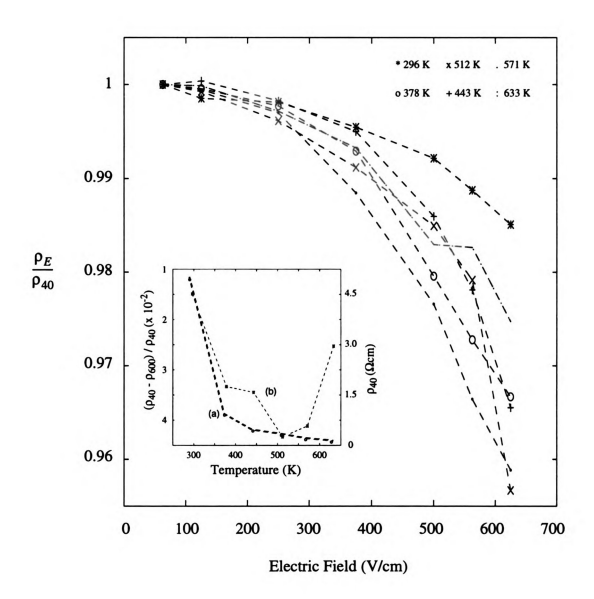


Figure 4.4 Normalized resistivity vs. field of small grain sample as a function of temperature. Inset: (a)  $\rho_{40}$  and (b)  $(\rho_{40} - \rho_{600}) / \rho_{40}$  as a function of T.

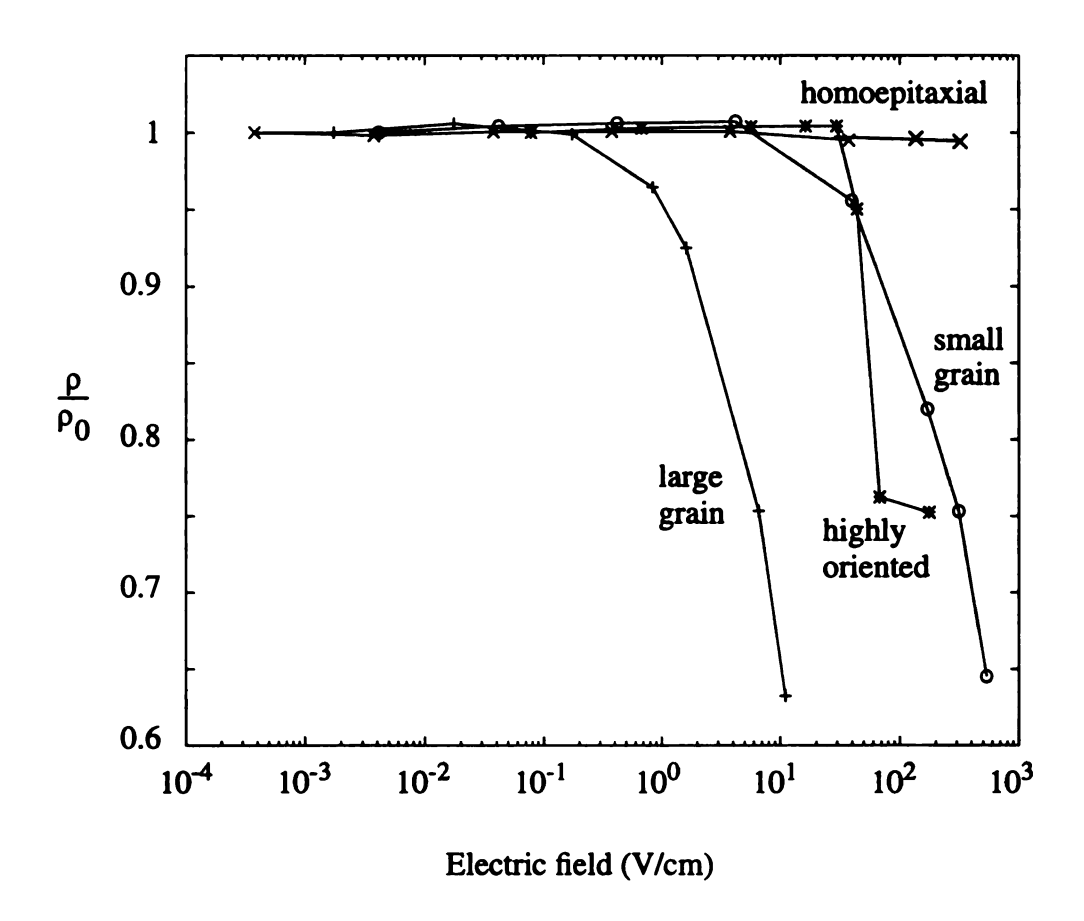


Figure 4.5 Ratio of room temperature resistivity to low-field resistivity for B-doped homoepitaxial, highly oriented, large grain and small grain films.

sample is constant for all fields, all polycrystalline films show a decrease of resistivity with increasing electric field. Since the electric field effect on resistivity is more prominent at low doping, the resistivity of the highly oriented film is expected to start decreasing at a lower field followed by the small grain then the large grain film, based on their resistivities as listed in Table 4.1. The data in Figure 4.5 differs from this expectation, which suggests that besides doping, the onset of resistivity decrease with electric field is probably sensitive to grain size and orientation.

#### 4.4.5 Discussion

The measurements presented in this section reveal that the resistivity of B-doped polycrystalline diamond decreases with the electric field applied to measure it. The onset and the rate of the observed resistivity decrease seems to be sensitive to doping level, temperature and morphology. The field at which the resistivity starts to decrease is lower than the 10<sup>5</sup>V/cm reported for not intentionally doped polycrystalline diamond films and attributed to Poole-Frenkel conduction [12]. It is worth mentioning, however, that the resistivity of the films in [12] is at least three orders of magnitude higher than the samples used in this study and that neither the origin of conduction nor the effect of the non insulating p-type Si substrate are well understood [12]. The homoepitaxial film data obtained in this study is consistent with the report that non linear field effects, due to impact ionization, were not observed for p-type homoepitaxial CVD diamond below 10kV/cm [109].

In order to determine if Joule heating is the reason for the observed field effect, the temperature of the samples is monitored using a K-type thermocouple. Since no

temperature increase is detected, Joule heating is excluded. Comparison between the data for homoepitaxial and polycrystalline B-doped diamond films suggests that the observed decrease of resistivity with electric field is related to the presence of grain boundaries. Consistently with the report that highly oriented films have closer electrical properties to homoepitaxial films than randomly oriented [5], the field effect on resistivity is less prominent for the highly oriented film. The difference between the effect of field on the resistivity of both randomly oriented large and small grain films is unclear. As further discussion of the field effect on resistivity requires exact knowledge of the role of GB in electrical conduction in B-doped polycrystalline diamond, intra- and inter-grain conduction are studied in the next section.

## **4.5 Current Flow Study**

The effect of GBs on the electrical properties of polycrystalline diamond has been addressed by correlating measured electrical properties and structural properties [112], by comparing the properties of single crystal and polycrystalline diamond [113], or by fitting measured electrical properties to known conduction models [114][115]. Although these studies suggest possible conduction mechanism(s) in polycrystalline diamond, they do not provide a direct experimental characterization of the effect of grains and grain-boundaries on current flow.

Intra-grain conduction was studied by making electrical contacts to 3D isolated diamond micro-crystals [116]. Since continuous films are used in diamond sensors, it is important to characterize intra- and inter-grain conduction directly in a continuous film. For the first time, the contribution of grains and GBs to electrical conduction in

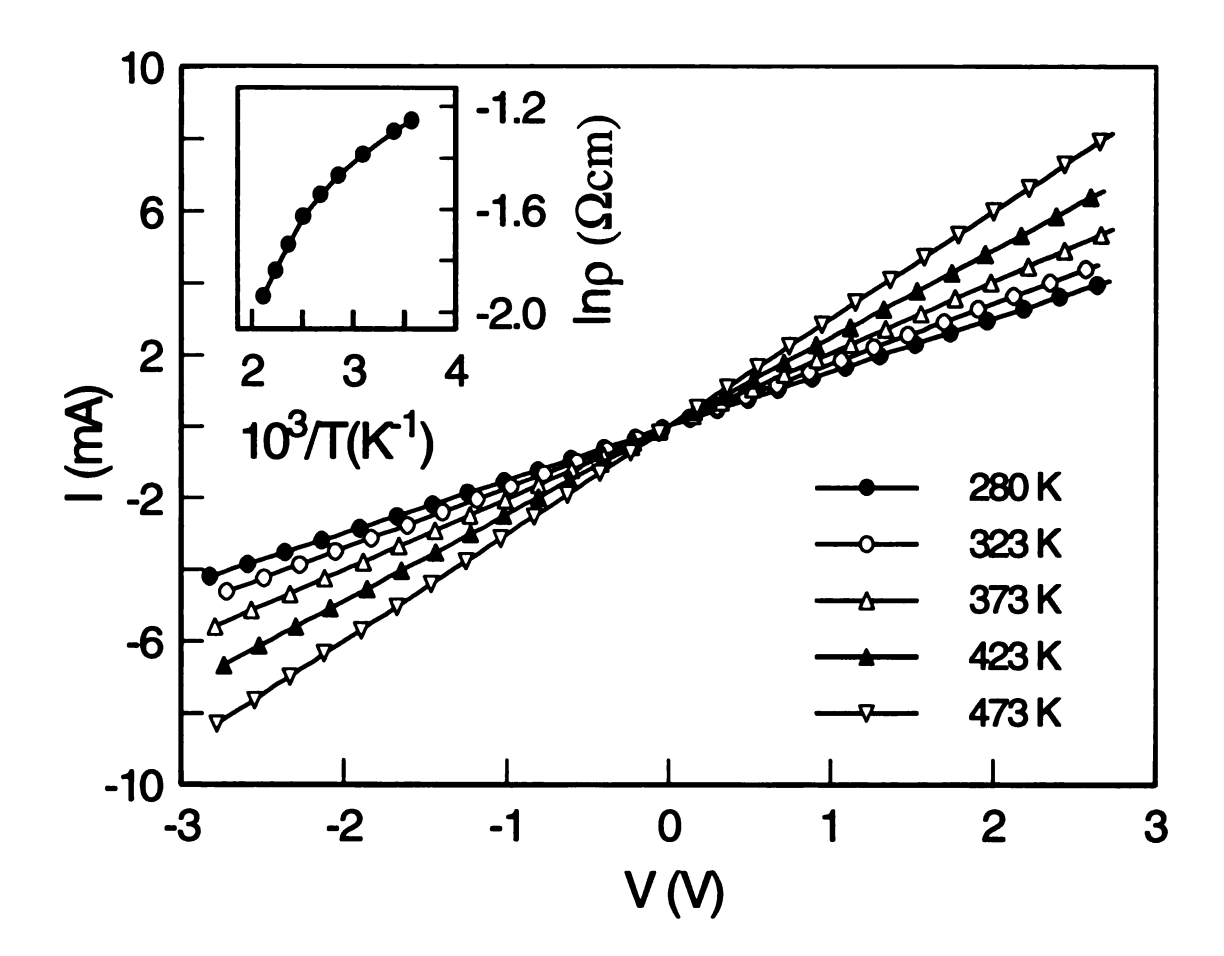


Figure 4.6 Four-probe resistivity measurements as a function of temperature.

polycrystalline diamond is studied by three types of measurements: (i) four-point-probe measurements of effective resistivity in the temperature range of 7-200°C, (ii) potential profile measurements across a few grains and (iii) two-point-probe I-V measurements within a single grain and across an individual GB. The I-V data and surface morphology of the conduction path are directly correlated for the first time.

## 4.5.1 Experimental

The large grain film described in section 3.3.2 is used in this experiment. A microprobe station equipped with a heated chuck is used for I-V measurements under atmospheric pressure in a Nitrogen rich environment. The temperature and voltage are limited by the cooling/heating capacity of the chuck and the compliance current of the HP4145, respectively. Tungsten probes with tip diameter of 5 µm are used for electrical contacts.

### 4.5.2 Four-point probe measurements

The four-point-probe measurements, with a probe separation equal to 20 times the mean grain size, reveal a linear I-V relationship in the temperature range of 7-200°C, as shown in Figure 4.6. The inset shows that the slope of lnp vs 1/T is not constant which indicates a spread of activation energies. In order to understand this non-Arrhenius resistivity behavior, current flow in the film is characterized by performing potential profile measurements.

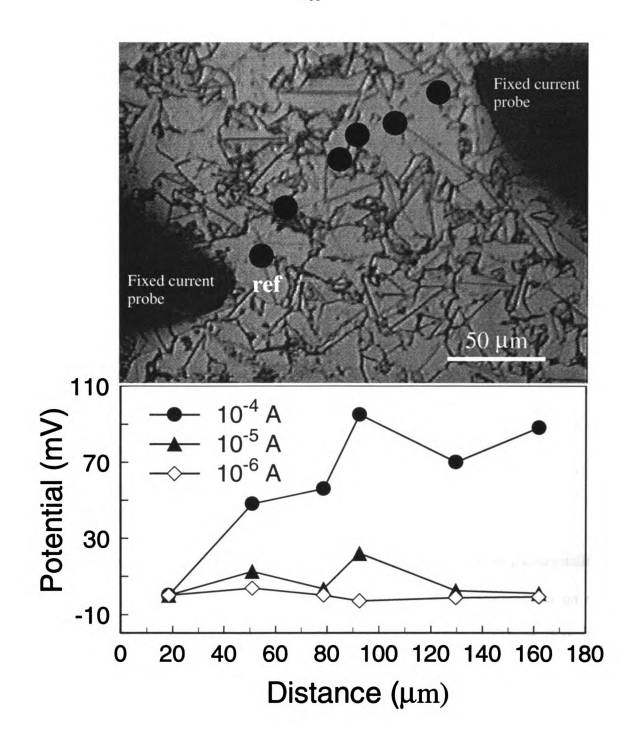


Figure 4.7 Potential profile measurements and corresponding probe positions.

## 4.5.3 Potential profile measurements

Two fixed probes are used to apply constant current, as depicted in the light microscope photo in Figure 4.7. Using the probe in the left as a reference, the potential at the positions marked by black dots is measured. Since the obtained potential values are affected by the reference contact potential, the potential difference between the dots with respect to the leftmost dot is computed. The potential differences thus obtained are plotted for three different current levels in Figure 4.7. For  $10^{-6}$  A and  $10^{-5}$ A, the potential does not seem to increase with distance. This may reveal that the shortest path is not necessarily the lowest resistance path and that current flow is probably not uniform. However, for  $10^{-4}$ A, the shortest path seems to be the lowest resistance path.

## 4.5.4 Intra- and inter-grain I-V

#### Non-ohmic contacts

While the above measurements suggest non-uniform current flow in polycrystalline diamond and its sensitivity to current/field bias, they provide no information on the effect of grains and GBs. To study the role of grains and GBs in current flow, the distance between the fixed probes was reduced to 20 µm and the probes were placed so that the shortest path between them is either entirely within a single grain or crosses an individual GB. Typical curves obtained from intra- and inter-grain I-V data measured at different regions of the sample, are plotted in Figure 4.8a. A nearly symmetrical but non-linear I-V relationship is observed. Since all the probes are placed on smooth grain facets, the W-diamond contacts are expected to be non-ohmic [117]. Nevertheless, the

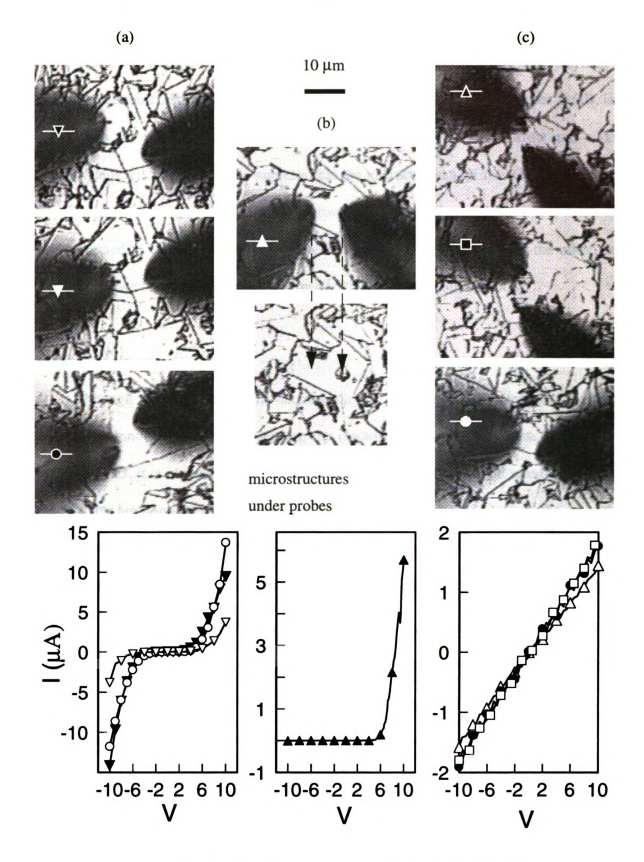


Figure 4.8 I-V data and corresponding probe positions.

contact potentials for all curves are expected to be comparable. Based on this observation, the apparent increase in barrier potential observed for the wide-GB-intergrain connection could be due to the existence of an additional potential barrier at GB, in series with the contact potential. Comparing the I-V curves for the narrow and wide barriers depicted in Figure 4.8a, suggests that the characteristics of this GB barrier may be affected by the width of the GB. The variation in GB angles shown in Figure 3.15b is also expected to result in variations of the barrier height from one GB to the other, as was established for other polycrystalline materials such as polysilicon [108].

#### Ohmic contacts

Although the existence of GB barriers may be deduced from non-ohmic I-V data, such data cannot be used to characterize the electrical properties of grains. During our measurements, it is observed that when two probes are placed on rough micro-structures the contacts are ohmic. Figure 4.8b shows an I-V curve obtained with one probe on such micro-structures and the other on a smooth grain facet. The observation of ohmic contacts to the rough micro-structures is consistent with reports that damage to the diamond surface [117] and higher incidence of GB [118]·[119] improve metal contacts to diamond. I-V data obtained with both probes on rough micro-structures in different locations of the sample are shown in Figure 4.8c. Comparable linear I-V is observed regardless whether both probes are within a grain, both probes are on GBs or one probe is on GB and the other within a grain. Since ohmic contact is limited by the availability of rough microstructures it was not possible to obtain I-V data such that the probes are across opposite sides of the same GB. As a result, the I-V data shown in Figure 4.8c

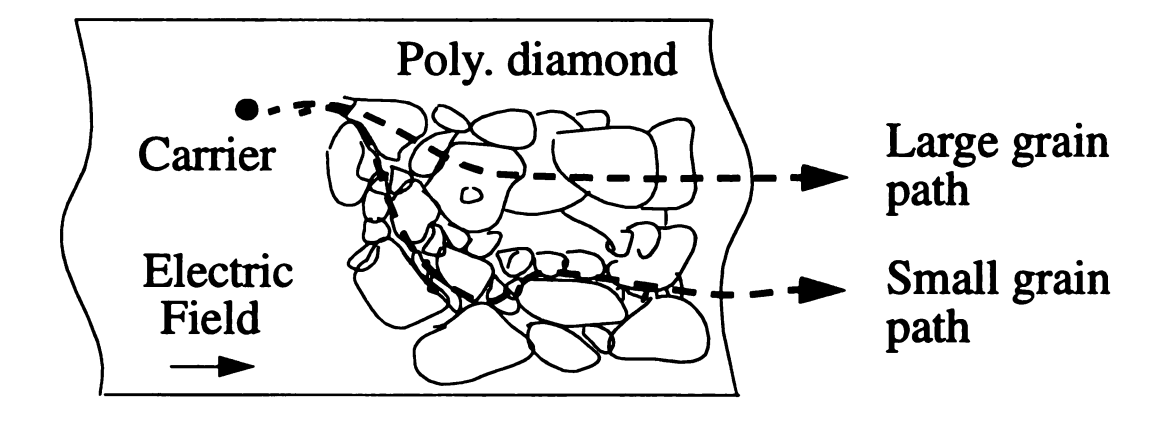


Figure 4.9 Current flow in polycrystalline diamond with non-uniform grain size modeled in terms of paths made of small grains and paths made of large grains.

probably reflect intra-grain conduction.

#### 4.5.5 Non-uniform current flow

Table 4.2 shows a summary of the linear I-V data obtained from the four-point probe, the potential profile and the two-point probe measurements. Interestingly,  $\frac{\Delta V}{I}$  decreases with increasing probe separation. As there is a wide spread of grains sizes, it may be assumed that current paths with small and large grains have conductivities  $\sigma_{sg}$  and  $\sigma_{lg}$ , respectively, as indicated in Figure 4.9. The average conductivity in the film,  $\sigma_{avg}$ , is written in terms of contribution of all paths:

$$\sigma_{avg} = \Sigma \sigma_{sg} + \Sigma \sigma_{lg}$$

Other studies have shown that for the same doping conditions the measured resistivity of large grain films is higher than that of small grain films [81]. Consequently, the resistivity for small-grain paths is expected to be lower than that of large grain paths. As the probe separation increases the probability of occurrence of small grain paths increases. Thus the resistivity of the dominant path(s) decreases leading to lower resistance for longer path(s). It is not clear at this point if the resistivity variation with grain size is due to variation in doping incorporation with grain orientation and GB angle [120] or GB vs. grain contribution to conduction.

Depending on the conduction mechanism, current flow could be affected by the observed variation of GB potential barrier heights and widths as in the case of polysilicon [108]. Non-uniform current flow results in non-uniform potential profiles and could give the impression of a spread of activation energies [121] if different conduction

mechanisms exist for different doping levels. Interestingly, non-uniform current flow could be one of the reasons why electrical properties of CVD diamond do not show good quantitative fit to simple models that use average parameters and assume spatial uniformity, such as the boundary barrier model [120].

Figure 4.7 shows that the potential drop along the characterized path increases linearly with distance for 10<sup>-4</sup>A, but not for 10<sup>-6</sup>A and 10<sup>-5</sup>A. Since as the applied current increases, the potential drop and hence electric field increases, the observed difference in potential profiles maybe related to the effect of electric field on resistivity presented in 4.4. In this context, the data in Figure 4.7 can be interpreted as follows: as the applied electric field increases, the resistance of the shortest path decreases until it becomes the least resistance path. This suggests that as electric field increases current flow becomes more uniform.

Table 4.2 Summary of linear I-V data

Measurement	Shortest path	I (A)	$\frac{\Delta V}{I}$
Four point probes	1587 μm	10-3	0.7 ΚΩ
Potential profile	190 μm: 3 large grains	10 <sup>-4</sup>	10 ΚΩ
2 probes on rough diamond	6-14 μm: within a single grain	10 <sup>-6</sup>	6.7-5.5 ΜΩ

#### 4.6 Summary

In this chapter, the effect of substrate, post deposition anneal and electric field on the resistivity of B-doped polycrystalline CVD diamond deposited on insulating substrate, were studied. The anneal study reveals for the first time that the resistivity decrease with anneal is lower at high doping and varies with diamond quality. The electric field study shows for the first time that resistivity decreases with increasing electric field for fields up to 10<sup>3</sup>V/cm. This field effect seems to be related to the presence of GBs and is found to be less pronounced at high doping, high temperature and for highly oriented films. Four-point probe I-V across many grains, potential profile across five grains and two-point-probe I-V within a single grain and across an individual GB reveal non-uniform current flow in B-doped polycrystalline diamond. Inter-grain I-V across individual GBs with different widths suggests the existence of potential barriers at GBs.

# **CHAPTER 5**

# Sensor characterization

#### 5.1 Introduction

The purpose of sensor characterization is to understand and eventually improve the performance of CVD diamond piezoresistive sensors. Early work on CVD diamond piezoresistors suggests that performance may be affected by operating conditions and film properties. As piezoresistance characterization is based on resistance measurements and the resistance of CVD diamond is affected by electric field, it is important to determine if the electric field affects piezoresistivity. Since the greatest potential for diamond pressure sensors would be at high temperature where the performance of their Si counterparts deteriorates, it is important to characterize them at high temperature.

In this chapter, the effects of electric field and temperature on GF of B-doped CVD diamond are measured as a function of doping level. The results, when correlated with data published in the literature, show that both field and temperature effects seem to be less prominent with increased doping.

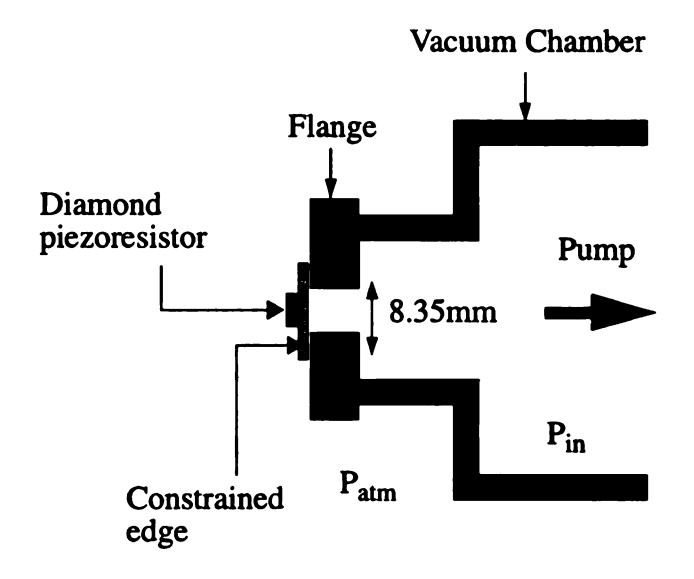
#### 5.2 Gauge factor measurement setup

Early GF measurements used a cantilever beam and three point bending structure [7][9]. In this work, a cantilever beam and a membrane based setup are used. The strain equations for the cantilever beam setup developed in [36] will be summarized. As strain calculation for the membrane based setup is highly dependent on the assumptions made to convert pressure to strain, it is important to fully describe it.

#### **5.2.1 Pressure sensor setup**

A schematic of a membrane based setup consistent with commercially available differential pressure sensors is depicted in Figure 5.1. A hole with 8.35 mm diameter is drilled in the center of a standard 2-3/4" stainless steel blank flange. The sample is rigidly glued on the flange, with the diamond piezoresistor radially aligned at the center of the hole facing outward in order to facilitate making electric connections. The flange is then used to seal one of the ports of a vacuum chamber. The chamber is pumped down thus subjecting the sample to a differential pressure equal to the difference between atmospheric pressure and the pressure inside the chamber.

As the sensitivity of piezoresistors is generally characterized in terms of gauge factor,  $GF = \frac{\Delta R}{R_0} \cdot \frac{1}{\epsilon}$ , where  $R_0$  and  $\epsilon$  are the stress-free resistance and the applied strain, pressure values must be transformed to strain values. Plate theory for uniform pressure load is used for this purpose. The appropriate plate model and boundary conditions for this setup are checked using a commercially available wire strain gauge. The gauge is mounted on an oxidized Si substrate similar to those used in the actual samples. The pressure response of



Differential pressure  $P = P_{atm} - P_{in}$ 

(a)

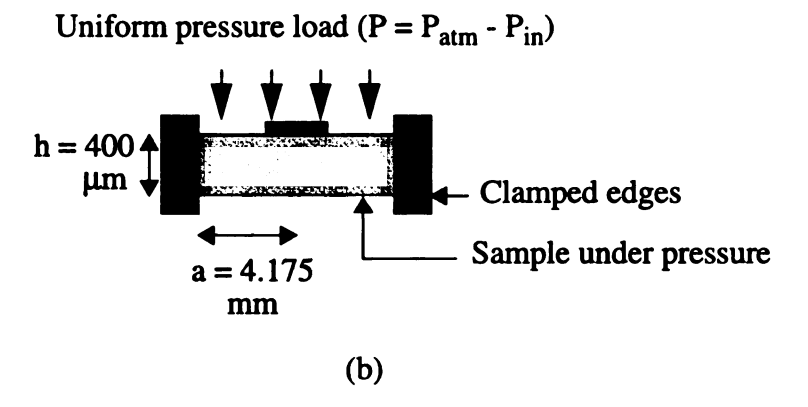


Figure 5.1 (a) Differential pressure measurement setup and (b) plate model.

the wire strain gauge is plotted in Figure 5.2. Pressure is transformed to strain using the circular plate model for small deflection, clamped edges and uniform load [122]:

$$\varepsilon_l = \frac{3P(1-v^2)(r_0^2 - 3r^2)}{8Eh^2} \text{ and } \varepsilon_t = \frac{3P(1-v^2)(r_0^2 - r^2)}{8Eh^2},$$
 (5.1)

where  $\varepsilon_l$  and  $\varepsilon_t$  are the radial and circumferential strains, E and v are Young's modulus and Poisson ratio for Si, P is the differential pressure, h is the Si thickness and  $r_0$  is the radius of the area under pressure. The longitudinal gauge factor obtained using the computed strain values is 2.667 which is close to the manufacturer specified value of 2.105 $\pm$ 0.5%. The discrepancy maybe due to the large dimension of the strain gauge as compared to the hole diameter. Based on this strain gauge test, the small deflection, uniform load and clamped edge model seems appropriate for this measurement setup.

Since the diamond films show good physical adhesion to the oxidized Si substrate when subjected to scratch testing, it is reasonable to assume that strain is transmitted ideally across the diamond-substrate interface. The presence of the 3µm diamond layer changes the strain on the 400 µm uncoated oxidized silicon substrate by a correction factor computed using the theory of bi-fringed coatings [123]:

$$FCR = 1 + \frac{h_d}{h_{Si}} \cdot \frac{E_d}{E_{Si}} \cdot \frac{1 + v_{Si}}{1 + v_d} = 0.9761,$$
 (5.2)

where E and v and h are Young's modulus, Poisson ratio and thickness of silicon (Si subscript) and Diamond (d subscript), respectively.

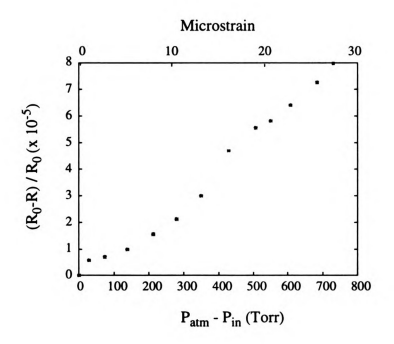


Figure 5.2 Pressure response of wire strain gauge.

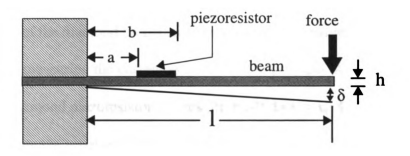


Figure 5.3 Schematic diagram of a cantilever beam setup.

#### 5.2.2 Cantilever beam setup

A schematic of a cantilever beam setup is shown in Figure 5.3. Assuming that at the fixed end the beam can neither rotate nor translate and neglecting shear deformation, the strain due to a small deflection as a result of a concentrated bending force F, can be written as [36]:

$$\varepsilon = \frac{3h}{2l^3} \left( l - \frac{1}{2} (a+b) \right) \cdot \delta \tag{5.3}$$

where h, l, a, b and  $\delta$  are as indicated in Figure 5.3. Two of the advantages of the cantilever beam technique are its ease and the possibility to apply both compressive and tensile strains.

## 5.3 Effect of electric field on piezoresistance

The effect of electric field on piezoresistivity is studied by measuring the pressure response of diamond piezoresistors of the small grain type with resistivities of 0.29, 10 and 116  $\Omega$ cm, in the pressure and field ranges of 10 - 740 Torr and 10 - 250 V/cm, respectively.

The resistance of the diamond piezoresistor is measured by maintaining a constant DC voltage bias and measuring the current as a function of pressure. Assuming uniform current flow in the diamond piezoresistor, the resulting I-V data is used along with sample dimensions to compute the resistance change and the electric field. The measured change of resistance with pressure,  $\frac{\Delta R}{R_0}$ , for the 0.29, 10 and 116  $\Omega$ cm samples are plotted in Figures 5.4 - 5.6, respectively. The insets show representative (i) SEM and (ii) Raman. Based on SEM the average grain size is approximately equal to 2  $\mu$ m for all samples. The

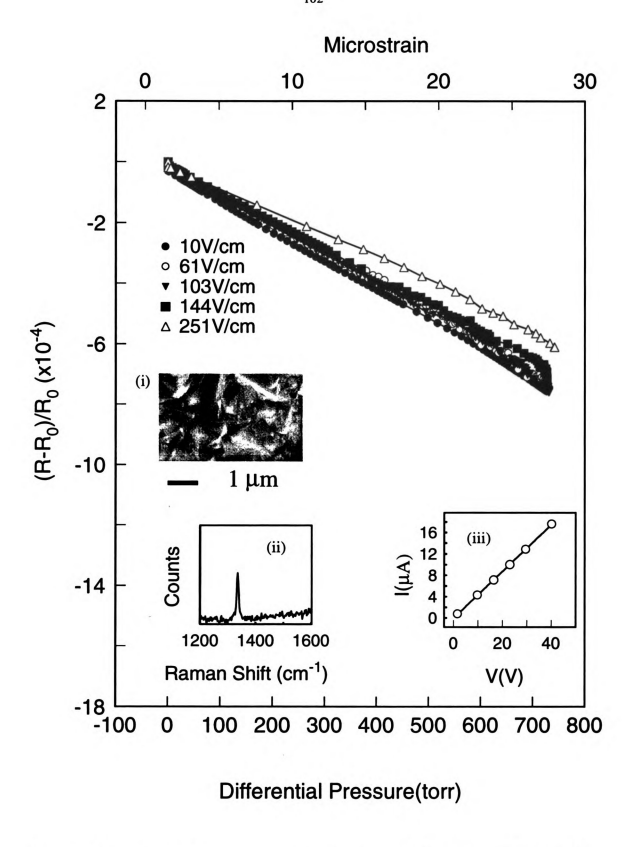


Figure 5.4 Room temperature pressure response measured using different electric fields. Insets: (i) SEM, (ii) Raman and (iii) zero strain IV.

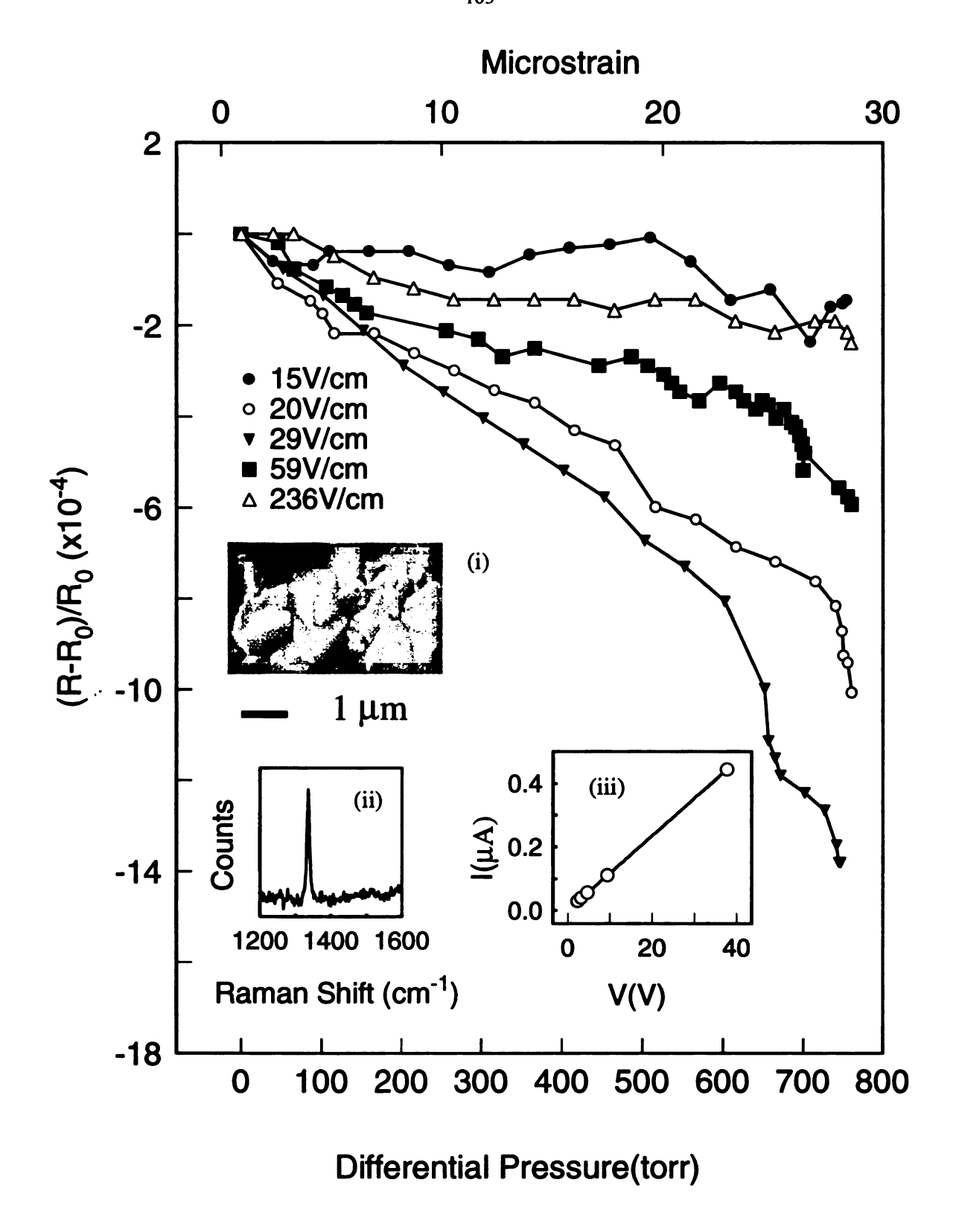


Figure 5.5 Room temperature pressure response measured using different electric fields. Insets: (i) SEM, (ii) Raman and (iii) zero strain IV.

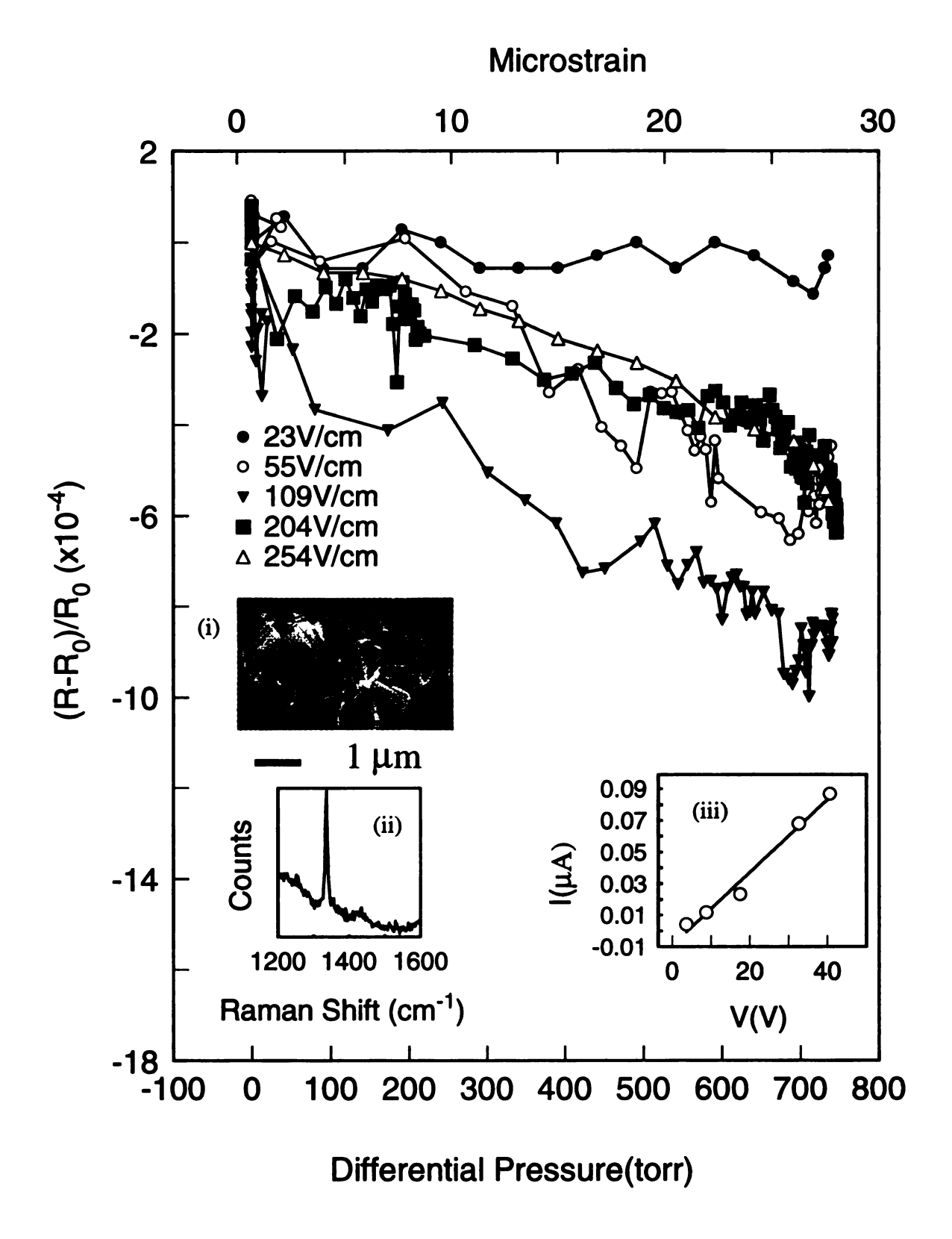


Figure 5.6 Room temperature pressure response measured using different electric fields. Insets: (i) SEM, (ii) Raman and (iii) zero strain IV.

lowest resistivity sample shows twinned grains. The Raman spectra show low graphitic content for all samples although the intensity of the diamond peak varies among samples.

The pressure response of the lowest resistivity sample is nearly linear and changes little with electric field bias. For the high resistivity samples, linearity deteriorates and the sensitivity of the piezoresistor changes with applied electric field. Large fluctuations are observed especially for the 116  $\Omega$ cm sample. Inset (iii) of Figures 5.4 - 5.6 show linear IV.

In order to minimize the effect of the fluctuations on GF calculation, the data is first smoothed using a least square approximation and then used to compute GF. Figures 5.7 - 5.9 show the calculated GF for the three samples. Higher GF at lower strains is observed for the low resistivity sample. The zero strain resistivity,  $\rho_0$ , and GF at 20 microstrains, GF(20µ $\epsilon$ ), are plotted as a function of applied field in the insets. Although GF of all samples seems to depend on electric field, the field effect differs from one sample to the other. GF of the lowest resistivity sample decreases with increasing electric field. As shown in the inset of Figure 5.7, in the field range of 10 - 251 V/cm, GF(20µ $\epsilon$ ) and  $\rho_0$  decrease by 25% and 1.03%, respectively. The 10 and 116  $\Omega$ cm samples exhibit a different trend of GF dependence with electric field: first an increase with field then a decrease. Their GF(20µ $\epsilon$ ) reaches maximum values of 37 and 35 at 29 V/cm and 109 V/cm, respectively. Their  $\rho_0$  decreases by 1.41% and 49.5% in the field ranges of 15-236V/cm and 23-255V/cm, respectively.

A further consideration is the effect of electric field on linearity and offset.

Although it is not possible to measure these parameters accurately using this simple membrane setup, the data in Figure 5.4 - 5.6 show that the highly doped sample has better linearity and offset. Unfortunately, as in the case of silicon [124] and polysilicon [51],

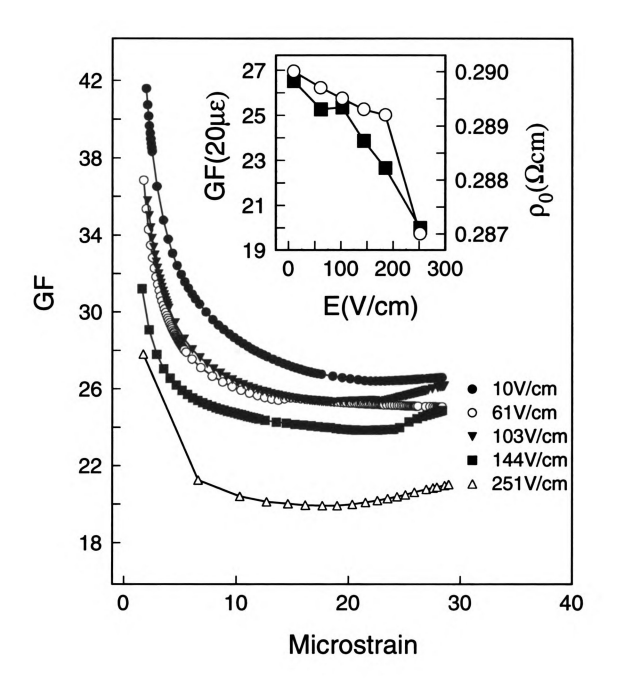


Figure 5.7 Calculated GF as a function of strain for SS4S6. Inset: (■) GF at 20 microstrains and (○)zero strain resistivity.

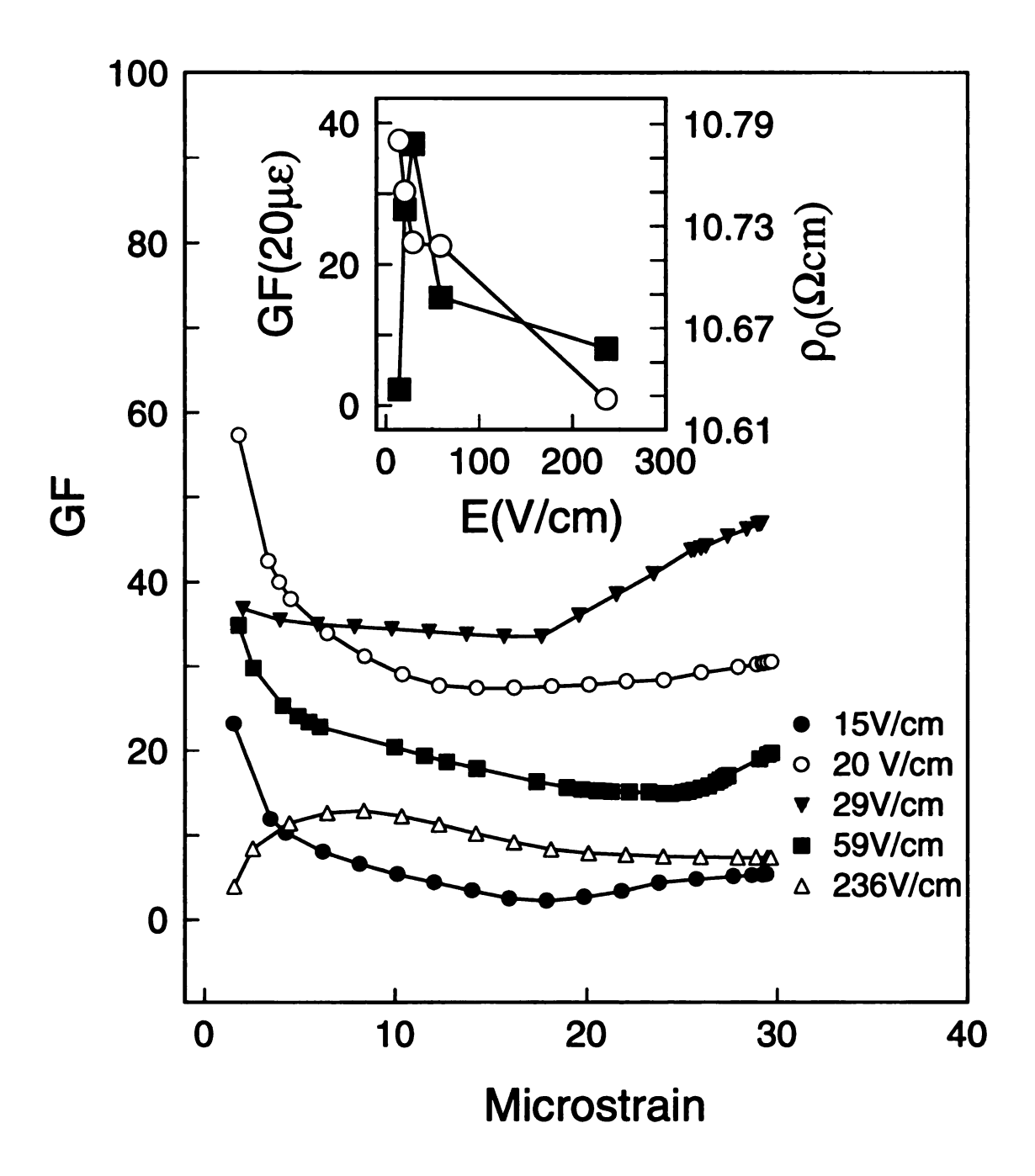


Figure 5.8 Calculated GF as a function of strain for SS70S2. Inset: (**a**) GF at 20 microstrains and (O)zero strain resistivity.

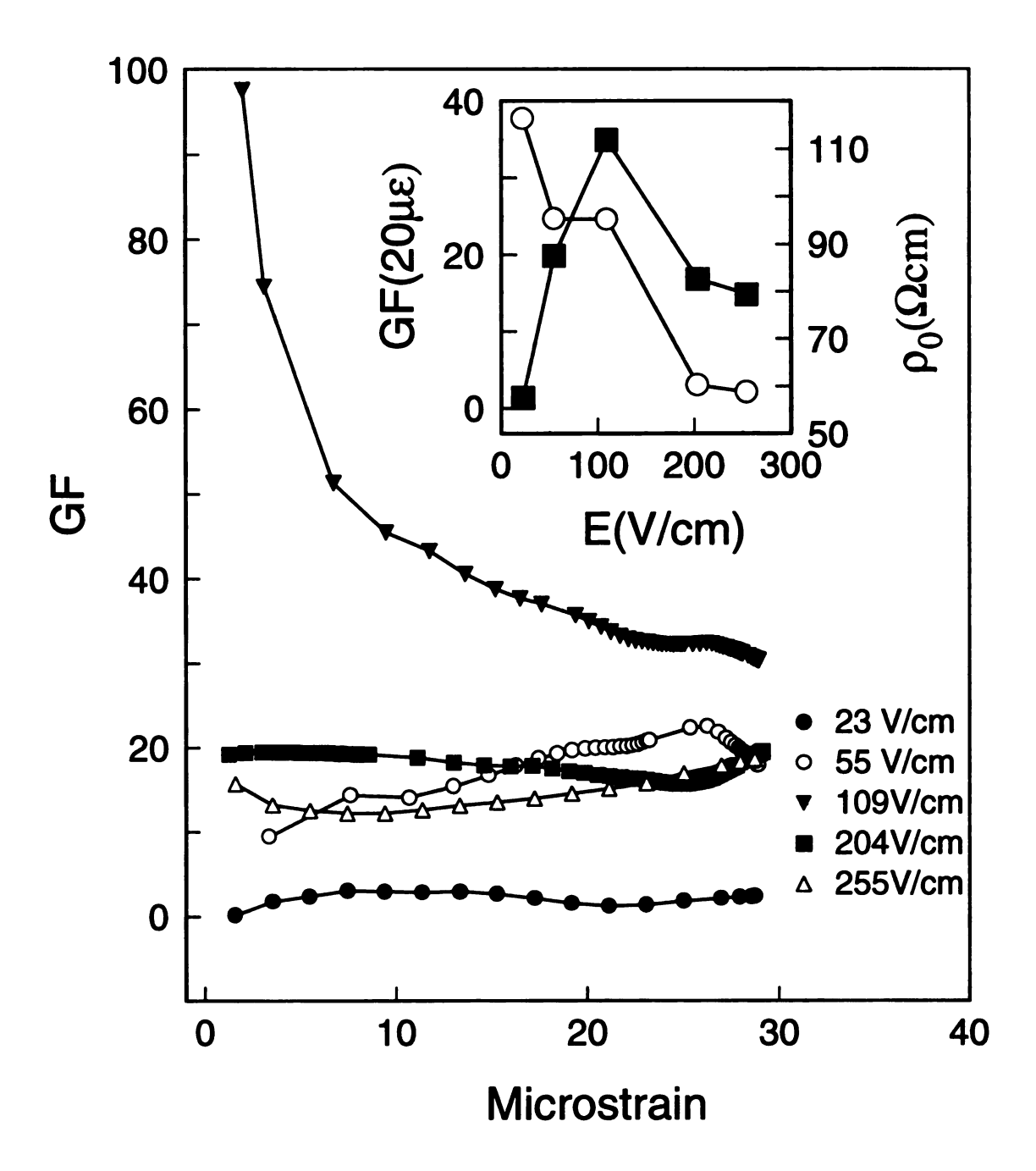


Figure 5.9 Calculated GF as a function of strain for SS70S4. Inset: (**III**) GF at 20 microstrains and (O)zero strain resistivity.

high doping decreases GF.

#### • Exploring the field effect on GF

The effect of electric field on GF is expected given the observed electric field effect on resistivity (section 4.4) and current flow (section 4.5). The effect of electric field on  $\rho_0$  is consistent with the finding that the resistivity decrease with electric field of films with comparable grain size is more prominent at lower doping level [125]. The mechanism for the observed change of GF with electric field is not clear and may be related to changes in current paths with electric field [126] if different paths have different GFs.

Since the field effect on GF of polycrystalline diamond is reported for the first time, it is interesting to explore its possible relationship to the scattering in the GF data reported in the literature [7][9][10][11][17][18]. As shown in Figure 5.10, there is a general trend of increasing GF with resistivity. However, some samples have comparable resistivity but different GFs. In addition to differences in film characteristics, this GF scattering, even from the same group of researchers [9][17][18], may be an indication that different field biases were applied to measure the resistance and/or piezoresistance.

## 5.4 Effect of temperature on piezoresistance

The effect of temperature on GF is characterized in the temperature range of 22-80 °C for small grain type samples with different doping levels using a cantilever beam setup. Heating is achieved by mounting a heater to the cantilever clamp and allowing the temperature of the sample to stabilize. A K-type thermocouple is used to measure the tempera-

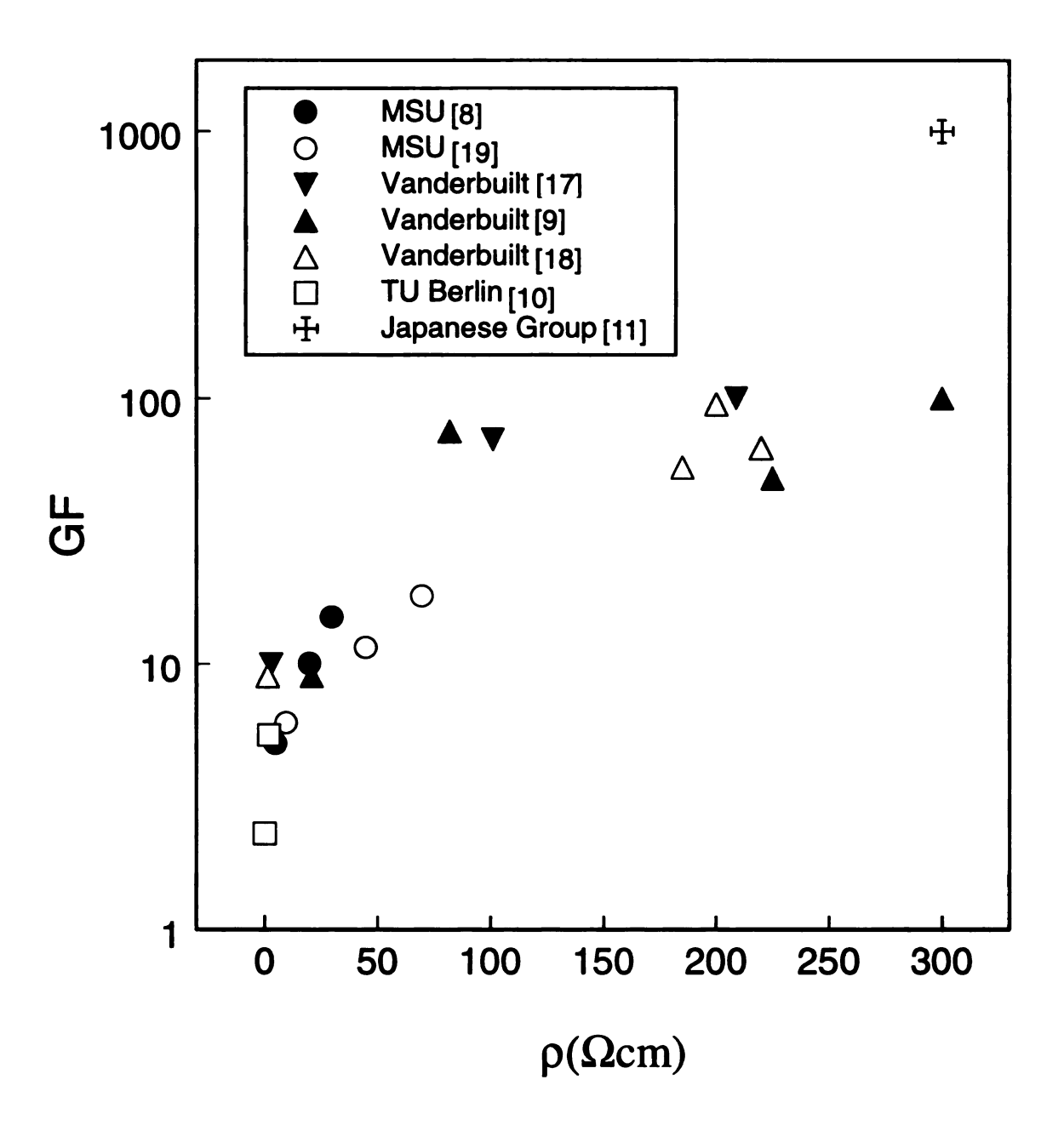


Figure 5.10 Summary of room temperature GF vs. resistivity data reported in literature.

ture.

The data shown in Figure 5.11, generated in collaboration with Xinhai Hou [127], shows that the effect of temperature on GF varies with doping level. The 5 and 3  $\Omega$ cm samples show a rapid increase of GF with temperature up to approximately 55 °C. At higher temperatures, GF of the 3  $\Omega$ cm sample starts to decrease. The gauge factor of the 0.7  $\Omega$ cm sample also increases with temperature; but at a much slower rate. In contrast, the gauge factor of the 0.07  $\Omega$ cm sample slowly decreases with temperature.

To further explore these results, they are compared with the data plotted in Figure 5.12 obtained from literature. Although samples from different research groups may have different characteristics that can affect GF sensitivity to temperature, a general trend can be distinguished when considering the temperature effect on piezoresistivity in relation to resistivity. Consistently with the results of this work, GF seems to change from being constant with temperature at low resistivity, to increasing at intermediate resistivity and decreasing at high resistivity. The decrease of GF with temperature has been observed for other semiconductor materials such as Silicon and polysilicon and attributed to intervalley lattice scattering [41]. The increase of GF with temperature, which is currently not well understood, has not been observed for any other semiconductor.

## 5.5 Summary

Our results show that GF of B-doped polycrystalline diamond is affected by the operating temperature and the electric field applied to measure the piezoresistance and that the field effect depends on doping level. Although the exact mechanism(s) involved in the field and temperature effects are not understood, the results show that higher

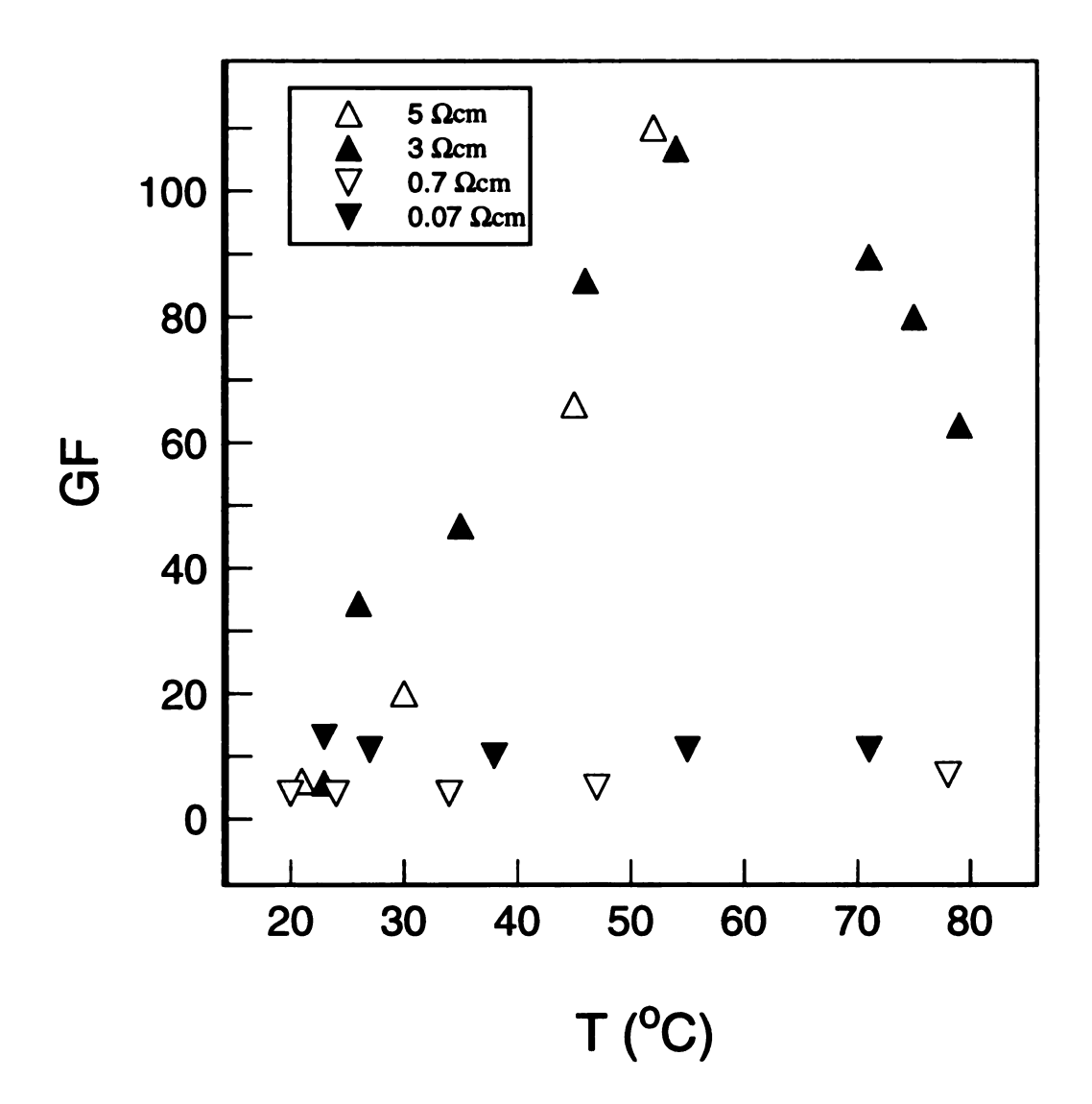


Figure 5.11 Effect of temperature on GF.

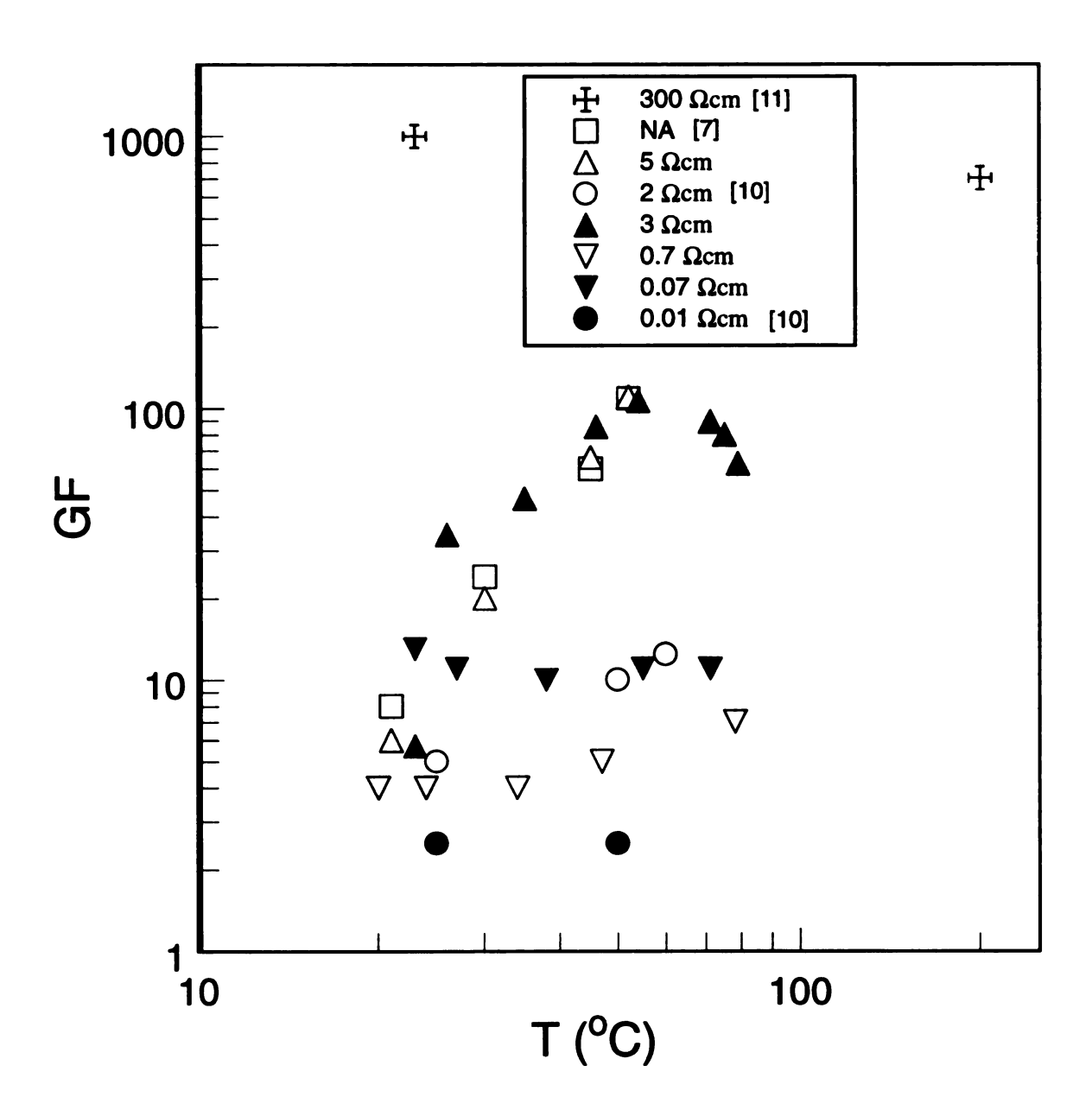


Figure 5.12 Summary of data reported in literature on the effect of temperature on GF.

doping lowers the dependence of GF on both field and temperature. Moreover higher doping improves linearity. Unfortunately, higher doping also decreases GF. Intra- and inter-grain GF measurements may help in understanding the field and temperature effects on GF.

# **CHAPTER 6**

# **Intra-grain Gauge Factor**

#### 6.1 Introduction

The reported piezoresistive gauge factors of single crystal and poly-crystalline diamond are in the ranges of 500 - 3,500 [8] and 10 - 1000 [9][10][11], respectively. As the chemical vapor deposited (CVD) diamond is inexpensive, polycrystalline CVD diamond piezoresistive sensors can become commercially viable if their sensitivity can rival that of a sensor made from crystalline diamond. Low GF values of CVD diamond can be attributed to the presence of grain-boundaries (GBs). In this chapter the effect of GB on GF of B-doped polycrystalline diamond is studied by measuring intra- and intergrain resistance as a function of strain. The extracted gauge factor values show that: (i) intra-grain gauge factor is comparable to single crystal diamond and (ii) the presence of grain-boundaries decreases the gauge factor and deteriorates linearity.

## **6.2 Measurement setup**

Four point probe resistivity measurements as a function of strain are performed on the large grain film described in section 3.3.2 with an average film resistivity of 0.28  $\Omega$ cm. The sample is mounted on a beam of oxidized silicon using Omega's C-C cement epoxy.

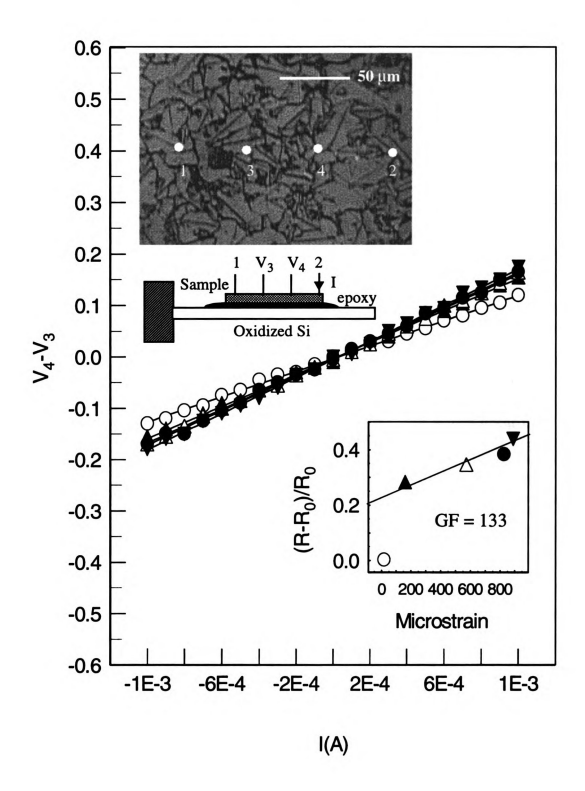


Figure 6.1 Small grain I-V at different strains and corresponding probe location. Insets: cantilever beam setup, relative resistance change vs. strain and extracted GF.

Strain is applied using a cantilever beam configuration, as shown in the inset of Figure 6.1. The cantilever beam setup is placed on top of the chuck of a microprobe station. Four tungsten probes connected to an HP4145B semiconductor parameter analyzer are used to measure I-V as a function of stress. The outer probes are used to apply current and the inner ones to measure voltage, eliminating the effect of contact resistance. A video camera and VCR are used to record the microscopic photo of the actual probe location.

The probes are placed so that the shortest current path is in the direction of longitudinal strain. The longitudinal GF is defined by:

$$GF_l = \frac{R - R_0}{R_0} \cdot \frac{1}{\varepsilon_l}$$

where  $R_0$  and R are the resistances at stain values of zero and  $\varepsilon_l$ , respectively. The resistance at a given strain is determined as the slope of the least square linear fit to the measured I-V data at that strain. The average longitudinal strain is measured by mounting a commercially available wire strain gauge on top of the diamond film. GF is determined as the slope of the least square linear fit to the  $\frac{\Delta R}{R_0}$  vs. strain curve.

## 6.3 Gauge factor for different current path morphologies

I-V data measured at different regions of the sample are plotted in Figures 6.1 - 6.3. The probe location is indicated by the white dots on the microscope photos shown in the inset. The extracted  $\frac{\Delta R}{R_0}$  vs. strain curve and resulting GF are also shown at the inset. Figure 6.1 shows the piezoresistive response when the shortest path between the voltage probes

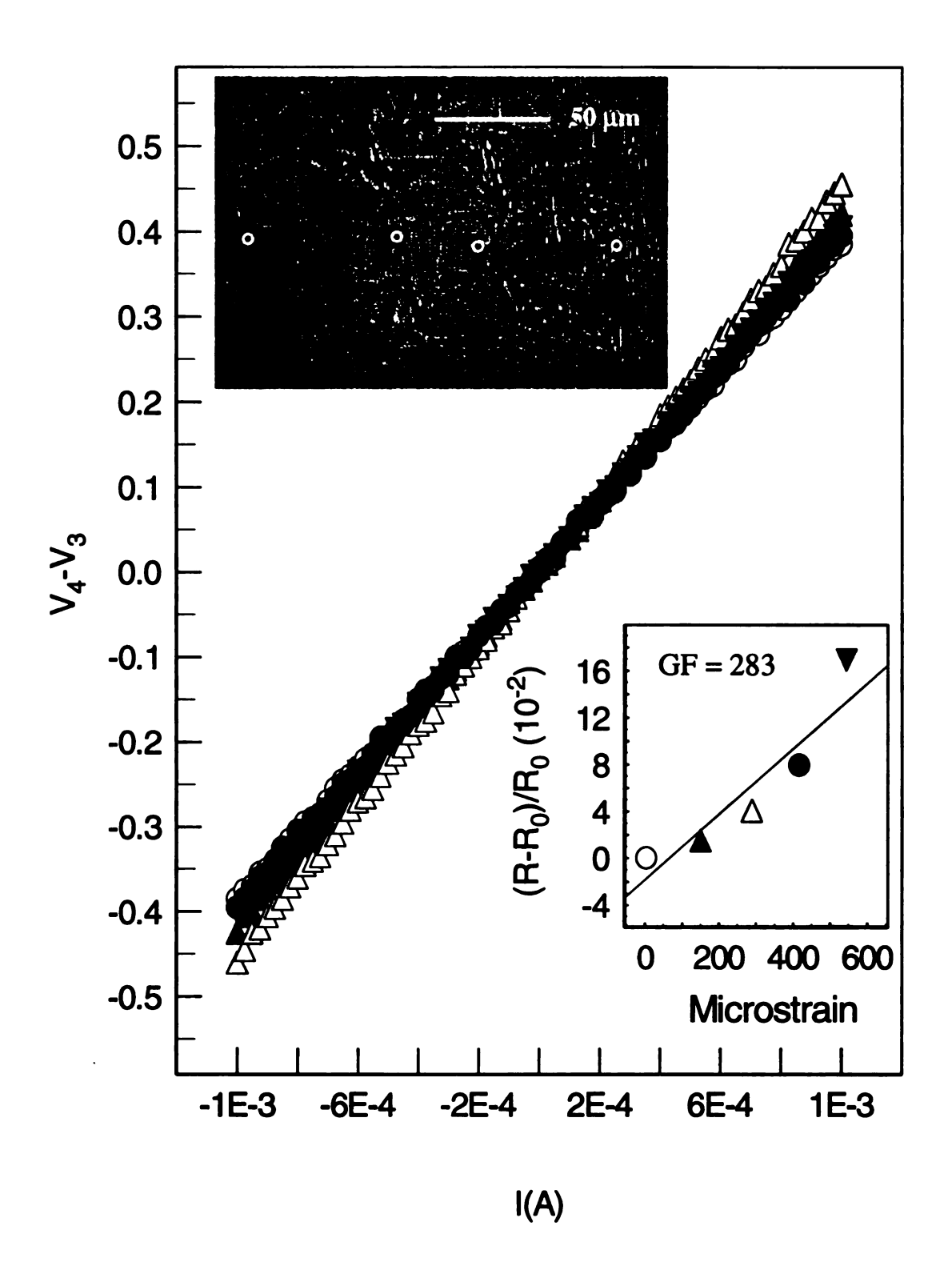


Figure 6.2 Large grain I-V at different strains and corresponding probe location. Inset: Relative resistance change vs. strain and extracted GF.

crosses many small grains. The resulting  $\frac{\Delta R}{R_0}$  vs. strain curve is nonlinear and a best line fit gives a GF of 133. The data shown in Figure 6.2 is obtained when the voltage probes are placed within a large grain and separated by a single GB. GF value of 283 is obtained. To investigate the effect of GB on GF, the probes are connected such that their shortest path does not cross any GB, as shown in Figure 6.3 The strain curve is linear and the extracted GF is 4062.

Assuming that the dominant current path is the shortest path between the current probes for all strains, the I-V data in Figure 6.3, where the voltage probes are placed within a single grain, describe intra-grain current flow. Consequently, the relatively high GF of 4687 corresponds to GF inside a grain. This is consistent with the high GF range of 500-3500 reported for single crystal homoepitaxial and synthetic diamond [8]. Although it is not clear whether the boundary crossing the shortest path in Figure 6.2 is a GB or a twin-boundary, its presence seems to result in lower GF and poorer linearity. The GB effect on linearity is worse when the number of GBs that cross the shortest current path increases, as seen in Figure 6.1. The low strain measurements seem to be scattered, especially for Figures 6.1 and 6.2, probably due to inaccurate strain values.

The measurements in Figures 6.1 - 6.3 show that intra-grain piezoresistive response has higher sensitivity and linearity than inter-grain. Since the crystal structure of the grain does not change with deposition method and conditions, intra-grain GF is expected to be independent of deposition parameters. Thus intra-grain CVD diamond piezoresistors are expected to be more reproducible and reliable than inter-grain piezoresistors.

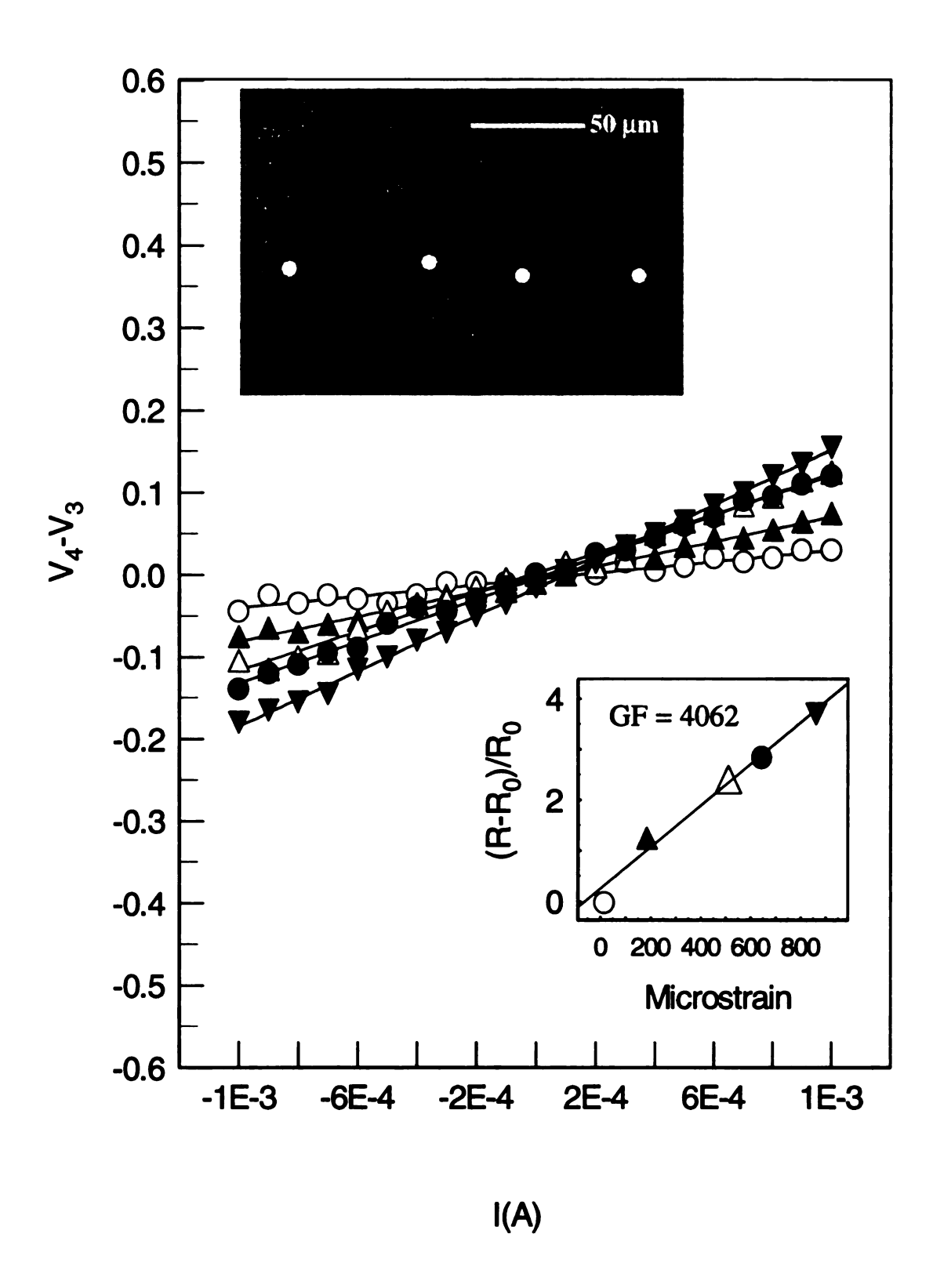


Figure 6.3 Intra-grain I-V at different strains and corresponding probe location. Inset: Relative resistance change vs. strain and extracted GF.

It is worth mentioning that the zero strain resistivities obtained from the four-point-probe measurements for the probe configurations in Figures 6.1-6.3 are 0.103, 0.272 and 0.034  $\Omega$ cm, respectively, and that the average film resistivity is 0.28  $\Omega$ cm.

It was found that the above GF results can lead to important information related to resistance of grain and grain-boundaries. Assuming that conduction in B-doped polycrystalline diamond is mainly through GBs, the resistance of the shortest path between the voltage probes can be witten as a series combination of contribution of grains,  $R_g$ , and GBs,  $R_b$ :

$$R = R_b + R_g \tag{6.1}$$

Using this formula the relative change of path resistance with strain can be written as:

$$\frac{R - R_0}{R_0} \approx \left(\frac{1}{1 + \alpha}\right) \frac{R_g - R_{g0}}{R_{g0}} + \left(\frac{\alpha}{1 + \alpha}\right) \frac{R_b - R_{b0}}{R_{b0}}$$
(6.2)

where  $\alpha = \frac{R_{b0}}{R_{g0}}$ . Similarly, starting from path length:

$$L = L_b + L_g, (6.3)$$

where  $L_g$  and  $L_b$  are the part of the path through grains and GBs, respectively, the relative change of path length is given by:

$$\varepsilon = \frac{L - L_0}{L_0} = \left(\frac{1}{1 + \beta}\right) \frac{L_g - L_{g0}}{L_{g0}} + \left(\frac{\beta}{1 + \beta}\right) \frac{L_b - L_{b0}}{L_{b0}}$$
(6.4)

where  $\beta = \frac{L_{b0}}{L_{g0}}$ . For uniform strain distribution, since  $L_g >>> L_b$  and  $\beta \approx 0$ , equation (6.3) becomes:

$$\varepsilon \approx \frac{L_g - L_{g0}}{L_{g0}} = \varepsilon_g, \tag{6.5}$$

where  $\varepsilon_g$  is the intra-grain strain. Based on equations (6.2)-(6.5):

$$GF \approx \frac{R - R_0}{R_0} \frac{1}{\varepsilon_g} = \left(\frac{1}{1 + \alpha}\right) GF_g + \left(\frac{\alpha}{1 + \alpha}\right) \delta GF_b,$$
 (6.6)

where 
$$\delta = \frac{\varepsilon_b}{\varepsilon_g}$$
.

As in polysilicon, the disordered structure of GB is expected to result in very low  $GF_b$  as compared to  $GF_g$  [51]. In this case, equation (6.6) gives:

$$GF \approx \left(\frac{1}{1+\alpha}\right)GF_g$$
 (6.7)

Plugging in  $GF_g = 4062$  and GF = 283, 133 yields:

$$\alpha = \frac{R_{b0}}{R_{g0}} \approx \frac{GF_g - GF}{GF} = 13,29$$
 (6.8)

for the data in Figure 6.2 and 6.1, respectively.

The above result provides evidence that GBs have higher resistance than grains and that GB contribution to path resistance increases as more GBs are crossed. The larger GB resistance as compared to grain resistance is consistent with the assumption that current flow in the film is dominated by carrier transport from one grain to the other through GBs (Equation 6.1). The high GB resistance could be due to GB potential barriers, as suspected from inter-grain I-V [126], and/or to Boron desegregation at GB, as reported in [128].

It is important to emphasize that the derived ratio of GB to grain resistance is subject to the assumption that strain distribution along the current path is uniform. As inhomogeneous internal strain distributions were reported for polycrystalline diamond

[63], direct measurement of the strain along the current path shown in Figure 6.1 - 6.3 is needed to fully confirm the results of Equation 6.8.

## **6.4 Summary**

In this chapter intra-grain GF is measured for the first time and its value, 4062, is comparable to that of single crystal diamond. Intra-grain piezoresistive response shows better linearity than inter-grain and is expected minimize scattering in reported GF data attributed to differences in film deposition and/or processing conditions.

Assuming that (i) strain distribution is uniform in CVD diamond, (ii) GF of GB is zero and (iii) current flow is dominated by paths that cross GBs, a simple model is used to determine the effect of GB on GF. Based on this model, the ratio of GB to grain resistance is computed and shown to increase with the number of GBs in the current path. The high GB resistance as compared to grain resistance provides for the first experimental evidence that the role of GBs in electrical conduction in B-doped polycrystalline diamond is to limit current flow.

# **CHAPTER 7**

# **Summary and Future Research**

#### 7.1 Introduction

The primary objective of this research is to characterize the piezoresistive gauge factor of B-doped CVD diamond. In order to achieve this goal, resistivity and sensor characterization are performed on films deposited on insulating substrates. Resistivity characterization covers the effect of substrate conduction, anneal and electric field on resistivity. It also included intra- and inter-grain I-V measurements. Sensor characterization addresses the effect of electric field and temperature on GF of B-doped CVD diamond. Intra- and inter-grain GF measurements are performed.

## 7.2 Summary of Contributions

## 7.2.1 Results reported for the first time

## • Intra- and inter-grain measurements

Four-point probe I-V across many grains, potential profile across five grains and two-point-probe I-V within a single grain and across an individual GB reveal non-uniform current flow in B-doped polycrystalline diamond. I-V measurements across individual

grain boundaries with different widths suggest the existence of grain boundary potential barriers.

Intra-grain piezoresistive response measurements show excellent linearity and a GF of 4687, which offers sensitivity in the same range as single crystal diamond at a much lower cost. Since intra-grain conduction is not affected by grain boundaries, intra-grain GF is expected to be less sensitive to electric field and film quality than inter-grain GF. A simple gauge factor model is derived as used along with intra-and inter-grain GB data to compute the ratio of grain-boundary to grain resistance. The higher GB resistance as compared to grain resistance provides experimental evidence that current follows intergrain paths as opposed to parallel grain-boundary paths.

## • Effect of electric field on resistivity and GF

The pressure response of B-doped chemical vapor deposited (CVD) polycrystalline diamond piezoresistors is characterized using an experimental setup consistent with commercially available differential pressure sensors. The change of resistance due to pressure is measured over a range of 10-740 Torr for samples with resistivities of 0.29, 10 and 116 Ωcm. The results show that pressure response is affected by the electric field applied to measure the resistivity. Higher doping minimizes this field dependence and seems to improves linearity at the cost of lower sensitivity.

The study of the electric field on resistivity reveals that resistivity decreases with increasing electric field and that the onset and rate of resistivity decrease varies with doping, temperature and grain size and orientation. The absence of field effect in B-doped homoepitaxial diamond suggests that the field effect is related to the presence of grain-

boundaries.

#### • Effect of anneal on resistivity

The anneal study reveals that the resistivity of B-doped polycrystalline diamond decreases after anneal at 600°C in N2 for 10 min. The anneal effect, is found to decrease with doping and to vary with film quality.

#### 7.2.2 Other significant results

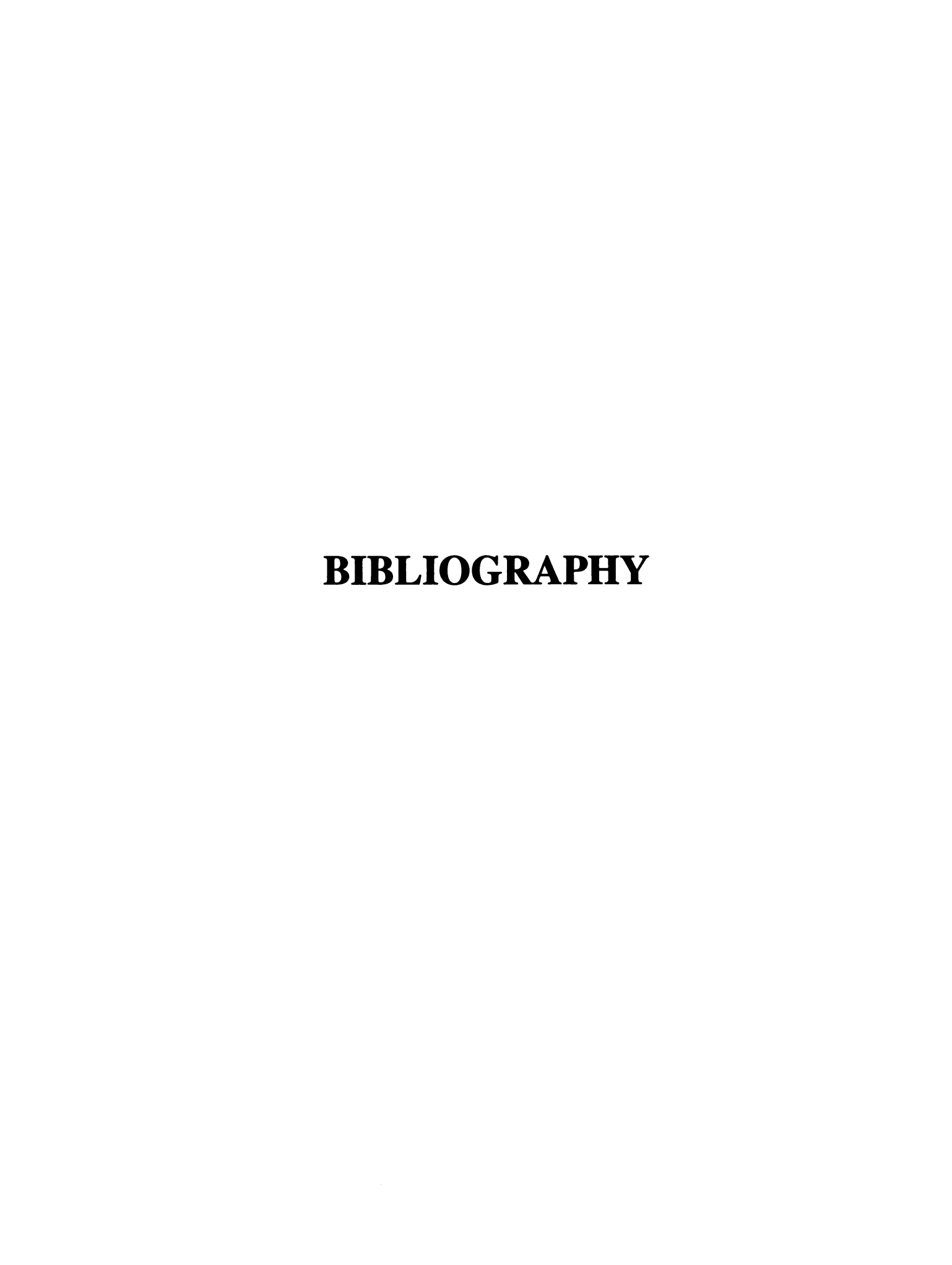
- A 4" wafer HFCVD system is built and a special temperature control scheme is implemented to use the heat generated by the 4.5 x 5 inch<sup>2</sup> filament array for substrate heating without degrading diamond quality.
- The finding that undoped films grown on conducting Si are conducting whereas those grown on oxidized Si are insulating restricted the samples used in this study to those grown on oxidized Si.
- Temperature measurements reveal that GF changes from being constant with temperature at low resistivity, to increasing with temperature at intermediate resistivity and decreasing at high resistivity.

#### 7.3 Future Research

Although this study improves current understanding of CVD diamond piezoresistance, more advances are need in the following areas in order to help commercialize diamond piezoresistors:

(i) determine the exact role of GBs in electrical and mechanical properties,

- (ii) improve consistency of diamond quality and enhance doping uniformity,
- (iii) fabricate a pressure sensor prototype and use it to measure a complete set of performance specifications for CVD diamond sensors,
- (iv) extend the temperature range for sensor characterization,
- (v) evaluate sensor reliability and repeatability, and
- (vi) evaluate sensor performance in industrial environments.



## **BIBLIOGRAPHY**

- [1] Interview of Dr. Bryzek, co-founder and executive vice president of Lucas NovaSensor, Fremont, California.
- [2] G.L. Pearson, W.T. Read, Jr. and W.L. Feldman, "Deformation and Fracture of Small Silicon Crystal's," Acta. Met., vol. 5, pp. 181-191, 1957.
- [3] S. Koizumi, M. Kamo, Y. Sato, H. Ozaki and T. Inuzuka, "Growth and Characterization of Phosphorous Doped {111} Homoepitaxial Diamond Thin Films," To be published in Appl. Phys. Let. no. 11 Aug. 1997 issue.
- [4] Diamond: Electronic Properties and Applications, Edited by L.S. Pan and D.R. Kania, Kluwer Academic Publishers.
- [5] D. M. Malta, J. A. von Windheim, H. A. Wynands and B. A. Fox, "Comparison of the Electric Properties of Simultaneously Deposited Homoepitaxial and Polycrystalline Diamond Films," J. App. Phys., vol. 77, no. 4, pp. 1536-1545, 1995.
- [6] Synthetic Diamond: Emerging CVD Science and Technology, Edited by H.E. Spear and J.P. Dismukes, Published by John Wiley and Sons, Inc., 1993.
- [7] M. Aslam, I. Taher, A Masood, M. A. Tamor and T. J. Potter, "Piezoresistivity in vapor-deposited diamond films," Appl. Phys. Lett., vol. 60, pp. 2923-2925, 1992.
- [8] I. Taher, M. Aslam, M. Tamor, T.J. Potter and R.C. Elder, "Piezoresistive Microsensors using p-type CVD Diamond Films," Sensors and Actuators A, vol. 45, pp. 35-43, 1994.
- [9] D.R. Wur and J. L. Davidson, "Piezoresistivity of Polycrystalline Diamond Films," presented at the Fall 1992 MRS meeting in Boston.
- [10] O. Dorsh, K. Holzner, M. Werner, E. Obermeir, R.E. Harper, C. Jhonston, P.R. Chalker and I.M. Buckley-Older, "Piezoresistive Effect in Boron-Doped Diamond Thin Films," Diamond 92 (ICNDST-3) Heidelberg, Germany, pp20.2-20.3, Sept. 1992.
- [11] M. Deguchi, N. Hase, M. Kitabatake, H. Kotera, S. Shima and M. Kitagawa, "Piezoresistive Property of CVD Diamond Films," presented at Diamond '96 (Diamond Films jointly with ICNDST-5), Tours, France, Sept. 8-13, abstract no. 16.2, 1996.
- [12] Bohr-ran Huang and D. K. Reinhard, "Electric field-dependent conductivity of

- polycrystalline diamond thin films," App. Phys. Lett., vol. 59, pp. 1494-1496, 1991.
- [13] N. Fujimori, "Electrical Applications of CVD Diamond Films," New Diamond Sci. and Tech. @ MRS Int. Conf. Proc., pp. 901-908, 1991.
- [14] K. Plamann and D. Fournier, "Thermal Conductivity of CVD Diamond: Methods and Results," Phys. Stat. Sol. A, vol. 154, pp. 351-369, 1996.
- [15] G. Lu, "Applications of CVD Diamond in Thermal Management," 2nd Int. Conf. on the Application of Diamond and Related Materials, Eds. Yoshikawa et al., vol. 2, pp. 269-274, Tokyo, Japan 1993.
- [16] C. A. Klein, G. F. Cardinale, "Young's Modulus and Poisson Ratio of CVD Diamond," Diamond and Related Materials, vol. 2, pp. 918-923, 1993.
- [17] D.R. Wur, J. L. Davidson et al., "Fabrication and Characterization of doped Polycrystalline Diamond Film (PDF) for strain Sensing Applications," Proc. 7th Int. Conf. Solid State Sensors and Actuators (Transducers'93), pp. 722-725, Okohama, Japan, June 7-10, 1993.
- [18] J. L. Davidson, D.R. Wur, W.P Kang, D. Kinser, D.V. Kerns, J. P. Wang and Y.C. Ling, "Microelectronic Pressure Sensor with Diamond Piezoresistors on Diamond Diaphragm," Advances in New Diamond Science and Technology, pp. 693-700, 1994.
- [19] M. Aslam and I. Taher, "CVD Diamond Piezoresistive Sensors," Proc. 7th Int. Conf. Solid State Sensors and Actuators (Transducers'93), pp. 718-721, Okohama, Japan, June 7-10, 1993.
- [20] Ian M. Buckley-Golder, Paul R. Chalker, Colin Johnston, Simion Romani and Matthias Werner, "High Temperature Electronic Applications of Diamond," in Advances in New Diamond Science and Technology, pp. 669-678, Tokyo 1994.
- [21] A. Masood, Technology and Electronic Properties of Diamond Film Microsensors for Thermal Signals, Ph.D. Dissertation, Michigan State University, 1991.
- [22] E. Obermeir, "High Temperature Microsensors Based on Polycrystalline Diamond Thin Films," Proc. 8th Int. Conf. Solid State Sensors and Actuators (Transducers'95), pp. 178-181, Stokholm, Sweden, June 25-29, 1995.
- [23] G.S. Yang and D.M. Aslam, "Single-Structure Heater and Temperature Sensor Using a P-type Polycrystalline Diamond Resistor," IEEE Electron Device Letters, vol. 64, pp595-597, 1994.
- [24] J.P. Bade, S.R. Sahaida, B. R. Stoner, J.A. von Weindheim, J.T. Glass, K. Miata, K.

- Nishimura and K. Kobashi, "Fabrication of Diamond Thin-Film Thermistors for High-Temperature Applications," Diamond and Related Materials, vol. 2, pp. 816-819, 1993.
- [25] G.S. Yang and D.M. Aslam, "CVD Diamond Resistor as a Heater and Temperature Sensor," Applications of Diamond Films and Related Materials, Third International Conf., Ed. A. Feldman, Y. Tzeng, W.A. Yarbrough, M. Yoshikawa and M. Murakawa, NIST Special Publications, Washington D.C., pp. 125-128, 1995.
- [26] R. Pallas-Areny and J.G. Webstr, Sensors and Signal Conditioning, John Wiley and Sons, Inc., New York, 1991.
- [27] Y. Gurbuz, W.P. Kang, J.L. Davidson, D.V. Kerns and B. Henderson, "High Sensitivity and Wide Temperature Tolerance Hydrogen Gas Sensors Using PECVD Diamond Technology," Applications of Diamond Films and Related Materials, Third International Conf., Ed. A. Feldman, Y. Tzeng, W.A. Yarbrough, M. Yoshikawa and M. Murakawa, NIST Special Publications, Washington D.C., pp. 87-90, 1995.
- [28] S. Albin, J.C. Hagwood, J.B. Cooper, D.L. Gray, S.D. Martin and M.A. Scott, "A Diamond Thin Film Flow Sensor," Applications of Diamond Films and Related Materials, Third International Conf., Ed. A. Feldman, Y. Tzeng, W.A. Yarbrough, M. Yoshikawa and M. Murakawa, NIST Special Publications, Washington D.C., pp. 113-120, 1995.
- [29] R.B. Jackman, R. McKeag, S. SM Chang and M.D. Whitefield, "Photoconductive Properties of CVD Diamond," presented at Diamond '96 (Diamond Films jointly with ICNDST-5), Tours, France, Sept. 8-13, abstract no. 16.3, 1996.
- [30] D.R. Kania, M.I. Landstrass, M.A. Plano, L.S. Pan and S. Han, "Diamond Radiation Detectors," Diamond Films and Related Materials, vol. 2, pp. 1012-1019, 1993.
- [31] V.F. Dvoryakin, A.A. Kudryashov, Yu.Sh. Temirov, L.L. Bouilov, G.A. Sokolina, and A.E. Alexenko, "CVD Diamond Films for X-ray Detectors," Applications of Diamond Films and Related Materials, Third International Conf., Ed. A. Feldman, Y. Tzeng, W.A. Yarbrough, M. Yoshikawa and M. Murakawa, NIST Special Publications, Washington D.C., pp. 128-132, 1995.
- [32] V.V. Tokiy, V.I. Timchenko, V.A. Soroka, B.V. Spitsyn and L.L. Bouilov, "Diamond Film Metal-Semiconductor-Metal Photodetector," Applications of Diamond Films and Related Materials, Third International Conf., Ed. A. Feldman, Y. Tzeng, W.A. Yarbrough, M. Yoshikawa and M. Murakawa, NIST Special Publications, Washington D.C., pp. 145-148, 1995.

- [33] L. Allers, J. Hassard, A.S. Howard, A. Mainwood and R. Mongkolnavin, "Neutron Damage of CVD Diamonds," presented at Diamond '96 (Diamond Films jointly with ICNDST-5), Tours, France, Sept. 8-13, abstract no. 13b.2, 1996.
- [34] M. Marchywka, J. Hochedez, M.W. Geis, D.G. Socker, D. Moses and R.T. Goldberg, "Ultraviolet Photoresponse Characteristics of Diamond Diaodes," Appl. Optics, vol. 30, pp. 5011-5013, 1991.
- [35] M. Marchywka and D. Moses, "Optical Characterization of Diamond MIS Capacitors," IEEE Trans. Elect. Devices, vol 41, pp. 1265-1272, 1994.
- [36] I. Taher, CVD Diamond Piezoresistive Microsensors, Ph.D. Dissertation, Michigan State University, 1994.
- [37] S. Wang, Fundamentals of Semiconductor Theory and Device Physics, New Jersey, Prentice-Hall, Inc., 1989.
- [38] J. Bardeen and W. Schockley, "Deformation Potentials and Mobilities in Non-Polar Crystals," Physical Review, vol. 80, pp. 72-85, 1950.
- [39] C. Herring, "Transport Properties of a Many-Valley Semiconductor," The Bell System Technical Journal, vol. 34, pp. 237-289, 1955.
- [40] S. Middlehoek and S.A. Audit, Silicon Sensors, London: Academic Press, 1989.
- [41] F.J. Morin et al., "Temperature Dependence of the Piezoresistance of High-Purity Silicon and Germanium," Phys. Rev., vol. 105, pp. 525-539, 1957.
- [42] E.N. Adams, "Elastoresistance in p-type Ge and Si," pp.803-804, 1954.
- [43] C. S. Smith, "Piezoresistance Effect in Germanium and Silicon," Phys. Rev., vol. 94, pp. 42-49, 1954.
- [44] T.I. Kamins, "Hall Mobility in Chemically Vapor Deposited Polycrystalline Silicon," J. Appl. Phys., Vol. 42, pp. 4347-4365, 1971.
- [45] M.M. Mandurah, K.C Saraswat, C.R. Helms and T.I. Kamins, "Dopant Segregation in Polycrystalline Silicon," J. Appl. Phys., Vol. 51, pp. 5755-5763, 1980.
- [46] N.C. Lu, L. Gerzberg, C. Lu and J.D. Meindl, "A New Conduction Model for Polycrystalline Silicon Films," IEEE Electron Device Letters, Vol. EDL-2, No. 4, pp. 95-98, 1981.
- [47] M.M. Mandurah, K.C Saraswat and T.I. Kamins, "A Model for Conduction in Polycrystalline Silicon, Part I: Theory," IEEE Transactions on Electron Devices,

- Vol. ED-28, No. 10, pp. 1163-1171, 1981.
- [48] M.L. Tarng, "Carrier Transport in Oxygen-Rich Polycrystalline-Silicon Films," J. Appl. Phys., vol. 49, pp. 4069-4076,1978.
- [49] D.M. Kim, A.N. Khondeker, S.S. Ahmed and R.R. Shah, "Theory of Conduction in Polysilicon: Drift-Diffusion Approach in Crystalline-Amorphous-crystalline Semiconductor System Part I: Small Signal Theory," IEEE Transactions on Electron Devices, Vol. ED-31, No. 4, pp. 480-493, 1984.
- [50] D.M. Kim, A.N. Khondeker, S.S. Ahmed and R.R. Shah, "Theory of Conduction in Polysilicon: Drift-Diffusion Approach in Crystalline-Amorphous-crystalline Semiconductor System Part II: General I-V Theory," IEEE Transactions on Electron Devices, Vol. ED-31, No. 4, pp. 493-500, 1984.
- [51] P. J. French and A. G. R. Evans, "Piezoresistance in Polysilicon and its Applications to Strain Gauges," Solid State Electronics, vol. 32, pp. 1-10, 1989.
- [52] J. Y. W. Seto, "Piezoresistive Properties of Polycrystalline Silicon," J. Appl. Phys., vol. 47, pp. 4780-4783, 1976.
- [53] D. Hong and M. Aslam, "Field Emission from p-type Polycrystalline Diamond Films," J. of Vac. Sc. and Tech. B, vol. 13, pp. 427-430, 1995.
- [54] J. Mort, M. A. Machonkin and K. Okumura, "Density of State Distribution in Diamond Thin Films," Appl. Phys. Let., vol. 59, pp. 455-459, 1991.
- [55] M. Werner, O. Dorsh, A. Hinze, E. Obeimeier, R. E. Harper, C. Johnson, P. R. Chalker and I. M. Buckley-Older, "Space-charge-limited Current Flow and trap density in undoped diamond Films," Diamond and Related Materials, vol. 2, pp. 825-828, 1993.
- [56] T. Sugino, Y. Muto, K. Karasutani, J. Shirafuji and K. Kobashi, "Electrical Conduction in undoped Diamond Films Prepared by Chemical Vapour Depositon," Appl. Phys. Let., vol. 59, pp.843-845, 1991.
- [57] G. A. Sokolina, A. A. Botev, S. V. Bantsekov, O. I. Lazerva, and A. F. Belyanin, "Temperature and Frequency Dependence of the Electrical Conductivity of Diamond Films," Sov. Phys. Semicond., vol. 24, pp. 105-108, 1990.
- [58] T. Sugino, Y. Muto, K. Karasutani, J. Shirafuji and K. Kobashi, "Trap states elucidated by a.c. conductance measurements in polycrystalline chemically vapour-deposited diamond films," Diamond and Related Materials, vol. 2, pp. 803-807, 1993.
- [59] R. Heiderhoff, P. Kochinski, M. Maywald, L.J. Balk and P.K. Bachmann,

- "Correlation of the Electrical, Thermal, and Optical Properties of CVD Diamond Films by Scanning Electron Microscopy Techniques," Diamond and Related Materials, vol. 4, pp. 645-651, 1995.
- [60] M. Werner, R. Job, A. Zaitzev, W.R. Fahrner, W. Seifert, C. Johnston, and P.R. Chalker, "The Relationship between Resistivity and Boron Doping Concentration of Single and Polycrystalline Diamond," Phys. Stat. Sol. (a), vol. 154, pp. 385-393, 1996.
- [61] W. Werner, O. Dorsh, H.U. Baerwind, E. Obermeier, C.Haase, W. Seifert, A. Ringhandt, C. Johnston, S. Romani, H. Bishop and P.R. Chalker, "Charge Transport in Heavily B-doped Polycrystalline Diamond Films," J. Appl. Phys. Let., vol. 64, pp. 595-597, 1994.
- [62] D. M. Malta, J. A. von Windheim, H. A. Wynands and B. A. Fox, "Comparison of the Electric Properties of Simultaneously Deposited Homoepitaxial and Polycrystalline Diamond Films," J. Appl. Phys., vol. 77, pp. 1536-1545, 1995.
- [63] A. Feldman, S. Holly, C. A. Klein and G. Lu, Workshop on Characterizing Diamond Films III, Applied Diamond Conference 1995.
- [64] F.P. Bundy, H.T. Hall, H.M. Strong and R.H. Wentroff, "Man-made Diamond," Nature, vol. 176, pp. 51-54, 1995.
- [65] R.F. Davis and J.T. Glass, "The Growth and Characterization of Silicon Carbide and Diamond for Microelectronic Applications," Advances in Solid State Chemistry, vol. 2, , JAI Press Ltd, pp. 55-111, 1991.
- [66] P.K. Bachmann, D. Leera and H. Lydtin, "Towards a general Concept of Diamond Chemical Vapour Deposition," Diamond and Related Materials, 1, pp. 1-12, 1991.
- [67] S. Harris, and L.R. Martin, "Methyl versus Acetelyne as Diamond Growth Species," J. Mater. Res., vol. 5, no. 11, Nov. 1990, pp. 2313-19.
- [68] S. Yugo, T. Kanai and T. Muto, "Generation of Diamond Nuclei by Electric Field in Plasma Chemical Vapor Deposition," Appl. Phys. Let., vol. 58, pp. 1036-38, 1991.
- [69] B.V. Spitsyn, G. Popovici and M.A. Prelas, "Problems of Diamond Film Doping," 2nd Int. Conf. on the Application of Diamond Films and Related Materials, Ed. M. Yoshikawa, M. Murakawa, Y. Tzeng and W.A. Yarbrough, MYU, Tokyo., pp. 57-64, 1993.
- [70] Gennady SH. Gildneblat, Stephen A. Grot, and Andrzej Badzian, "The electrical properties and Device Applications of Homoepitaxial and Polycrystalline Diamond Films," in Proc. of the IEEE, vol. 79, pp. 647-667, 1991.

- [71] J. Mort, D. Kuhman et al., "Boron Doping of Diamond Thin Films," Appl. Phys. Lett., vol. 55, pp. 1121-1123, 1989.
- [72] F. Zhang, E. Xie, B. Yang, Y. Cai and G. Chen, "Synthesis and Infrared Absorption Characteristics of Boron-Doped Semiconducting Diamond Thin Films," Materials Letters, vol. 19, pp. 115-118, 1994.
- [73] X. Jiang, M. Paul, P. Willich, E. Bottger and C.-P. Klages, "Controlled Boron Doping in Chemical Vapor Deposited Diamond," Diamond 96, Tours, France, Sept. 8-13, poster 8.059, 1996.
- [74] E. Colineau, et al., "Minimization of Defects Concentration from Boron Incorporation in Polycrystalline Diamond Films," Diamond 96, Tours, France, Sept. 8-13, poster 11.051, 1996.
- [75] X.Z. Liao, et al., "The influence of Boron Doping on the Structure and Characteristics of Diamond Thin Films," Diamond 96, Tours, France, Sept. 8-13, poster 8.060, 1996.
- [76] K. Miyata, K. Kumagai, K. Nishimura and K. Kobashi, "Morphology of Heaviliy B-doped Diamond Films," J. Mat. Res., vol. 8, pp. 2845-2857, 1993.
- [77] A. Masood, M. Aslam, M.A. Tamor and T.J. Potter, "Techniques for Patterning of CVD Diamond Films on non-Diamond Substrate," J. Electrochem. So., vol. 138, pp. L67-68, 1991.
- [78] T. Roppel, R. Ramesham and S.Y. Lee, "Thin Film Diamond Microstructures," Thin Solid Films, vol. 212, pp. 56-62, 1992.
- [79] J.L. Davidson, C. Ellis and R. Ramesham, "Selective Deposition of Diamond Films," New Diamond, vol. 6, pp.29-32, 1990.
- [80] K Hirabayashi, Y. Taniguchi, O. Takamatsu, T. Ikeda, K. Ikoma and N.I. Kurihara, Appl. Phys. Let., vol. 53, 1989, pp. 1071.
- [81] G. Yang, Technology of CVD Diamond Thermistor and Thin Film Heater, Ph.D. Dissertation, Michigan State University, 1996.
- [82] H. Shiomi et al., "Electrical Characteristics of Metal Contacts to Boron-Doped Diamond Epitaxial Films," Japanese J. App. Phys., vol. 28, pp. 758-62, 1989.
- [83] K. L. Moazed et al., "Diamond/Metal Interfaces," Materials Research Society, Extended Abstract (EA-19), pp. 167-169, 1989.
- [84] S. A. Grot et al., "The Effect of Surface Treatment on the Electrical Properties of Metal Contacts to Boron-Doped Homoepitaxial Diamond Film," IEEE Electron

- Device Letters, Vol. 11, pp. 100-102, 1990.
- [85] T. Tachibana, et al., "Correlation of the electrical properties of metal contacts on diamond films with the chemical nature of the metal-diamond interface. I. Gold contacts: A non-carbide-forming metal," Physical Review B, Vol. 45, pp. 11968-74, 1992.
- [86] T. Sugino, et al., "Surface Fermi Level Position of Diamond Treated with Plasma," Advances in New Diamond Science and Technology, Ed. K. Kobashi, N. Fujimori, O. Fukunaga, M. Kamo, K. Kobashi and M. Yoshikawa, MYU, Tokyo., pp. 637-640, 1994.
- [87] M.W. Geis, "Diamond Transistor Performance," Proceedings of the IEEE, vol. 79, pp.669-675, 1991.
- [88] T. Tachibana, et al., "Correlation of the electrical properties of metal contacts on diamond films with the chemical nature of the metal-diamond interface. II. Titanium contacts: A carbide-forming metal," Physical Review B, Vol. 45, pp. 11975-81, 1992.
- [89] K. Das, et al., "A Review of the Electrical Characteristics of Metal Contacts on Diamond," Applications of Diamond Films and Related Materials, Eds. T. Tzeng, M. Yoshikawa, M. Murakawa and A. Feldman, Elsevier Science Publishers B.V., pp. 301-307, 1991.
- [90] T. Iwasaki, et al., "Formation of Ohmic Contacts on Semiconducting Diamond Grown by Chemical Vapor Deposition," Diamond and Related Materials, vol. 3, pp. 30-34,1993.
- [91] V. Venkatesan et al., "Evaluation of ohmic contacts formed by B<sup>+</sup> implantation and Ti-Au metallization on diamond," J. App. Phys., vol. 74, pp. 1179-87, 1993.
- [92] S. Liu, et al. "Thermally Stable Metallizations on Polycrystalline Diamond Films," Applications of Diamond Films and Related Materials, Third International Conf., Ed. A. Feldman, Y. Tzeng, W.A. Yarbrough, M. Yoshikawa and M. Murakawa, NIST Special Publications, Washington D.C., pp. 161-164, 1995.
- [93] A. Bachi, et al. "A Novel Metallizations Scheme for Diamond," Applications of Diamond Films and Related Materials, Third International Conf., Ed. A. Feldman, Y. Tzeng, W.A. Yarbrough, M. Yoshikawa and M. Murakawa, NIST Special Publications, Washington D.C., pp. 157-160, 1995
- [94] R. Brunsteiner, R. Haubner and B. Lux, "Hot-Filament CVD Diamond Deposition on SiAlON at Pressures up to 500 torr," presented at DIAMOND 92, Aug. 31-Sept. 4, 1992, Heidelberg, Germany.

- [95] M. A. Plano, S. Zhao, C. F. Gardinier, M. I. Landstrass, D. R. Kania, H. Kagan, K.K. Gan, R. Kass, L. S. Pan, S. Han, S. Schnetzer and R. Stone, "Thickness dependence of the electrical characteristics of chemical vapor deposited diamond films," Apply. Phys. Lett., vol. 64, pp. 2923-2925, 1994.
- [96] Solid Boron Source.
- [97] H. E. Exner and H. P. Hougardy, in *Quantitative Image Analysis of Microstructures*, DGM Informationsgesellschaft mbH, 1988.
- [98] Y. Mori, H. Yagi, M. Deguchi, M. Kitabatake, K. Nishimura, A. Hatta, T. Ito, T. Hirao, T.Sasaki, and A. Hiraki, "Crystallinities and Electrical Properties of Homoepitaxial Diamond Films Grown from Carbom Monoxide," 2nd Int. Conf. on the Application of Diamond Films and Related Materials, Ed. M. Yoshikawa, M. Murakawa, T. Tzeng and W. A. Yarbourgh, MYU, Tokyo, 1993, pp. 393-398.
- [99] F. Fontaine and A. Deneuville, "High Temperature Diamond Thin Films," Diamond and Related Materials, vol. 4, pp. 673-677, 1995.
- [100] M. I. Landstrass and K. V. Ravi, "Resistivity of Chemical Vapor Deposited Diamond Films," App. Phys. Let., vol. 55, pp. 975-977, 1989.
- [101] I.M. Buckley-Golder, "Post Processing of Diamond and Diamond Films: a Review of some Harwell Work," Diamond and Related Materials, vol. 1(1991)43-50.
- [102] M. A. Plano, S. Zhao, C. F. Gardinier, M. I. Landstrass, D. R. Kania, H. Kagan, K.K. Gan, R. Kass, L. S. Pan, S. Han, S. Schnetzer and R. Stone, "Thickness dependence of the electrical characteristics of chemical vapor deposited diamond films," App. Phys. Lett., vol. 64, pp. 2923-2925, 1994.
- [103] R. Ramesham, T. Roppel, and C. Ellis, "Electrical Characterization of Undoped and Boron-Doped Polycrystalline Diamond Thin Films," J. of Electrochemical Society, vol. 138, pp. 2981-2984, 1991.
- [104] P. Gonon, A. Deneuville, E. Cheeraert and F. Fontaine, "Influence of Annealing on the Resistance of Polycrystalline Chemically Vapour Deposited Diamond Films: a Surface Chemical Effect," Diamond and Related Materials, vol. 3, pp. 654-657, 1994.
- [105] M. Tamor and W. C. Vassel, "Raman "Fingerprinting" of Amorphous Carbon Films," J. Appl. Phys., vol. 76, pp. 3823-3830, 1994.
- [106] K. Miyata, K. Kumagai, K. Nishimora and K. Kobasi, "Morphology of Heavily B-doped Diamond Films," J. Mater. Res., vol. 8, pp. 2845-2857, 1993.
- [107] F. Zhang, E. Xie, B. Yang, Y. Cai and G. Chen, "Synthesis and Infrared Absorption

- Characteristics of Boron-Doped Semiconducting Diamond Thin Films," Materials Letters, vol. 19, pp. 115-118, 1994.
- [108] T. Kamins, Polycrystalline Silicon for Integrated Circuit Applications, Klumer Academic Publishers, 1988.
- [109] Shozo Shikama, Tetsuro Maki and Takeshi Kobayashi, "Experimental Study on High-Field Transport in B-doped CVD Diamond Epitaxial Films," in Proc. of 2nd International Conference on the Applications of Diamond Films and Related Materials, M. Yoshikawa, Ed., pp. 323-328, Saitama, Japan, 1993,.
- [110] T. Sugino et al., "Electrical conduction mechanisms in polycrystalline chemically vapor-deposited diamond films", Diamond and Related Materials, vol. 2, pp. 797-802, 1993.
- [111] B. R. Stoner, D.M. Malta, A.J. Tessmer, J. Holmes, D.L. Dreifus, R.C. Glass, A. Sowers and R.J. Nemanich, "Highly Oriented Diamond Films on Si: Growth, Characterization and Devices," in Proc. of SPIE- The Int. Society for Optical Engineering on Diamond-Film Semiconductors, Vol. 2151, pp. 2-13, Los Angeles, California, 1994.
- [112] R. Heiderhoff, R. Heiderhoff, P.Koschinski, M. Maywald, L.J. Balk and P.K. Bachmann, "Correlation Between the Electrical, Thermal, and Optical Properties of CVD Diamond Films by Scanning Microscopy Techniques," Diamond and Related Materials, vol. 4, pp. 645-651, 1995.
- [113] D. M. Malta, J. A. von Windheim, H. A. Wynands and B. A. Fox, "Comparison of the Electric Properties of Simultaneously Deposited Homoepitaxial and Polycrystalline Diamond Films," J. Appl. Phys., vol. 77, pp. 1536-1545, 1995.
- [114] Gennady SH. Gildneblat, Stephen A. Grot, and Andrzej Badzian, "The electrical properties and Device Applications of Homoepitaxial and Polycrystalline Diamond Films," in Proc. of the IEEE, vol. 79, pp. 647-667, 1991.
- [115] G. A. Sokolina, A. A. Botev, S. V. Bantsekov, O. I. Lazerva, and A. F. Belyanin, "Temperature and Frequency Dependence of the Electrical Conductivity of Diamond Films," Sov. Phys. Semicond., vol. 24, pp. 105-108, 1990.
- [116] M. Jaeger, B. Golding, M. Thorpe, K. Shirai and D.M. Aslam, "Electrical Contacts to 3D Diamond Microcrystals,," Bull. Am. Phys. Soc. 40, pp. 221-223, 1995.
- [117] T. Tachibana, B.E. Williams and J.T. Glass, "Correlation of the electrical properties of metal contacts on diamond films with the chemical nature of the metal-diamond interface. I. Gold contacts: A non-carbide-forming metal," Physical Review B, Vol. 45, pp. 11968-74, 1992.

- [118] B. Huang, Electrical Properties and Physical Characterization of Polycrystalline Diamond Films Deposited in Microwave Plasma Disk Reactor, PhD Dissertation, Michigan State University, 1992.
- [119] V. Venkatesan, D.M. Malta, K. Das and M. Belu, "Evaluation of ohmic contacts formed by B<sup>+</sup> implantation and Ti-Au metallization on diamond," J. App. Phys., vol. 74, pp. 1179-87, 1993.
- [120] X. Jiang, M. Paul, P. Willich, E. Bottger and C.-P. Klages, "Controlled Boron Doping in Chemical Vapor Deposited Diamond," Faunhofer-Institut fur Schicht-und Oberflachentechnik (FhG-IST), Germany (poster 8.059)
- [121] C. H. Seager and T. G. Caster, "Zero-Bias Resistance of Grain Boundaries in Neutron-Transmutation-Doped Polycrystalline Silicon," J. App. Phys., vol. 49, pp. 3879-3889, 1978.
- [122] S. Timoshenko, *Theory of Plates and Shells*, first edition, New York: McGraw-Hill, 1940.
- [123] J.W. Dally and W.F. Riley, Experimental Stress Analysis, New York: McGraw-Hill, 1965.
- [124] D. Long, "Stress Dependence of the Piezoresistance Effect," J. Appl. Phys., vol. 32, pp. 2050-2051, 1961.
- [125] S. Sahli, X. Hou and D. M. Aslam, "Effect of Grain Size and Temperature on the Field Dependence of the Resistivity of B-doped Diamond," ADC 95, Gaithersburg, USA, pp. 103-106, 1995.
- [126] S. Sahli and D.M. Aslam, "Non-uniform Conduction in B-doped Chemical Vapor Deposited Diamond Studied by Intra- and Inter-grain Measurements," Appl. Phys. Lett., vol. 70, pp. 2129-2131, 1997.
- [127] S. Sahli, X. Hou and D. M. Aslam, "Piezoresistive Gauge Factor of Polycrystalline Diamond Measured at Different Fields and Temperatures," ADC 95, Gaithersburg, USA, pp. 95-98, 1995.
- [128] J.T. Huang, C.S. Hu, J. Hwang, L.J. Lee, "Desegregation of Boron at the Grain Boundaries of the In-situ Boron Doped Diamond Films," App. Phys. Lett. vol. 67, pp. 2382-2284, 1995.

